



UNIVERSITÀ DEGLI STUDI DI ROMA

"TOR VERGATA"

DOTTORATO DI RICERCA IN SCIENZE CHIMICHE

XXIX CICLO DEL CORSO DI DOTTORATO

Design of Graphene Based PVA composites for Biomedical Devices

Yosra Toumia

A.A. 2016/17

Tutor: Prof. Gaio Paradossi

Coordinatore: Prof. Roberto Paolesse

To my parents...

Table of Contents

Introduction	1
<i>Chapter I: Overview, Functionalization Methods and Applications in Biomedicine of Graphene and Poly(vinyl-alcohol)</i>	4
1. Graphene materials:	5
1.1 History	5
1.2.1. Electronic structure properties	5
1.2.2 Mechanical properties.....	6
1.2.3 Magnetic properties	6
1.2.4 Optical properties.....	6
1.3. Production routes.....	7
1.4 1. Raman Spectroscopy characterization:	8
1.4.2 Microscopic characterization:	9
1.5 Applications in biomedicine:	9
2. Poly(vinylalcohol) (PVA):	10
2.1. Properties of poly(vinyl-alcohol):	10
2.1.1. PVA solubility and solution viscosity:	11
2.1.2. PVA crystallinity:.....	12
2.1.3. PVA thermal properties:.....	12
2.1.4. PVA mechanical properties:	12
2.2. Applications of PVA in biomedicine:	12
2.2.1 PVA based hydrogels:	13
2.2.2. PVA based Core-shell microbubbles for bioimaging applications:.....	15
3. Aim of the work:	15
References.....	17
<i>Chapter II: Study on Graphene Functionalized PVA-Methacrylated Hydrogel</i>	20
1. Introduction:.....	21
2.1. Materials:.....	21
2.2. Methods:	22
2.2.1. Self assembly properties:	22

2.2.2. Aqueous Graphene dispersion in PEG-PEPEMA:	22
2.2.3 Graphene UV spectrophotometry quantification:	23
2.2.4 Synthesis of PVA-MA:	23
2.2.5 Synthesis of graphene based PVAMA hydrogels:	23
2.2.6 Synthesis of thermoresponsive graphene based PVA/p(MA-co-NiPAAm) thermoresponsive hydrogels:	24
2.2.7. NMR spectroscopy:	25
2.2.8 Raman spectroscopy characterization:	25
2.2.9 Dynamic light scattering (DLS):	25
2.2.10 Scanning Electron Microscopy (SEM):	25
2.2.11 Rheology:	26
2.2.12 Confocal laser scanning microscopy (CLSM):	26
2.2.13 Differential Scanning Calorimetry (DSC):	26
2.2.14 Doxorubicine (DOX) loading and release kinetics:	27
3. Results and Discussion:	27
3.1. Self assembly properties of PEG-PEPEMA:	27
3.2. Graphene UV spectrophotometry quantification:	28
3.3. NMR spectroscopy:	29
3.4. Raman spectroscopy characterizations:	29
3.5. Dynamic Light Scattering:	33
3.6. Scanning Electron Microscopy:	34
3.7. Rheology:	35
3.8. Confocal laser microscopy:	36
3.9. Differential Scanning Calorimetry:	37
3.10. Doxorubicin loading and delivery kinetics:	40
Conclusion	42
References	43
Chapter III: Photoacoustic Imaging in Biomedicine and Hybrid Contrast Agents	45
Introduction:	46
1. Photoacoustic effect history:	46
2. Concept of photoacoustic imaging (PAI):	46
3. Ultrasound and photoacoustic imaging in biomedicine:	48
3.1. Ultrasound imaging (US):	48
3.2. Photoacoustic imaging vs. ultrasound imaging:	50

4. Hybrid Contrast agents:.....	54
4.1 Specific contrast agents for ultrasound imaging:	54
4.2 Specific contrast agents for photoacoustic imaging:	57
5. Hypothesis and aims:.....	62
References.....	63
Chapter IV: Synthesis of graphene-PVA microbubbles a hybrid contrast agent for PAI	68
1. Introduction:.....	69
2.1. Materials:.....	69
2.2. Methods:	69
2.2.1. Poly(vinyl-alcohol) microbubbles, PVA MBs, preparation :.....	69
2.2.2. Ethylene diamine, EDA, PVA MBs functionalization:	70
2.2.3. Graphene Aqueous Dispersion Preparation:.....	71
2.2.4. Graphene functionalization of PVA-EDA MBs:	71
2.2.5. G/PVA RBITC labeled MBs:	72
2.2.6. Optical and confocal microscopy characterization:	72
2.2.7. Raman spectroscopy characterization:	73
2.2.8. Thermogravimetric analysis (TGA):	73
2.2.9. Differential Scanning calorimetry:.....	73
2.2.10. Field emission scanning electron microscopy (FESEM):.....	73
2.2.11. Ultrasound properties measurements:	74
2.2.12. In vitro photoacoustic imaging:.....	74
2.2.13. <i>In vivo</i> photoacoustic imaging	75
3. Results and Discussion.....	75
3.1. Primary amine groups quantification on modified PVA-EDA MBs.....	75
3.2. Characterization of graphene dispersion and G/PVA hybrid MBs	76
3.3. Raman spectroscopy characterization of graphene dispersion and of G/PVA MBs:	80
3. 4. Thermogravimetric analysis of PVA and G/PVA MBs:	84
3.5. Differential Scanning Calorimetry:	85
3.6. Field emission scanning electron microscopy:	86
3.7. Ultrasound properties of G/PVA MBs:	88
3.8. Photoacoustic behavior of pristine graphene	89
3.9. <i>In vitro</i> photoacoustic imaging of G/PVA MBs:	91
3.10. <i>In vivo</i> photoacoustic imaging of G/PVA MBs	94
Conclusion	96

References.....	97
Chapter V: Effect of Diamine Intermediate on Graphene PVA MBs and Cytotoxicity Evaluation	101
1. Introduction.....	102
2.1. Materials.....	102
2.2. Methods	103
2.2.1. Diamine Surface Modification of PVA Microbubbles and Graphene Functionalization	103
2.2.2. Primary Diamine Quantification of PVA Microbubbles Modified Surfaces:.....	103
2.2.3. Graphene PVA Diamine Microbubbles Functionalization:	103
2.2.4. Acoustic Attenuation Measurements of Graphene PVA Diamines Microbubbles:	
2.2.5. MTT Cytotoxicity Assay of Graphene PVA Diamines Microbubbles:.....	104
3. Results and discussion:.....	105
3.1. Diamine functionalization of PVA microbubbles:.....	105
3.2. Graphene PVA-diamines microbubbles:	106
3.3. Acoustic Properties of Graphene/PVA-Diamines Microbubbles:.....	107
3.4. Cytotoxicity Evaluation of Graphene/PVA-Diamines Microbubbles	109
Conclusion	110
References.....	111
Concluding Remarks and Future Directions	112
Appendix: Polymerized Surfactant Shell-Perfluorocarbon Filled-Micro/Nanodroplets for Ultrasound Imaging Applications	117
1. Introduction:.....	118
2. Materials:.....	118
3. Methods:	118
3.1. Poly-PCDA-DFP/ PFP filled droplets preparation.....	118
3.2. Tween 80 droplets preparation.....	119
3.3. Dynamic light scattering (DLS).....	120
3.4. Bright field, Fluorescence and CLSM microscopy.....	120
3.5. Acoustic droplets vaporization (ADV).....	120
3.6. Droplets preparation by microfluidics.....	121
4. Discussion	122
4.1. PCDA-PFC nanodroplets	122
4.2. Tween 80-PFC droplets.....	129
5. Formulation of PFC droplets by Microfluidics	131

6. Conclusion and perspectives	133
References	134
ACKNOWLEDGMENTS	136
LIST OF PUBLICATIONS	137

Introduction

This work conducted within Prof. Paradossi's group at the Department of Chemical Science and Technology in the University of Rome Tor Vergata aimed to develop an easily applicable strategy enabling functionalization of graphene, suspended in an aqueous medium in its pristine form, to biocompatible polymeric surfaces, in particular "poly(vinylalcohol)" platforms, designed for biomedical applications. Nowadays graphene, this new two-dimensional material with fascinating properties, is emerging in many scientific fields. Exploitation of graphene properties has been one of the motivations to implement biomedical applications of interest for our laboratory. Our investigations are about what kind of functionalities can be introduced in a polymeric platform, such as hydrogel sponges for anti-tumor drug delivery or the surface of microbubbles, still in the development phase as multimodal imaging contrast agents mainly for ultrasounds and photoacoustics. To this regard, photoacoustic imaging is a high-resolution preclinical fast developing diagnostic tool. Evolution of this imaging methodology can bring to a new clinical tool designed for human investigation and is a major challenge that can be tackled by *ad hoc* engineered contrast agents. To this aim an optimized selection of advanced hybrid platforms is needed. Graphene derivatives, mainly graphene oxide (GO) and reduced graphene oxide (RGO), exhibiting depleted properties with respect to pristine graphene, but chemically more versatile, have been highlighted in the recent literature. These forms derive from the chemical modifications of the 2D structure of graphene in very harsh conditions, which introduce kinks and irregularities in the carbonic material. Such modifications make GO and RGO more reactive and more processable than pristine graphene, but jeopardize the electrical, optical and mechanical properties of this material. Despite this fact, we have not found a study that reports the incorporation of pristine graphene into biomedical devices starting from its suspended form in aqueous media. The challenge herein was to preserve the graphene original properties which are important for the applications we address; and find the intermediate key to adequately tether

graphene on our studied poly(vinylalcohol) composites. For this, Prof. Paradossi's group strong background about poly(vinylalcohol) hydrogels and microbubbles was a great advantage.

The first chapter of the thesis is a brief general introduction about graphene and poly(vinylalcohol) providing the necessary details of why these materials could be interesting candidates for our research, taking into account the main problems concerning the separate materials as well as their assembly and formulating hypothesis regarding the efficiency and biocompatibility of the hybrid systems.

The second chapter is a proof of concept on the method allowing pristine graphene entrapment into a poly(vinylalcohol) hydrogel matrix with potential in drug release at physiological temperature by using thermosensitive moieties.

The third chapter of this thesis is a general introduction to the photoacoustic imaging. It provides the basic theoretical foundation for understanding this method and the physical mechanisms related to photoacoustic generation in biological tissues. First, we describe light propagation mechanisms in tissues, and the deposition of heat via optical absorption. Assimilating the biological tissue to a liquid medium, we then introduce the fundamental equations describing the photoacoustic issue, and the assumptions used in imaging to improve diagnosis. We also introduce ultrasound imaging and its inherent clinical approach for diagnostic and therapy. Finally, the contrast agents used in both ultrasound and photoacoustic imaging modalities are discussed through two important examples: microbubbles and NIR absorbing agents.

The chapter IV details the state of the art in the context of the objectives we pursued during this thesis regarding hybrid contrast agents for photoacoustic imaging based pristine graphene and poly(vinylalcohol) microbubbles. Details on the microdevice fabrication as well as its physico-chemical characterization are provided. Finally, the potential of the graphene poly(vinylalcohol) microbubbles in enhancing the photoacoustic signal is assessed in vitro and in vivo.

In the chapter V, we present a study on the influence of diamine intermediates and PEGylation used as links between graphene and the PVA microbubbles on the colloidal behavior, acoustic properties, and cytotoxicity of the overall system.

An appendix is presented at the end of the thesis describing a preliminary work carried recently on the realization of new “phase-change” ultrasound contrast agents with a photo-polymerized surfactant monolayer shell structure encapsulating perfluorocarbon. These systems are in normal conditions droplets and upon ultrasound irradiation, they convert into microbubbles by “acoustic droplet vaporization”. The phase change efficiency is studied and the experimental setup and operating conditions are detailed.

Chapter I:

Overview, Functionalization Methods and Applications in Biomedicine of Graphene and Poly(vinyl-alcohol)

Chapter I

1. Graphene materials:

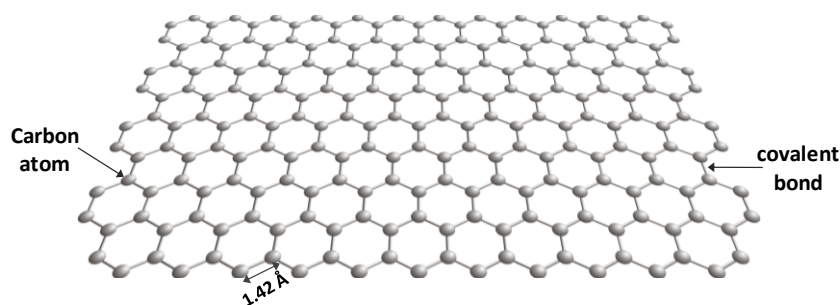
1.1 History

The graphene history goes back to 1947 with the work of P. R Wallace. Later on, few studies were carried out by scientists describing first observations of multi-layers graphene.^[1,2] Only in 2004 and for the first time, the successful isolation of one-thick atom single-layer graphene has been achieved by Andre Geim and Konstantin Novoselov at the University of Manchester. Their experiment consisted on a multi-step micromechanical cleavage of graphite using a scotch tape deposited on a graphite substrate. Lifting away the tape, a single sheet was delaminated. Characterization of its electrical features, mechanical strength and thermal conductivity revealed unusual and unique properties, making graphene a very promising material for the future. The two researchers were later awarded the Nobel Prize in Physics in 2010. Since this “groundbreaking” experiment, graphene has become a rising material crossing the horizon of condensed matter and materials science in diverse fields^[3-5].

1.2.1. Electronic structure properties

Graphene is one- atom thick carbon layer arranged in a honeycomb structure with sp^2 configuration (see [scheme 1](#)) and it is the basis of its allotropes such as carbon nanotubes, fullerene and graphite. Graphene has proven to be a zero overlap semimetal with a very high electrical conductivity with one free available electron per each carbon atom. Delocalized electrons in graphene obey a linear dispersion behaviour making it exhibit a number of very peculiar electronic properties such as the high mobility at room temperature, the quantum Hall effect, an ambipolar electric field effect, and a good optical transparency. Due to its high electron mobility ($200\,000\text{ cm}^2/\text{V s}$), graphene is thermally and electrically highly conductive.
[6]

Chapter I



Scheme 1. Graphene structure

1.2.2 Mechanical properties

Due to its 0.142 nm-long carbon bonds, graphene is considered the strongest ever discovered material. The good mechanical properties of graphene with a large Young's Modulus make it very promising. As compared to steel, graphene is six times lighter, five to six times less dense, harder and more extensible. Moreover, it is stiffer to bending, environmentally friendly and cost effective^[7].

1.2.3 Magnetic properties

Magnetism in sp^2 hybridized carbon materials is due to possible contamination by magnetic impurities. The paramagnetic and some other magnetic characteristics, including magnetic switching phenomena have been observed as well in the graphene systems.^[8]

1.2.4 Optical properties

Graphene has optical transparency, admitting that the electrons in a graphene sheet have a very high mobility and considering its unique one atom thick carbon structure, graphene is able to absorb 2,3% of white light. The optical absorption of graphene layers shows a linear proportionality with the number of layers, each absorbing the same amount of light of one single layer, i.e. 2.3%, over the visible spectrum. In a few-layer graphene this can be explained by considering the delocalized electrons of each sheet as a 2D electron gas, with little perturbations from adjacent layers, making it optically equivalent to a superposition of almost non-

Chapter I

interacting single-layers. The absorption spectrum of pristine graphene is almost wavelength independent from the visible to the infrared region, and exhibits a peak in the UV region around 270 nm, due to the π - π electronic transition of the electron orbitals. In few-layers graphene, other absorption features are present at lower energies, associated with interband transitions.^[9,10]

1.3. Production routes

Several methods are employed to produce graphene, and may be classified mainly according to the nature of the starting graphite, pristine or modified, which leads to either a pristine graphene form or a graphene derivative respectively; also the state of the obtained graphene should be considered as it can be accomplished as a solid on a substrate or as a liquid suspension. Among these methods, mechanical cleavage, chemical vapor deposition (CVD), epitaxial growth on SiC and arc discharge of graphite yield a pristine form of graphene in the solid state. On the contrary, graphene colloidal suspensions can be obtained by organic solvents extraction from graphite and/or surfactants assisted ultra-sonication, or through the oxidation of graphite oxide followed by its subsequent exfoliation in water to yield graphene oxide (GO). The latter can undergo a reduction process, via a thermal route or by hydrazine, to obtain reduced graphene oxide (RGO). Each synthetic procedure was a new solution to a previous problem. Indeed, the mechanical cleavage of graphite, particularly highly oriented pyrolytic graphite (HOPG), and CVD procedures lead to the highest quality of graphene, but they are not scalable methods and are difficult to apply. Thus, processing graphene in liquid solutions is an exciting alternative for a large scale production and a promising route to obtain graphene materials suitable for several applications crossing diverse fields. Successful exfoliation of graphite to give defect-free graphene using certain organic solvents such as DMF, DMSO, NMP, etc has been reported.^[11] However, this method has its drawbacks due to the toxicity and high boiling points of these solvents and therefore it requires a specific handling which is unsuitable for several applications such as biomedical ones.^[12] The most common technique is to disperse graphene in aqueous medium through the oxidation of graphite leading to the formation of epoxy bridges, carboxyl, carbonyl,

Chapter I

and hydroxyl groups on its surface. By subsequent exfoliation in water, GO sheets can be obtained up to 7mg/ml, ^[13,14] and could be easily further functionalized to obtain hybrid materials with some stability in water. Still this method suffers from one serious drawback; the oxidation process introduces significant defects in the 2D, planar structure of graphene as evidenced by Raman spectroscopy, altering severely the unique electronic properties of graphene. Even after a reduction process, it is from one side impossible to completely remove the defects due to the presence of residual oxygen groups, and from another side a problem of dispersion stability occurs ^[14]. These structural modifications make GO and RGO different materials from pristine graphene. However, ultrasound-assisted exfoliation of graphite in water using surfactant, which does not require neither oxidation process nor chemical post-treatments, was proved to be a cheap and friendly way to produce relatively free-defect graphene. However, it leads to low graphene yield with respect to the oxidative procedure (up to 1mg/ml). ^[13,15]

1.4 1. Raman Spectroscopy characterization:

Raman spectroscopy is historically a method able to provide a fingerprint of the structural characteristics of graphitic materials, and has become a powerful technique to understand the behavior of electrons and phonons in graphene, aiming at gaining a better understanding of its quality. Several and recent Raman studies on the different thickness of graphene were carried out at 532 and 614 nm excitation wavelengths, where the first order (G) and the double resonance Raman scattering (2D) mechanisms were discussed to distinguish the monolayer from multilayered structures and determine the number of layers in a graphene sample. At 532 nm in single layer graphene, G and 2D appear at 1580 and 2680 cm^{-1} , respectively: the 2D band should be more intense than the G band, and can be fitted into a single Lorentzian peak. Therefore, the intensity ratio 2D/G together with the shape analysis of 2D allow for the determination of the number of graphene layers. Another important feature of graphene is the D mode at 1340 cm^{-1} , which is related to defects in the structure and is present in structurally disordered samples. Thus, the D/G bands intensities ratio is a useful indicator to quantify the disorder in the graphene sp^2 network. ^[16-18]

Chapter I

1.4.2 Microscopic characterization:

Direct observation of graphene sheets is possible using microscopy techniques. Mainly transmission electron microscopy (TEM), scanning electron microscopy (SEM) and atomic force microscopy (AFM) are commonly used to characterize graphene materials. These techniques give information concerning the lateral size and the shape of graphene as well as the number of layers, and are therefore considered as complementary methods to the Raman spectroscopy characterization. The layers can be distinguished by the edge contrast produced in a graphene sheet when using TEM or SEM, whereas AFM provides a more precise determination by measuring the thickness of the latter. Besides, a direct visualization of graphene allows for a deeper study of its structural morphology, when it is either free or incorporated in composites such as polymers, in addition to determining the mechanical properties as can be assessed by AFM. ^[19,20]

1.5 Applications in biomedicine:

It is worth to notice that for biomedical research, most studies reported in the literature investigated graphene derivatives i.e. GO and RGO for their easy functionalization. The functionalization of graphene derivatives could be either covalent or non-covalent i.e. by π - π interaction. ^[21] The particular features of graphene and its derivatives render them interesting and promising templates which can fit the needs of numerous biomedical applications, ranging from biosensing to imaging and cancer therapy. Indeed, graphene materials offer high therapeutic molecule loading capacity due to their high available surface area and have been explored as potential drug delivery systems such as doxorubicin (DOX) and heparin. ^[22] This is due to stable π - π stacking between the aromatic rings in the drug and the graphene surface which leads to stable complex formation, avoiding chemical conjugation. Moreover the engineering of graphene hydrogels as scaffolds for cellular growth has been reported and showed enhanced cellular attachment and proliferation, which makes graphene a suitable material as a drug carrier and to make smart scaffolds. ^[23]

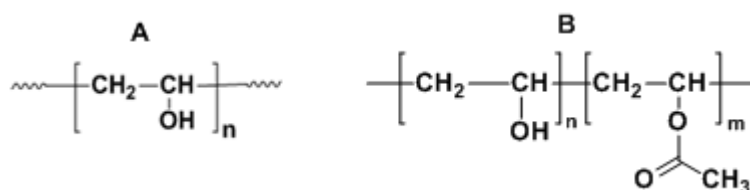
Graphene derivatives have also been recently investigated as a therapeutic agent due to the ability to absorb at the near-infrared (NIR) spectral region and

Chapter I

subsequently convert the absorbed energy into heat leading to thermal ablation of tumor tissues.^[24]

2. Poly(vinylalcohol) (PVA):

PVA is a hydrophilic linear polymer, which was first prepared by Herrmann and Haenel in 1924.^[25] This polymer is not obtained directly from a monomer, but from the full or partial hydrolysis of poly(vinyl acetate). Now many grades of PVA are available in the market, and are classified according to the hydrolysis percentage of the acetate as well as the polymerization degree. PVA is considered fully hydrolyzed when the degree of hydrolysis is above 98%, whereas a partially hydrolyzed PVA has a degree of deacetylation $\approx 87\%$ ^[26] (see proposed structures in scheme 2). The differences in the PVA grades lend it to a wide variety of applications such as emulsion stabilizers, adhesives, textile and even biomedicine. Each type of PVA finds use for some applications but not for others, as the properties of the polymer change in terms of viscosity behavior, crystallinity and solubility; hence an adequate selection of PVA grade is depending on the application requirements.^[27]



Scheme 2. Chemical structure of PVA: fully hydrolyzed A, partially hydrolyzed B

The repetitive units in a PVA chain are a sequence of head-to-tail consecutive repeats. However, defects can be present in the form of head-to-head sequences (about 2%) which are advantageous to make a telechelic polymer with specific groups allowing the design of advanced systems.^[27]

2.1. Properties of poly(vinyl-alcohol):

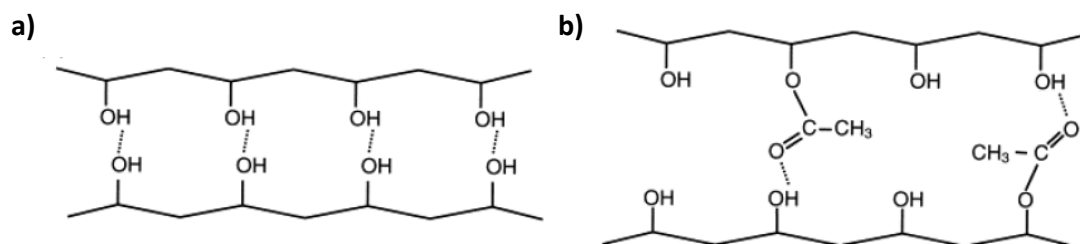
The chemical and physical properties of PVA are linked to its structure which varies with the chain lengths and the degree of hydrolysis, or alternatively degree of acetylation. These structure features affect the rheology of polymer solutions and properties of the PVA powder, in other terms, its mechanical properties, crystallinity and water solubility.^[27]

Chapter I

2.1.1. PVA solubility and solution viscosity:

The degree of hydrolysis and the degree of polymerization play both a significant role in defining the water solubility of PVA. The hydroxyl groups present in the PVA structure are the reason of its good affinity to water. However, strong hydrogen bonding between the intra- and inter-molecular hydroxyl groups greatly impedes its solubility in aqueous solutions. Besides, the residual acetate groups in the partially hydrolyzed PVA weaken the hydrogen bonding by acting as spacers and make therefore the polymer more soluble in water (see scheme 3). The PVA solubility increases with the temperature and it may be required to increase the temperatures as high as 80°C to achieve high solubility. This is because the hydrogen bonds between the hydroxyl groups of PVA chains are disrupted by the increased mobility of the molecules while those between PVA and water molecules are favored. [27, 28]

Moreover, PVA is insoluble in many organic solvents with the exception of dimethyl sulfoxide (DMSO). [27,29]



Scheme 3. Hydrogen bonds in a) fully hydrolyzed PVA and b) in partially hydrolyzed PVA: at higher acetylation degree, the acetate groups act as spacers and limit the hydrogen bonds.

The viscosity of PVA aqueous solutions mainly depends on the concentration and the degree of polymerization. As the polymer concentration and/or the chain length increase, the formation of inter- and intra-hydrogen bonds is enhanced. As a consequence the water becomes a poorer solvent and the viscosity is increased. However, the temperature and the degree of acetylation weakly affect the PVA viscosity in water because a higher molecular mobility is not effective as much as the concentration and molecular weight to reduce the hydrogen bondings between the chains. [27,29, 30]

Chapter I

2.1.2. PVA crystallinity:

PVA is a partially crystalline polymer. The crystallinity tends to be limited with increasing molecular weight since long molecular chains involve impeded segmental motion making the folding-up of the molecules into crystalline structure more difficult. Acetyl groups prevent molecular chains from a close approach as discussed above limiting the crystallinity. ^[26-30]

2.1.3. PVA thermal properties:

Upon heating, PVA undergoes a melting transition and is decomposed at temperatures above 200°C. These features change depending on the crystallinity degree of the polymer, its tacticity and consequently on its structure. It is also known that PVA crystallinity and melting point T_m decrease as the distribution of the residual acetyl groups is more random. ^[26, 27] Typical melting points are on the order of 228 to 240°C for atactic, 212 to 235°C for isotactic and 230 to 267°C for syndiotactic structures. The glass transition temperature is 85°C for highly hydrolyzed PVA and 58°C for 87 % - 89 % hydrolyzation. ^[27, 29, 31]

2.1.4. PVA mechanical properties:

In addition to its interesting chemical and structural properties, PVA exhibits a high tensile strength, varying from 30 MPa to 110 MPa, proportional to the molecular weight and relative humidity. The ability to obtain such a wide range of tensile strength values makes this polymer appropriate for diverse applications. ^[27]

PVA is also characterized by properties such as chemical resistance, and biocompatibility.

2.2. Applications of PVA in biomedicine:

PVA is biocompatible with human tissues; its fibrils can absorb protein molecules and engage with minimal cell adhesion without toxic effects. It is often used as coating material for stents or other devices that need to be introduced in the human body. Therefore, PVA based composites have been widely developed for biomedical applications from drug delivery systems to tissue engineering yet to bioimaging thanks to its solubility in water, good biocompatibility and easy functionalization. ^[32- 36]

Chapter I

2.2.1 PVA based hydrogels:

Hydrogels, defined as highly hydrated systems, are physically and chemically versatile devices widely investigated and used in biomedical research. They offer a favorable environment for many biological systems as cells and tissues because of their high water content and enhanced diffusion properties. Moreover, hydrogels function as physical or chemical shields against potentially toxic substances while preserving the natural hydration state of metabolites.^[37]

PVA is often crosslinked especially when used in the biomedical field. Moreover, it has an excellent ability to form hydrogels which can be made by a cross-linking process by a chemical reaction or UV light with photo-initiators, electron-beam or gamma radiation.^[33-35,38]

The physical hydrogels can be obtained via “Freeze-thaw”, a process consisting of repeated cycles of freezing and thawing, at high concentrations of PVA aqueous solutions (at least 10% w/v) and comprise non covalent junction knots of hydrogen bonding and Vander Waals forces.^[39] The first work describing the preparation of PVA based hydrogel using this method was by Peppas in 1975.^[40] In his work, aqueous solutions, 2.5 and 15% wt of PVA, were frozen at -20 °C and thawed back to room temperature resulting in the formation of crystallites rendering the polymer insoluble in water. Then in 1984, Nambu reproduced PVA hydrogels by freezing and thawing processes for biomedical applications.^[41]

This treatment allows one to obtaining stable PVA gel at room temperature which retains its original shape, but can be extended up to five or six times its initial size due to its high elasticity and high mechanical strength. However, these properties depend on many factors such as the molecular weight of the polymer, concentration, temperature, freezing time, and the number of freezing-thawing cycles. The more cycles are repeated the more density and chain entanglements increase resulting in higher rigidity. Nonetheless, the potential applications in biomedicine of these kinds of hydrogels are limited by their weak mechanical properties, and the need to perform many freeze-thaw cycles in order to enhance

Chapter I

the mechanical strength is not commercially attractive. The work presented in chapter II will focus on the chemically photocross-linked PVA hydrogels.

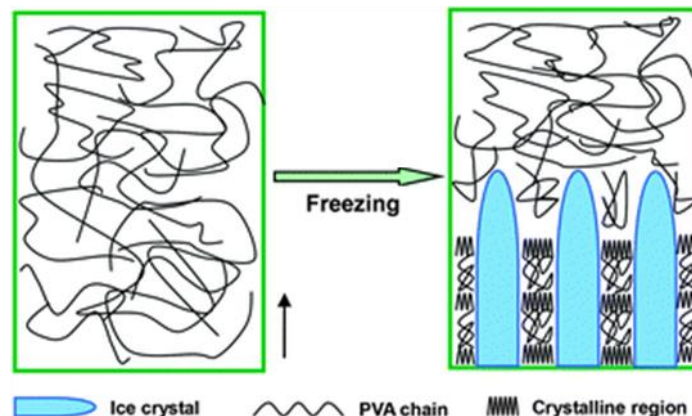


Figure 1. Schematic representation of PVA gelation by freeze thaw process. *Copyright Zhang et.al. Soft Matter (2012) 8, 10439-10447.*

The nearly fully hydrolyzed forms of PVA result in forming hydrogels with tunable properties through crosslinking of the linear polymer chains. PVA contents affect the physical status of the resulting material: low PVA content results in soft materials because the fluid (water) moves freely through the matrix, whereas a higher content results in considerable stiffening and strengthening of the polymeric matrix.^[27]

In recent studies, Paradossi *et.al* have explored PVA based hydrogels, from macro to micro scale, such as macroscopic hydrogels and microgels obtained by photocrosslinking methacryloyl-grafted PVA in the presence of photoinitiator,^[35,42] and hydrogels obtained by Michael-type addition via a nucleophilic thiol-ene addition between a thiol capped PVA and grafted methacrylic PVA chains.^[34] These systems reveal good mechanical properties, good biocompatibility and are physically and chemically very stable.

In addition, PVA chains grafted with methacrylic moieties offer the possibility to copolymerize with thermosensitive oligomers to give a thermoresponsive hydrogel above a low critical solution temperature (LCST). The crosslinks lead to the stability of the hydrogel when it swells in water or in biological tissues or shrinks according to the physical conditions (temperature, pH, salt concentration). This “switchable state” concept is a promising route for drug delivery and biotechnologies in general. A

Chapter I

recent work, described by Shivikumar *et. al.*, investigates the thermoresponse of a methacryloyl- grafted PVA “smart” microgel copolymerized with N-isopropyl acrylamide (NiPAAm), a well known oligomer exhibiting a LCST around 33°C, and demonstrates that a volume phase transition temperature (VPTT) of the system is induced within the physiological range, a behavior, which has positively affected the release of doxorubicin (DOX), an anti-cancer drug, when varying the temperature from RT to 37°C.^[35,42] Moreover, these PVA based hydrogels have shown a potential in tumor targeting, due to good chemical versatility of the polymer matrix, by functionalizing their networks with molecules such as hyaluronic acid.^[43]

2.2.2. PVA based Core-shell microbubbles for bioimaging applications:

PVA microparticles are of interest in the bioimaging field due to their inherent mechanical and physico-chemical properties. Recent studies carried by Paradossi *et.al* have shown the successful formulation of biocompatible and stable PVA microbubbles and their great potential as ultrasound imaging contrast agents aiming to enhance the diagnosis of diseases at an early stage. Ultrasound imaging and the important function of microbubbles will be further discussed in Chapter III. PVA microbubbles also demonstrated the ability to be transformed into microcapsules leaving unchanged their surface characteristics.^[44] Such PVA systems revealed very promising for theranostics: they offers at once good echogenicity and an adequate platform for drug loading in addition to the possibility to decorate their surface with tumor targeting molecules such as hyaluronic acid to target CD44 cancer cells receptors or RGD peptides.to target $\alpha\text{v}\beta\text{3}$ integrin.

3. Aim of the work:

The goal of the studies described in this dissertation is to incorporate graphene into an adequate biocompatible platform such as PVA, which offers a high chemical versatility, to fabricate advanced devices for bioimaging applications, drug delivery and tissue engineering.

The experimental work carried out as part of this dissertation was designed to address the following related research questions:

Chapter I

1. How to stably tether graphene prepared in an aqueous medium while preserving its pristine form, i.e. without passing by an oxidation process, to a PVA matrix?
2. How does graphene affect the features of the PVA matrix?
3. How does graphene improve the functionalities of the hybrid system?
4. How to define the graphene biocompatibility or toxicity?

Chapter I

References

- [1] Wallace, P. R. The Band Structure of Graphite. *Phys. Rev.* **1947**, *71*, 622–634.
- [2] Bonuu, H. P.; Cleuss, A.; Fischer, G.; Hofmann, U. Surface Properties of Extremely Thin Graphite Lamellae. Proceedings of the Fifth Conference on Carbon. Pergamon Press 1962, 73-80.
- [3] Novoselov, K. S.; Geim, A. K.; Morozov, S. V.; Jiang, D.; Zhang, Y.; Dubonos, S. V.; Grigorieva, I. V.; Firsov, A. A. *Science* **2004**, *306*, 666–669.
- [4] Geim, A. K.; Novoselov, K. S. The rise of Graphene. *Nat. Mater.* **2007**, *6*, 183–191.
- [5] Choi, W.; Lahiri, I.; Seelaboyina, R.; Kang, Y. S. Synthesis of Graphene and its Applications A Review. *Crit. Rev. Solid State* **2010**, *35*, 52–71.
- [6] Loh, K. P.; Bao, Q.; Ang, P. K.; Yang, J. J. *Mater. Chem.* **2010**, *20*, 2277–2289.
- [7] Ovidko, I. A. *Rev. Adv. Mater. Sci.* **2013**, *34*, 1-11.
- [8] Joly, V. L. J.; Kiguchi, M.; Hao, S. J.; Takai, K.; Enoki, T.; Sumii, R.; Amemiya, K.; Muramatsu, H.; Hayashi, T.; Kim, Y. A. et al. *Phys. Rev. B.* **2010**, *81*, 245428.
- [9] Kin FaiMaka, K. F.; Ju, L.; Wang, F.; Heinz, T. F. *Solid State Commun.* **2012**, *152*, 1341–1349.
- [10] Fernandez-Merino MJ, Guardia L, Paredes JI, Villar-Rodil S, Solis-Fernandez P, Martinez-Alonso A, et al. *J Phys Chem C.* **2010**; *114*, 6426–6432.
- [11] Ramakrishna Matte, H. S. S.; Subrahmanyam, K. S.; Rao, C. N. R. Synthetic Aspects and Selective Properties of Graphene. *Nanomater. Nanotechnol.* **2011**, *1*, 3-13.
- [12] Hernandez, Y.; Nicolosi, V.; Lotya, M.; Blighe, F. M.; Sun, Z.; De, S.; McGovern, I. T.; Holland, B.; Byrne, M.; Gun'ko, Y. K.; et al. *Nat. Nanotechnol.* **2008**, *3*, 563-568.
- [13] Cui, X.; Zhang, C.; Hao, R.; Yanglong. *Nanoscale* **2011**, *3*, 2118-2126.
- [14] Park, S.; Ruoff, R. S. *Nat. Nano.* **2009**, *4*, 217-224.
- [15] Lotya, M.; Hernandez, Y.; Kin, P. J.; Smith, R. J.; Nicolosi, V.; Karlsson, L. S.; Blighe, F. M.; De, S.; Wang, Z.; McGovern, I. T.; et al. *J. Am. Chem. Soc.* **2009**, *131*, 3611–3620.
- [16] Ferrari, A. C.; Meyer, J. C.; Scardaci, V.; Casiraghi, C.; Lazzeri, M.; Mauri, F.; Piscanec, S.; Jiang, D.; Novoselov, K. S.; Roth, S.; et al. *Phys. Rev. Lett.* **2006**, *97*, 187401-187404;

Chapter I

- [17] Ferrari, A. C. *Solid State Commun.* **2007**, *143*, 47–57.
- [18] Rao, R.; Podila, R.; Tsuchikawa, R.; Katoch, J.; Tishler, D.; Rao, A. M.; Ishigami, M. *ACS Nano.* **2011**, *5*, 1594 – 1599.
- [19] Park, M. H.; Kim, T. H.; Yang, C. W. Thickness Contrast of Few-layered Graphene in SEM. *Surf. Interface Anal.* **2012**, *44*, 1538 – 1541.
- [20] Wu, Z, S.; Ren, W.; Gao, L.; Liu, B.; Jiang, C.; Cheng, H. M. Synthesis of High Quality of Graphene with Predetermined Number of Layers. *Carbon* **2009**, *47*, 493-499.
- [21] Zheng, W.; Shen, B.; Zhai, W. Surface Functionalization of Graphene with Polymers for Enhanced Properties. *INTECH* **2013**, doi.org/10.5772/50490.
- [22] An, J.; Gou, Y.; Yang, C.; Hu, F.; Wang, C. Synthesis of a Biocompatible Gelatin Functionalized Graphene Nanosheets and its Application for Drug Delivery. *Mater. Sci. Eng. C* **2013**, *33*, 2827-2837.
- [23] Lee, S. K.; Kim, H.; Shim, B. S. Graphene an Emerging Material for Biological Tissue Engineering. *Carbon. Lett.* **2012**, *14*, 63-75.
- [24] Jung, H. S.; Kong, W. H.; Sung, D. K.; Lee, M. Y.; Beack, S. E.; Keum, D. H.; Kim, K. S.; Yun, S. H.; Hahn, S. K. NanographeneOxide_Hyaluronic Acid Conjugate for Photothermal Ablation Therapy of Skin Cancer. *ACS Nano* **2014**, *8*, 260-268.
- [25] Ger, Pat. *Consortium für Elektrochemische Industrie G.m.b.H.* **1924**, *450*, 286.
- [26] Tubbs, R. K. *J. Polym. Sci A1* **1966**, *4*, 623.
- [27] K. Toyoshima, Finch C. A. Polyvinyl Alcohol Properties and Application. Wiley, New York 1973, 17-64.
- [28] Feng, J.; Dogan, F. Structural Materials: Properties, Microstructure and Processing. *Mater. Sci. Eng. A* **2000**, *283*, 56-64.
- [29] Marten, F. L. Vinyl Alcohol Polymers. *Kirk-Othmer Encyclopedia of Chemical Technology* **2002** Wiley, New York, Online.
- [30] Vinyl Alcohol Polymers, *Encyclopedia of Polymer Science and Technology*, John Wiley & Sons, New York, NY **1971**, *14*, 149-207.
- [31] Molyneux, P. Water-soluble Synthetic Polymers, *CRC, Boca Raton, FL*, **1983**, *1*, 119-186.

Chapter I

[32] Paradossi, G.; Cavalieri, F.; Chiessi, E. Poly(vinyl-alcohol) as Verstatile Biomaterial for Potential Biomedical Applications. *J. Mater. Sci. Mater. Med.* **2003**, *14*, 687-691.

[33] Otsuka, E.; Suzuki, A. Swelling Properties of Physically Cross-linked PVA Gels Prepared by a Cast-drying Method. *Progr. Colloid. Polym. Sci.* **2009**, *136*, 121-126.

[34] Tortora, M.; Cavalieri, F.; Chiessi, E. Paradossi, G. Michael-Type Addition Reactions for the In Situ Formation of Poly(vinyl alcohol) Based Hydrogels. *Biomacromolecules* **2007**, *8*, 209-214.

[35] Ghugare, S. V.; Mozetic, P.; Paradossi, G. Temperature –Sensitive poly(vinylalcohol)/Poly(methacrylate-co-N-isopropyl acrylamide) Microgels for Doxorubicin Delivery. *Biomacromolecules* **2009**, *10*, 1589.

[36] Vrana, N.E.; Liu, Y.; McGuinness, G.B.; Cahill P.A. Characterization of poly(vinyl alcohol)/chitosan Hydrogels as Vascular Tissue Engineering Scaffolds. *Macromol. Symp.* **2008**, *269*, 106–110.

[37] Kopeček, J. Hydrogel Biomaterials: A Smart Future? *Biomaterials* **2007**, *28*, 5185-5192.

[38] Hennink, W.E.; van Nostrum, C.F. Novel Crosslinking Methods to Design Hydrogels. *Adv. Drug Deliver Rev.* **2002**, *54*, 13-36.

[39] Hassan, C. M.; Trakampan, P.; Peppas, N. A. Water Solubility Characteristics of Poly(vinyl alcohol) and Gels Prepared by Freezing/Thawing Processes. (book Chapter) *Water Soluble Polymers, Plenum Press, New York* **1998**, 31-40.

[40] Peppas, A. N. Turbidimetric Studies of Poly(vinyl-alcohol) Solutions. *Die Makromolekulare Chemie* **1975**, *176*, 3433-3440.

[41] Nambu, M. *Japanese patent* **1984**, 56446.

[42] Ghugare, S. V.; Chiessi, E.; Telling, M.; Deriu A.; Gerelli, Y.; Wuttke, J.; Paradossi, G. Structure and Dynamics of a Thermo-responsive Microgel around its Volume Phase Transition Temperature. *J. Phys. Chem. B.* **2010**, *114*, 10285.

[43] Paradossi, G. Hydrogels Formed by Cross-linked Poly(vinyl alcohol). *Polymeric Biomaterials: Structure and Function, Volume 1*, CRC Press, S. Dumitriu, V. I. Popa Eds. **2013** ISBN 9781420094701.

[44] Cavalieri, F.; El Hamassi, A.; Chiessi, E.; Paradossi, G. Villa, R.; Zaffaroni, N. Ligands Tethering to Biocompatible Ultrasound Active Polymeric Microbubbles Surface. *Macromol. Symp.* **2006**, *234*, 94–101.

Chapter II:

Study on Graphene Functionalized PVA-Methacrylated Hydrogel

Chapter II

1. Introduction:

In this chapter we show how to fabricate a robust, highly hydrated hybrid system by combining the advantages offered by a stable aqueous dispersion of pristine graphene sheets with the chemical anchoring offered by a hydrophilic and permeable PVA based polymer matrix. Such a system has been accomplished by the key choice of the surfactant scaffold allowing stabilization of graphene during ultrasonication-assisted exfoliation. We also consider the possibility of including N-isopropylacrylamide (NiPAAm) as comonomer whose sequences are known to display a lower critical solution temperature (LCST) in water close to physiological temperature. The presence of this moiety gives rise to a volume phase transition (VPT) in the macroscopic hydrogels, which can be suitably deployed for controlled drug release. Raman analysis was used to characterize the state of PVA hydrogel entrapping graphene in its network. Evidence for an intimate interaction of graphene sheets with the polymer matrix was collected. Release of the anticancer drug doxorubicin has been tested to evaluate the active role of the graphene/PVA/p(NiPAAm) construct in the drug delivery.

2.1. Materials:

Poly(ethylene glycol) 2,4,6-tris(1-phenylethyl)phenyl ether methacrylate (PEG-PEPEMA), synthetic graphite powder with size particles $< 20 \mu\text{m}$, poly(vinyl alcohol) (PVA) with a number average molecular weight, M_n , and weight average molecular weight, M_w , of 30 ± 5 and 70 ± 10 kg/mol, respectively, 4-dimethyl-amino-pyridine (DMAP), glycidyl methacrylate (GMA), dimethylsulfoxide (DMSO), acetone, hydrochloric acid (HCl), doxorubicin hydrochloride (DOX), N,N'-isopropylacrylamide (NiPAAm) were Sigma Aldrich products. NiPAAm was purified by recrystallization in n-hexane before use. Pyrene was purchased from Fluka and the photoinitiator Irgacure 2959 from BASF. Milli-Q quality water ($18.2 \text{ M}\Omega \cdot \text{cm}$) was produced by a deionization apparatus Pure Lab from USF (Perugia, Italy).

Chapter II

2.2. Methods:

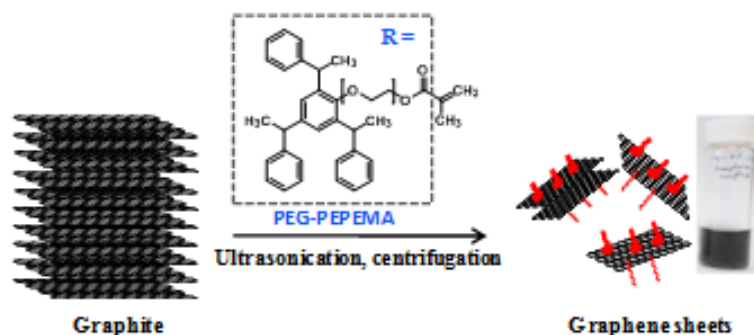
2.2.1. Self assembly properties:

The critical micelle concentration CMC of the surfactant was determined in aqueous medium by fluorescence spectroscopy using pyrene^[1] as a probe. A fixed volume of a stock solution of pyrene in acetone at a concentration of 10^{-6} M was transferred into vials and kept at room temperature under the hood until acetone evaporation was complete. Aqueous solutions of the surfactant, PEG-PEPEMA, at concentrations ranging from 10^{-8} to 10^{-2} M were added to the pyrene containing vials. The pyrene concentration was set to $6 \cdot 10^{-7}$ M for each solution and the mixtures were equilibrated by stirring at room temperature for 48 hours.

Fluorescence spectra were recorded from 350 to 450 nm using a spectrofluorometer, RF-5031 PC, equipped with 150 W Xenon lamp (Shimadzu Scientific, Mi, IT) emitting at an excitation wavelength of 341 nm. A 1.5 nm slit width was used for both excitation and emission modes.

2.2.2. Aqueous Graphene dispersion in PEG-PEPEMA:

In a typical experiment graphite powder was added to an aqueous surfactant solution (0.625 mM) at a concentration of 10mg/ml, then exfoliated by a non destructive π - π stacking interaction and via ultra-sonication for 90 minutes at 320W using a tip sonicator, these conditions were the optimum for our study. Vander Waals interactions between the graphene plans were overcome by the sheer force caused by the sonication and the help the surfactant, PEG-PEPEMA, to stabilize the exfoliated sheets in water through the interaction between the aromatic rings with the surface graphene sheet. The surfactant concentration, the graphite starting amount and the sonication parameters were optimized. The dispersion was placed in an ice bath during the exfoliation process to avoid over-heating, and it was stirred, every 30 minutes of continuous ultrasonication cycles, at 1500 rpm for 2 minutes to homogenize the non exfoliated graphite powder throughout the water surfactant solution in order to obtain higher exfoliation yield. The resulting dispersion was then centrifuged twice for 30 minutes at 1300 rpm to remove large aggregates.



Scheme 1. Surfactant (PEG-PEPEMA) assisted ultrasonication of graphene

2.2.3 Graphene UV spectrophotometry quantification:

The stabilizing ability of the surfactant was evaluated by determining the graphene concentration of the obtained dispersion yielded by ultrasonication, estimated by UV spectrophotometry at 660 nm using the molar extinction coefficient reported in the literature for graphene/surfactant aqueous solutions ($\epsilon = 1390 \text{ mL mg}^{-1}\text{m}^{-1}$) [2]. The measurement was carried on a double beam JASCO V-630 UV-vis spectrophotometer, the suspension was 10 fold diluted, and the absorbance of the surfactant, although negligible in the visible spectral region, has been subtracted.

2.2.4 Synthesis of PVA-MA:

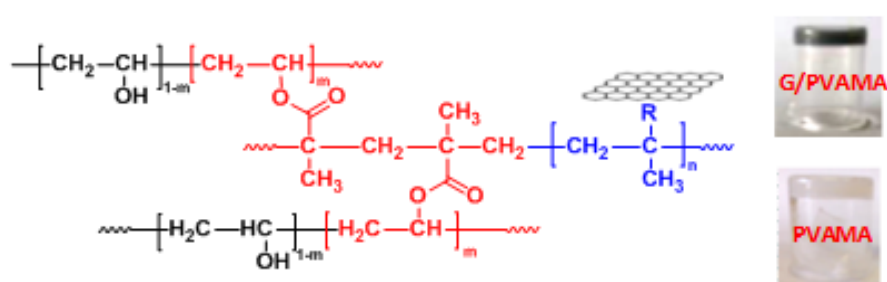
2 g of PVA was dissolved in 50 ml of DMSO under stirring and heating at 80° C. The solution was cooled to room temperature, followed by the addition of 1g DMAP under nitrogen flow. The solution was stirred and after 1 hour 0.16 mg of GMA was added. The reaction was kept under stirring in the darkness for 48 hours and then neutralized by the addition of 6M HCl to prevent alkaline hydrolysis of the methacrylic ester. The reaction mixture was intensively purified by dialysis against water using 12000 g/mol dialysis membranes to purify the derivative of PVA and to exchange DMSO with water. The resulting product was then freeze-dried and stored.

2.2.5 Synthesis of graphene based PVAMA hydrogels:

The surfactant PEG-PEPEMA-graphene adduct was crosslinked via a free radical photo-polymerization to methacryloyl- modified polyvinyl alcohol (PVA-MA), to form the hybrid hydrogel G/PVAMA: PVA-MA was dissolved in 0.1 mg/ml graphene dispersion at a concentration of 4% (w/v), followed by the addition of the

Chapter II

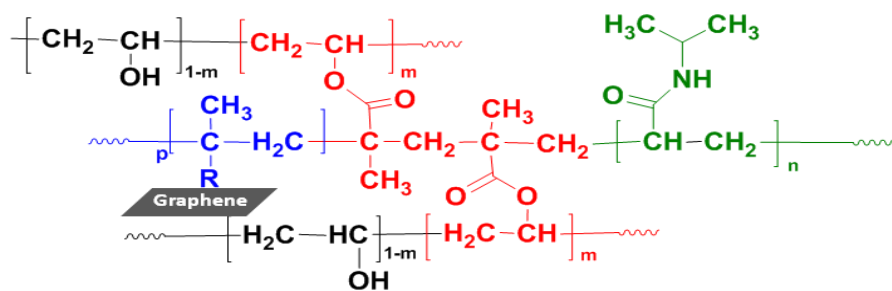
photoinitiator Irgacure 2959 at a concentration of 0.3% (w/v). The suspension was then irradiated for 5 minutes using a 365 nm UV light source at 7mW/cm². The obtained hybrid hydrogel (see scheme 2) was kept for 12 hours before being intensively washed with mQ water. It was noted that with higher graphene concentrations larger photoinitiator amount and longer UV irradiation time are required to form the hydrogel network. For comparison study, in a blank experiment, pure hydrogel PVAMA was prepared by dissolving PVA-MA in 0.625 mM aqueous surfactant solution following the same previous conditions for comparison study.



Scheme 2. G/PVAMA average chemical structure and hydrogels pictures

2.2.6 Synthesis of thermoresponsive graphene based PVA/p(MA-co-NiPAAm) thermoresponsive hydrogels:

Oligomers of poly(NiPAAm), were incorporated into the hydrogel network. Typically 4% (w/v) and 0.3% (w/v) of respectively PVA-MA and photoinitiator were dissolved in 0.1 mg/ml graphene dispersion, followed by the addition of 2.6% (w/v) of NiPAAm in ice bath. The suspension was then crosslinked by UV light as described above for 5 min. Blank hydrogels containing pNiPAAm were also prepared for this study (see scheme 3).



Scheme 3. G/PVA-p(MA-co-NiPAAm) chemical structure

Chapter II

2.2.7. NMR spectroscopy:

After methacryloyl grafting, the substitution degree, DS, value of PVA was calculated by ^1H NMR carried out with a Bruker 300 MHz spectrometer at 40°C by dissolving 7mg of the freeze dried polymer in 1mL of D_2O .

2.2.8 Raman spectroscopy characterization:

The Raman study was carried out using a Raman confocal microscope, Horiba Jobin Yvon XploRA, equipped with solid state laser sources at 532 and 785 nm and a 100x objective. Analysis of the graphene PEG-PEPEMA aqueous dispersion was performed using the 532 nm excitation wavelength and by evaporating, in air and at room temperature, a few microliters of the suspension deposited on a Si wafer. Nonetheless, for the hydrogel constructs, dried films were prepared and the spectra were recorded at 785 nm excitation wavelength to suppress the fluorescence of the polymer and maximize the sensitivity to the studied sample, then compared with the spectra of the graphene suspension recorded at the same wavelength.

2.2.9 Dynamic light scattering (DLS):

The average hydrodynamic size of the dispersed graphene sheets was evaluated using a DLS photometer and a BI-200SM goniometer with a BI-9000AT correlation board (Brookhaven Instruments Co.) equipped with a solid state laser source emitting at 532 nm. Analysis of the autocorrelation function, $g^2(q,t)$, of the scattered intensity was carried out using the CONTIN algorithm provided as part of the standard instrument software package. The graphene solution was 10-fold diluted with mQ water before measuring.

2.2.10 Scanning Electron Microscopy (SEM):

Graphene sheets morphology was analysed by Field emission-SEM using (SUPRA™ 35, Carl Zeiss SMT, Oberkochen, Germany). Approximately, 5 μl of graphene suspension (0.1 mg/ml) were deposited on Aluminum stub and dried in air at room temperature. The sample was then gold sputtered for 1 minute at 25 mA, using a sputter coater (EMITECH K550X, Quorum Technologies Ltd, West Sussex, United Kingdom) before observation. Micrographs were recorded by using the in-lens detector at a working distance of 3.8 mm with 5kV gun voltage.

Chapter II

2.2.11 Rheology:

The viscoelastic properties of hybrid graphene-containing hydrogels were investigated using a rheometer AR 2000 (TA Instruments) equipped with a 20 mm parallel acrylic plate geometry and a Peltier unit for temperature control to compare the viscoelastic behavior of hybrid G/PVAMA with respect to blank PVAMA hydrogels. The variation of storage modulus, G' , and loss modulus, G'' , was monitored with the linear regime under a constant strain of 1%, determined by dynamic strain sweep measurement, as a function of applied frequency, ranging from 0.1 to 10 rad/s at 25 °C.

The volume phase transition temperature, VPPT, of the GPVA/p(MA-co-NiPAAm), PVA/p(MA-co-NiPAAm) hybrid and blank hydrogels was performed by oscillatory time sweeps measurements, varying the temperature under linear regime applying an oscillating strain of 0.3% and a frequency of 1 Hz.

2. 2.12 Confocal laser scanning microscopy (CLSM):

The morphology of hydrogels was studied on dried films. Observations were performed under a green laser ($\lambda_{\text{excitation}} = 488 \text{ nm}$; $\lambda_{\text{emission}} = 515 \text{ nm}$) using a confocal laser scanning microscope (Nikon Inverted Microscope Eclipse model Ti-E from Nikon Instrument (Japan), equipped with: 60x/1.4 oil immersion objective, Argon-Ion laser (488 nm) (MellesGriot, Carlsbad, CA, USA), Helium-Neon laser (543.5 nm) (Spectra Physics, Mountain View, CA, USA)).

2.2.13 Differential Scanning Calorimetry (DSC):

Graphene hybrid hydrogel and blank hydrogel were examined using TA Q2000 differential scanning calorimeter. Exact amount of 4 mg of freeze-dried hydrogel was placed in an aluminum pan and sealed with holed aluminum lid. The scan was performed from 20°C to 250°C at a heating rate of 10°C/min under a flow of 50ml/min of nitrogen.

For graphene/PVA-MA co-pNiPAAm hydrogel, DSC was performed at a heating rate of 1°C/min from 10 °C to 120 °C under 50 ml/min nitrogen flow.

Chapter II

2.2.14 Doxorubicine (DOX) loading and release kinetics:

Thermoresponsive hybrid hydrogel was immersed in 0.64 mg/ml aqueous DOX solution, and kept 48 hours in the dark at room temperature for loading. The amount of the loaded DOX was determined using UV spectrophotometry as the difference of DOX absorbance at 480 nm before and after the loading. The hydrogel was then incubated in 5 ml of 0.1 M PBS solution (pH 7.4) at 25°C and 37°C. The absorbance of released DOX was measured every hour and PBS solution was changed each time.

The interaction between graphene sheets and DOX was studied by fluorescence spectroscopy. DOX was dissolved in 0.1 mg/ml graphene aqueous dispersion at concentrations ranging from 0.01 to 0.2 mg/ml. The fluorescence spectra were obtained at 480 nm excitation with a slit width of 3nm. Pure DOX was also dissolved in water at the same concentrations as in graphene for comparison.

3. Results and Discussion:

3.1. Self assembly properties of PEG-PEPEMA:

The study of the self-assembly properties of the surfactant molecule is an important parameter to optimize the yield of the graphene content in an aqueous suspension. The minimum surfactant concentration required to successfully suspend graphene in water using an appropriate surfactant is the CMC [2]. Pyrene probe emission at 373 and 383 nm wavelengths with intensities named I_1 and I_3 , respectively, was used to monitor the CMC of PEG-PEPEMA (see Figure 1). CMC value was estimated from the variation of the ratio (I_1/I_3) as a function of the surfactant concentration taking the intersection of the best linear fit lines (see Figure 1b). According to this method, the CMC of the used PEG-PEPEMA surfactant was $1.54 \cdot 10^{-5}$ M.

Chapter II

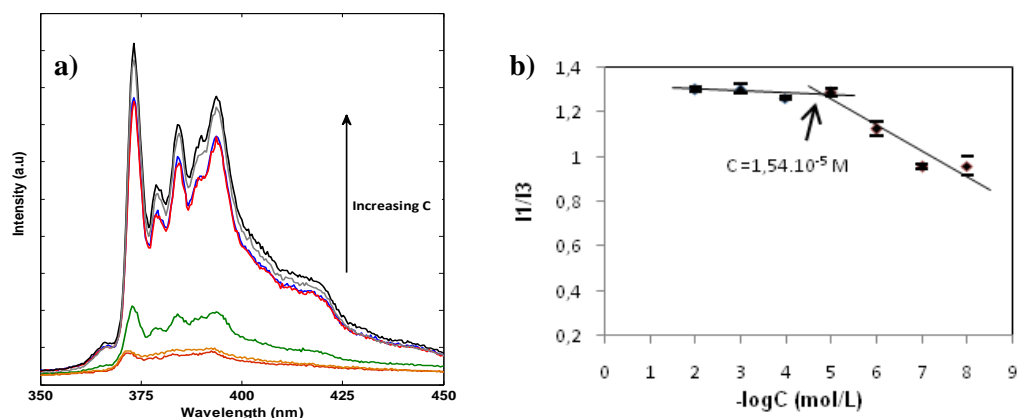


Figure 1. a) Pyrene/PEG-PEPEMA emission spectra; b) I_1/I_3 vs. PEG-PEPEMA concentration

3.2. Graphene UV spectrophotometry quantification:

Noting that the PEG-PEPEMA surfactant absorbance was subtracted, the graphene aqueous dispersion UV spectrum [Figure 2](#) shows an almost wavelength-independent absorbance in the visible/NIR domain and a maximum at 271 nm that is attributed to the $\pi \rightarrow \pi^*$ transition of C-C aromatic bonds. These spectral features, as discussed in Chapter I section 1.2.4, are consistent with graphitic objects, ^[3] and confirm the pristine-like quality of the obtained graphene flakes ^[4].

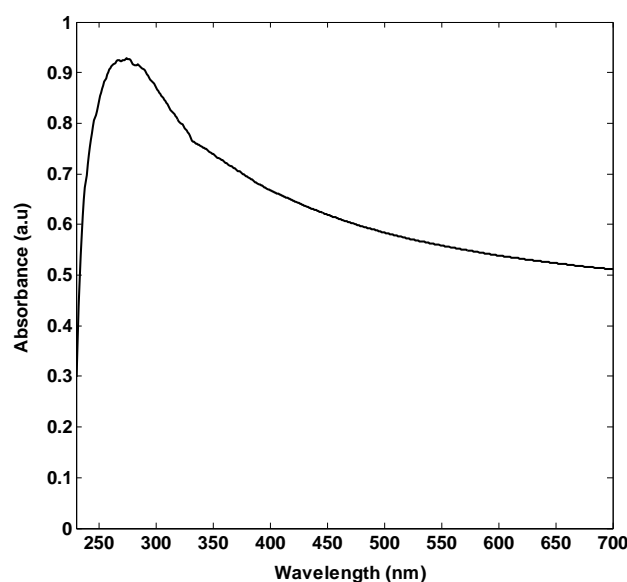


Figure 2. Graphene PEGPEPEMA aqueous dispersion UV-vis spectrum

Graphene concentration was estimated at 660 nm described in the [Experimental Section \(2.2.3\)](#). The obtained graphene sheets dispersion was stable for several weeks and achieved concentrations up to 0.3 mg/ml.

Chapter II

3. 3. NMR spectroscopy:

Figure 3 illustrates ^1H NMR spectrum of PVA-MA. According to the ratio of the peak areas of the vinyl protons at 5.66 and 6.08 ppm and the unsubstituted methine moiety at 3.98 ppm of the PVA backbone, the DS value was determined as equal to 2.5%.

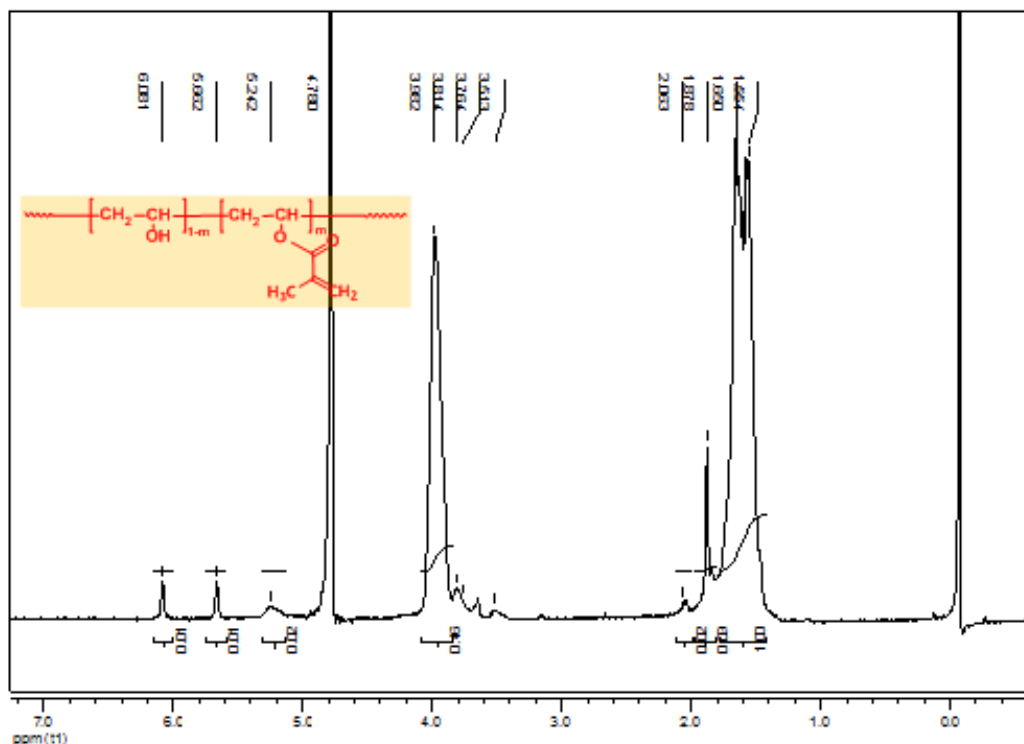


Figure 3. PVA-MA ^1H NMR spectrum in D_2O , $T=40^\circ\text{C}$

3. 4. Raman spectroscopy characterizations:

The spectra of the graphene dispersion are shown in Figure 4. The typical features of graphene: D, G, and 2D bands, are respectively at around 1343 , 1571 and 2680 cm^{-1} . Another band, at $\approx 3240\text{ cm}^{-1}$, marked as 2D', has been observed and ascribed to graphene on Si substrate [5-8].

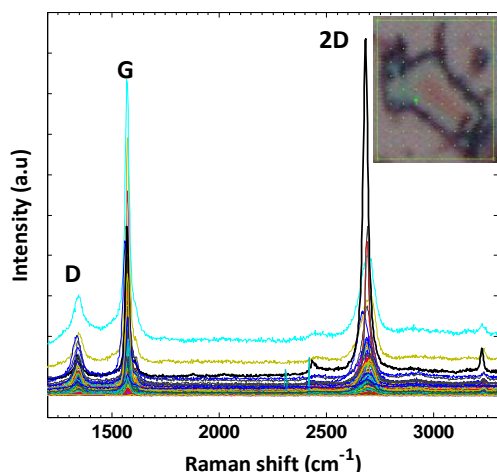


Figure 4. Raman spectra of graphene/PEG-PEPMA dispersion at 532 nm excitation. Inset: bright field micrograph of graphenic aggregate, the green spot indicates one point of the mapping

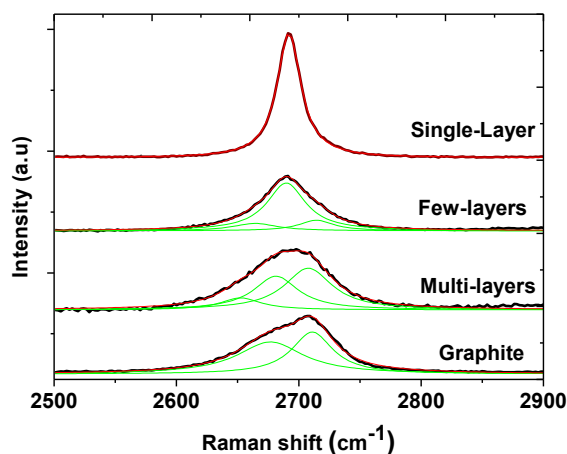


Figure 5. Graphene 2D band in graphite and PEG-PEPMA aqueous dispersion at 532 nm. Green lines describe the Lorentzian deconvolution band and red lines indicate the best fit.

According to the Raman mapping, the graphene/PEG-PEPMA aqueous suspension is a composition of graphene flakes with arrangements varying from single to few-layers as assessed by the values of intensities ratio I_{2D}/I_G and by the shape of 2D band.^[6-8] Figure 5 shows a set 2D bands collected by mapping different spots of a sample of graphene stabilized suspension. It is possible to detect (upper line in figure 5) sharp and perfectly symmetric intense Lorentzian signal attributed to single-layer graphene sheet. For a qualitative study, the Raman spectral features of the graphene suspension were compared with the starting graphite as shown in Figure 6a where it is clear the presence of D band in both spectra with comparable intensity. The deconvolution of the G band, reported in Figure 6b, has revealed an additional peak at around 1615 cm^{-1} , not present in the starting graphite sample. This peak is attributed to D' band, which is also related to the presence of defects caused by the ultra-sonication process during the exfoliation.^[9] Based on 2D shape and 2D/G, as well as D/G intensity ratios (see Table 1), we may confirm the presence of monolayer graphene as well as few-layers with limited defects.

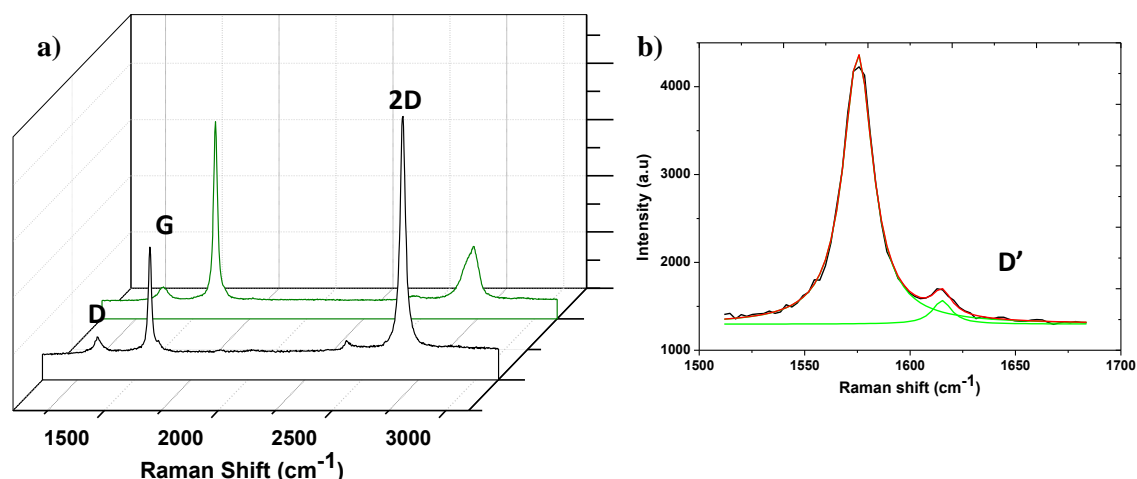


Figure 6. a) Raman spectra comparison between starting graphite (green) and single layer graphene in the aqueous suspension (black); b) Graphene G band deconvolution λ_{exc} 532 nm.

The Raman bands were fitted with a linear combination of Lorentzians:

$$y = y_0 + \frac{2A}{\pi} \frac{w}{4(x-x_c)^2 + w^2} \quad (1)$$

where y_0 , x_c , A , w , and H are the offset, the peak Raman shift, the area, the full width half maximum and the height of the peak, respectively.

Table1. Summary of the Raman features of Graphite and single-layer graphene using eq 1 as fitting equation

	Graphite			Graphene		
	D	G	2D	D	G	2D
x_c (cm ⁻¹)	1370.6	1599.9	2737.1	1343.4	1571.0	2681.4
w (cm ⁻¹)	50.2	19.7	76.9	36.2	16.7	27
A (a.u)	73949.6	393832.3	466454.6	57607.8	196001.1	709187.2
H (a.u)	2254.9	14039.1	5038.8	2999.9	9343.0	18918.7
I_D/I_G (a.u)		0.2 ± 0.01			0.3 ± 0.02	
I_{2D}/I_G (a.u)		1.2 ± 0.04			3.6 ± 0.03	

A typical Raman spectrum excited using the 785 nm (1.58 eV) laser source is reported in Figure 7. Few papers describe Raman studies on pristine graphene at such excitation wavelength.^[10,11] However, a striking different behavior of D and 2D

Chapter II

modes, as compared to the 532 nm (2.33 eV) studies, has been reported. In fact, as it was explained in the literature both D and 2D bands result from a double resonance Raman scattering mechanism, and whose frequencies depend on the energy of the incident laser. In agreement with literature, for single layer graphene excited at 785 nm ^[10,11], we notice that the intensity of D band is much more enhanced, whereas the 2D band is weak and not a single peak with a complex shape exhibiting a significant asymmetric broadening, which can be described by two Lorentzian components. The reported studies strongly suggest that the 2D mode line shape depends on the excitation energy. This difference in the shape and intensity with respect to the common laser excitation of 2.33 eV is due to the deformation of Dirac cones, i.e. the surface describing electron transport in graphene, as the energy increases. This complexity in the 2D mode when excited with 785 nm was explained by the contribution of two distinct processes (inner and outer) to the double resonance signal, such behavior indicates an alteration of the inner/outer contributions to the DR scattering signal in graphene, as a function of the incident photon energy.^[12]

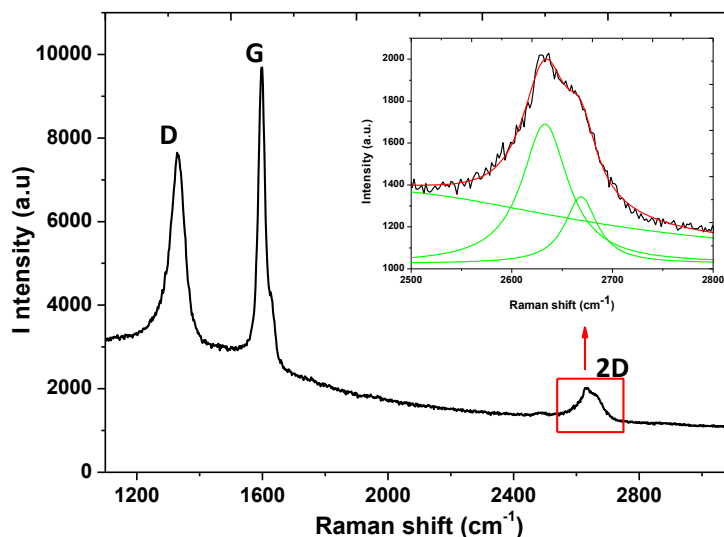


Figure 7. Raman spectrum using a $\lambda_{\text{exc}} = 785$ nm of graphene suspension in dry state on Si wafer. In the in-set is reported the Lorentzian fit of the 2D band.

Chapter II

To confirm graphene incorporation in the PVA hydrogel network, Raman spectrum of G/PVAMA dried hydrogel film was compared with the blank PVAMA (Figure 8a). In the obtained spectrum of PVAMA, the bands observed at around 2900 cm^{-1} , 1440 cm^{-1} , 1310 cm^{-1} , and 1100 cm^{-1} are attributed to C-H stretching, CH_2 , CH_3 bending modes, and C-O-C stretching of the polymeric backbone chain, respectively. However, the band at around 1600 cm^{-1} and superimposed to the G mode of graphene, can be attributed to the phenyl moiety stretching vibration of the cross-linked surfactant. Despite the spectral complexity displayed by the polymer matrix it was easy to distinguish feature bands of graphene in G/PVAMA with shapes and intensities as comparable to those obtained in the graphene dispersion at 785 nm excitation wavelength.^[10-12] The Raman mapping of G/PVAMA in Figure 8b revealed the signature of graphene in all Raman-mapped regions, demonstrating a very homogeneous distribution of the graphene sheets in the hydrogel matrix.

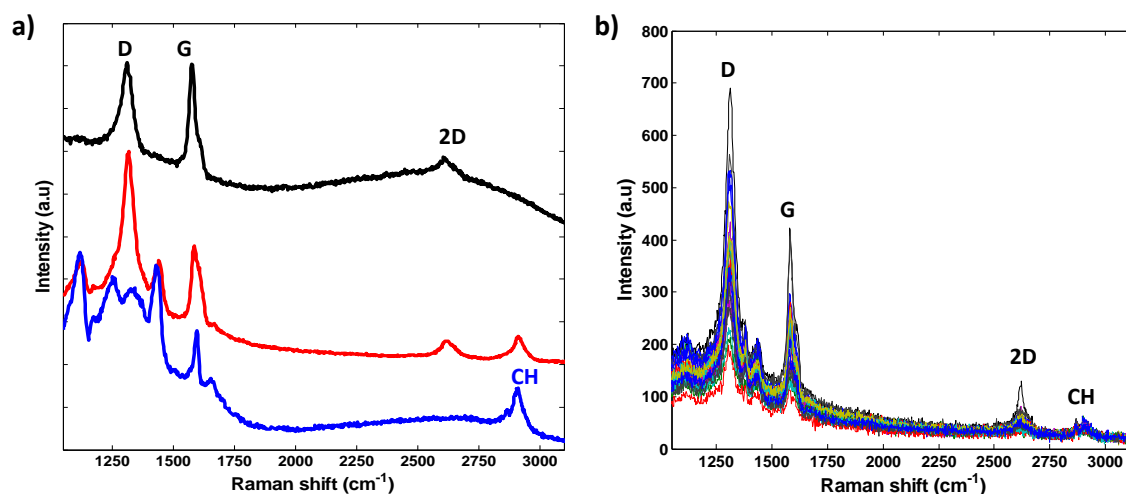


Figure 8. a) Raman spectra at $\lambda_{\text{exc}} = 785\text{ nm}$; b), graphene suspension (black), G/PVAMA hydrogel (red) and PVAMA hydrogel (blue) in dry states; right, confocal Raman mapping of the G/PVAMA dried hydrogel film.

3.5. Dynamic Light Scattering:

DLS can be used provide an estimation of the average dimensions as for non-spherical particles,^[13,14] DLS measurements allow determination of the hydrodynamic diameter of an equivalent sphere with the same translational diffusion coefficient of the investigated particles. The hydrodynamic diameter distribution of the graphene sheets exfoliated and stabilized by PEG-PEPEMA

Chapter II

surfactant is shown in [Figure 9](#) which reveals an average value of 500 nm with a mean standard deviation of 20 nm.

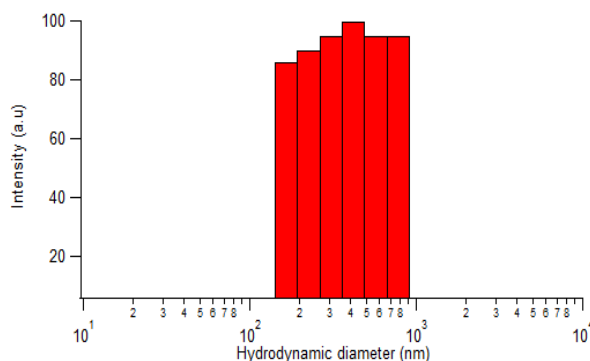


Figure 9. Graphene sheets size distribution dispersed in PEG-PEPEMA aqueous solution

3.6. Scanning Electron Microscopy:

The suspended graphene consisted of flakes with a lateral size between 2 and several hundred of nanometers (see [Figure 10 a-b](#)) confirming the results obtained by DLS. [Figure 7b](#) shows an almost perfect pile stacking sheets of few layered graphene (about 4 layers). It is worth noting that the exact number of layers cannot be precisely determined at the operating acceleration voltage, but it could be estimated by taking as a lateral marker the contrast edge produced.^[15]

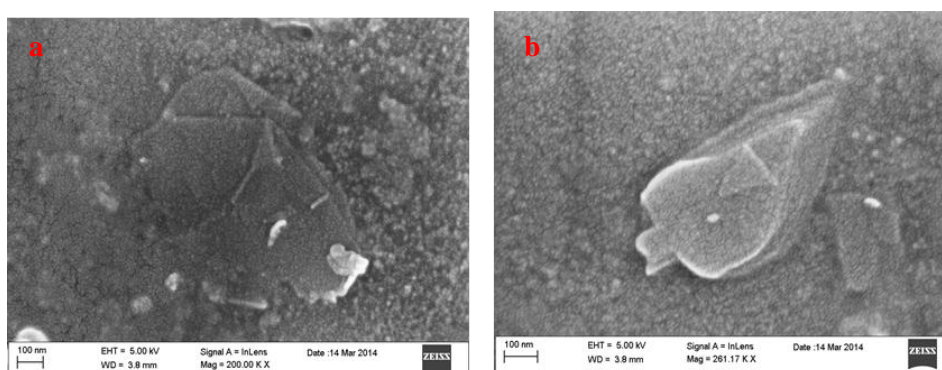


Figure10. FE-SEM of graphene sheets

[Figure 11](#) illustrates a morphological investigation of both GPVAMA and PVAMA hydrogels. The hybrid hydrogel reveals a different texture from the blank PVAMA hydrogel with pores size appearing to be smaller, which could be justified by the fact

Chapter II

that it represents a more complex network in which graphene is intercalated through the crosslinking of PEGPEPEMA to the PVAMA chains. However, the graphene sheets are hard to be distinguished within the polymeric network of the hydrogel. This is due from one side to the small content ratio of graphene with respect to the PVA (about 0.3% w/w), and from another side to the very low contrast with the polymeric matrix.

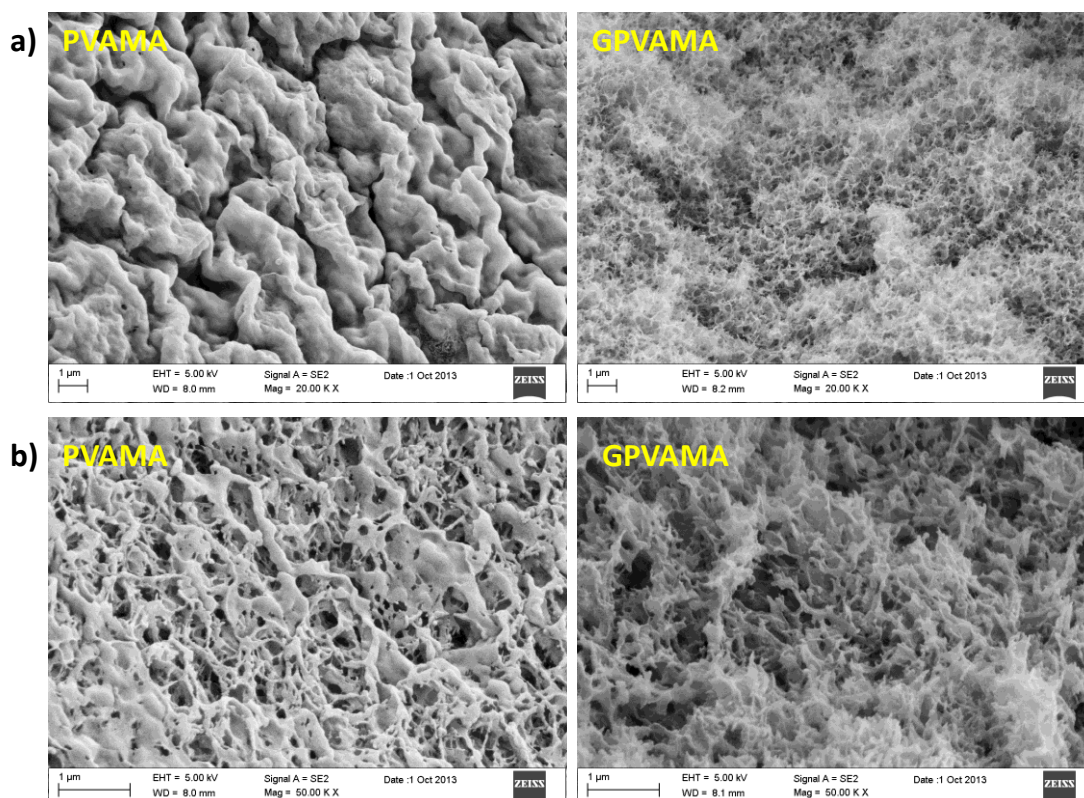


Figure 11. FESEM images of PVAMA and GPVAMA hydrogels at magnitudes of a) 20.00 KX, b) 50.00 KX. Scale bar is 1 μm.

3.7. Rheology:

Both G/PVAMA and PVAMA hydrogels exhibit a solid-like behavior and a frequency independent storage (G') and loss (G'') modulus under the linear regime (see [Figure 12a](#)). The increase in G' and G'' values for the hybrid hydrogel of about one order of magnitude as compared to the corresponding values of the blank hydrogel, represents an enhancement in the mechanical properties due to the incorporation of graphene despite its very small amount respect to the polymer matrix (0.3% w/w).

The rheological behavior of the hydrogels incorporating NiPAAm i.e. G/PVA-p(MA-co-NiPAAm) and PVA-p(MA-co-NiPAAm) was investigated at different temperatures

Chapter II

in order to assess an understanding of the hydrogels thermoresponsiveness. Polymerized NiPAAm (pNiPAAm) has in aqueous solution a lower critical solution temperature (LCST) at around 32-33°C, and when incorporated in a hydrophilic matrix, close to the physiological temperature, it triggers a volume phase transition temperature (VPTT).^[16,17] Hence, the systems incorporating the latter can be considered as thermoresponsive. Figure 12b show the storage modulus variation of both hydrogels as a function of the temperature ranging from 22 to 50°C. Increasing the temperature above the NiPAAm phase transition ($\approx 32-33^\circ\text{C}$), G/PVA-p(MA-co-NiPAAm) and PVA-p(MA-co-NiPAAm) shrink to dehydrated state and become more rigid, showing higher G' values. As in the case of G/PVAMA, incorporation of graphene leads to hydrogel reinforcement that shifts the G' of about 500 Pa.

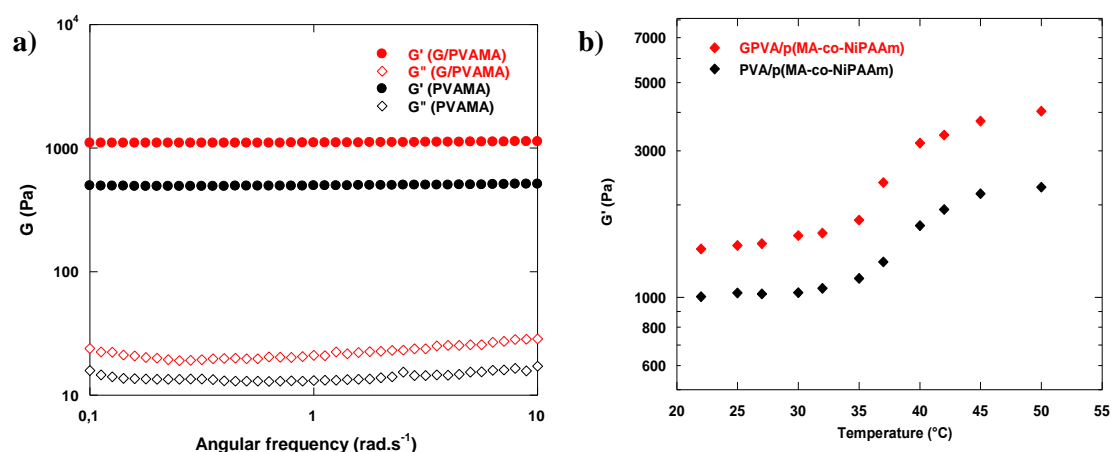


Figure 12. a) Frequency sweep measurement of viscous and elastic modulus in PVAMA and G/PVAMA hydrogels; b) Storage modulus, G' , vs. temperature of GPVA/p(MA-co-NiPAAm) and PVA/p(MA-co-NiPAAm) hydrogels.

3.8. Confocal laser microscopy:

The morphology of the PVA based hydrogels was characterized by bright field and confocal microscopy. Both G/PVAMA and PVAMA exhibited autofluorescence. However, dark zones exhibiting a quenching of fluorescence are observed in G/PVAMA, which can be attributed to graphene, contrarily to PVAMA (see Figure 13) where quenching is not observed. It should be noted that a slight quenching effect on the overall matrix occurs in the presence of graphene which could be due to an

Chapter II

electron energy transfer effect or to a non radiative decay of the polymeric matrix.^[18,19]

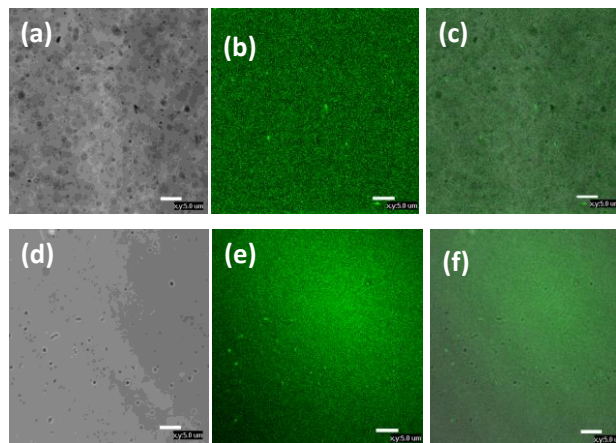


Figure 13. CLSM of hydrogel films, G/PVAMA bright field image (a), G/PVAMA fluorescence image (b), G/PVAMA merged image (c), PVAMA bright field image (d), PVAMA fluorescence image (e), PVAMA merged image (f). The scale barre is 10 μm .

3.9. Differential Scanning Calorimetry:

DSC was used to evaluate the effect of incorporating graphene into PVA hydrogel matrix on the crystal structure of the matrix. The results obtained herein highlight that PVA maintained a partial crystallinity even in the presence of a large amount of water, about 90 % (w/w). Moreover, the DSC thermograms, in both cooling and heating modes, show an increase in the crystallization and melting temperatures, as well as enthalpies, for the G/PVAMA with respect to PVAMA (see [Figure 14a](#) and [Table 2](#)). These results are attributed to an increase of the crystalline fraction in the polymer matrix of G/PVAMA and indicate that such entrapment of graphene influences the polymer matrix by acting as a nucleation agent in the crystallization process.^[20]

Chapter II

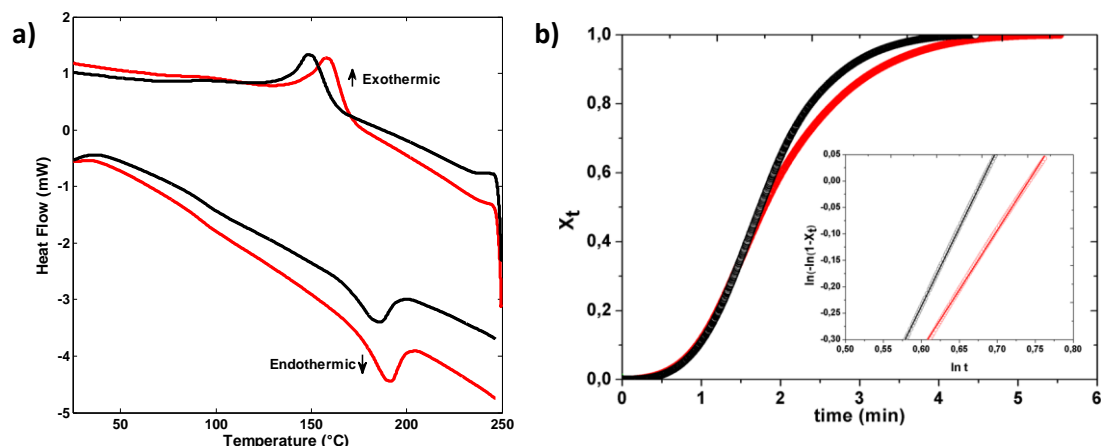


Figure 14. a) DSC thermograms of PVAMA (black) and G/PVAMA (red) hydrogels; b) Time dependence of the fraction of crystalline phase in PVAMA, black line, and G/PVAMA, red line. Inset: Analysis of the profiles according to the Avrami's model.

The analysis of the obtained DSC profiles allowed determination of the crystallization degree of the G/PVAMA hydrogel, $X(T)$, as a function of the temperature according to the following equation:

$$X(T) = \frac{\int_{T_0}^T \left(\frac{dH}{dT}\right) dT}{\int_{T_0}^{T_\infty} \left(\frac{dH}{dT}\right) dT} \quad (2)$$

where T_0 and T_∞ indicate the crystallization onset and the end temperatures, respectively. Assuming that in the experimental conditions the time lag between the sample and the furnace is negligible at the operative scanning rate, the change from temperature to time, $T \rightarrow t$, is obtained by:

$$t = \frac{T_0 - T}{\beta} \quad (3)$$

where β is the cooling rate of the experiment i.e $10^\circ\text{C}/\text{min}$.

Figure 14b illustrates the calculated crystallization vs time for PVAMA and G/PVAMA hydrogels. These profiles are commonly interpreted in the light of Avrami's nucleation-crystallization kinetic model according to the equation 4 below ^[21]:

$$X(t) = 1 - \exp[-(kt)^n] \quad (4)$$

Chapter II

Here, $X(t)$ describes the growth crystallization fraction in the crystalline phase of the polymer matrix over the time. The rate constant of the crystallization process and the Avrami kinetic exponent are defined by k and n parameters, respectively.

This model suggests that the growth rate of the crystalline phase k depends on the temperature and on the nucleation frequency, whereas n is a kinetic parameter with values ranging from 1 to 4 and reflecting the morphology of the crystalline domains and the nucleation frequency. The linearized form of eq 4 allows the determination of k and n :

$$\ln\{-\ln[1-X(t)]\} = \ln k + n \ln(t) \quad (5)$$

Table 2. DSC analysis and Avrami's parameters of G/PVAMA and PVAMA hydrogels

	ΔH_m (J/g)	T_m (°C)	ΔH_c (J/g)	T_c (°C)	k (min ⁻¹)	n
G/PVAMA	17.8	189.8	-25.3	159.4	0.2	2.1
PVAMA	16.5	185.6	-23.2	150.1	0.13	3

The determination of the values of k and n reported in table 2 confirm that graphene acts as a nucleation agent in the crystallization process of PVAMA matrix, which is linked to the viscoelasticity of the polymer, by increasing the number of the crystalline domains as well as their formation speed within the hydrogel network (see also inset Figure 14b).

Figure 15 illustrates the DSC profile of the hybrid thermoresponsive hydrogel i.e. G/PVA-p(MA-co-NiPPAm). The hydrogel exhibits a mean VPTT at about 33°C, which is in agreement with the results from rheology, the determined VPPT values from several measurements are summarized in table2.

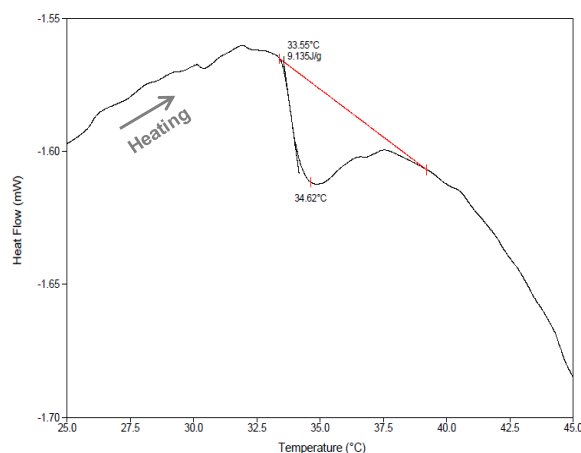


Figure 15. DSC thermogram of GPVA/p(MA-co-NiPAAm) hydrogel at 1°C/min and under 50 mL/min N₂.

Table 3. GPVA/p(MA-co-NiPAAm) hydrogel DSC analysis

Sample	m _{swollen} (mg)	m _{dried} (mg)	ΔH _m (J/g)	VPTT (°C)
1	26.6	1.9	13.6	32.9
2	24.7	1.7	11.0	34.0
3	23.8	2.0	18.3	32.2
4	22.8	1.3	9.1	34.6

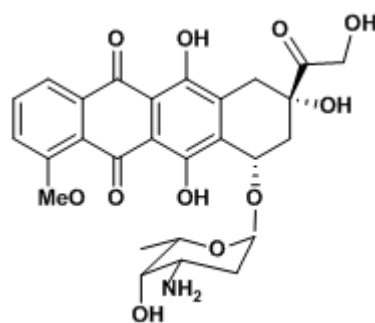
3.10. Doxorubicin loading and delivery kinetics:

On the base of the results obtained for the thermoresponsive hydrogel, we investigated whether the drug release properties of GPVA/p(MA-co-NiPAAm) hydrogel were influenced by the temperature using as model molecule the anti-cancer drug doxorubicin, DOX (see structure in Scheme 4). The graphene interaction with DOX was proved by studying fluorescence quenching effect according to the equation below:

$$\% \text{ Fluorescence Quenching} = \frac{I_{\text{pureDOX}} - I_{\text{DOX/Gr}}}{I_{\text{pureDOX}}} \times 100 \quad (6)$$

where I corresponds to the DOX maximum emission band at 550 nm.

Chapter II



Scheme 4. Chemical structure of the Doxorubicin anti-cancer drug model.

The NiPAAm VPTT affects the pores size of the matrix and then its permeability, whereas DOX can be stacked on the graphene by π - π interactions as shows the study of the DOX fluorescence quenching in the aqueous graphene/PEG-PEPEMA suspension ^[22] (see [Figure 16](#)).

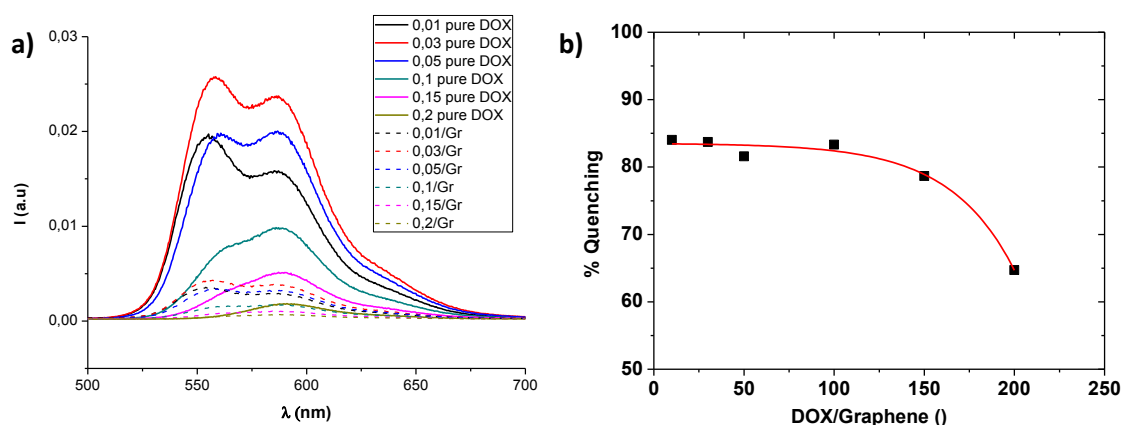


Figure 16. a) pure DOX (full lines) and DOX/Graphene (dashed lines) aqueous dispersions fluorescence spectra ; b) Quenching effect variation as function of DOX/Graphene content ratio (the red line is a guide for eyes).

[Figure 17a](#) illustrates that the amount of DOX released at physiological temperature, i.e. above VPTT, at equilibrium is higher than at RT. This increase is due to the shrinking of the hydrogel provoking a diminution of the pores size, which facilitates the release of the drug (see [Figure 16b](#))

Chapter II

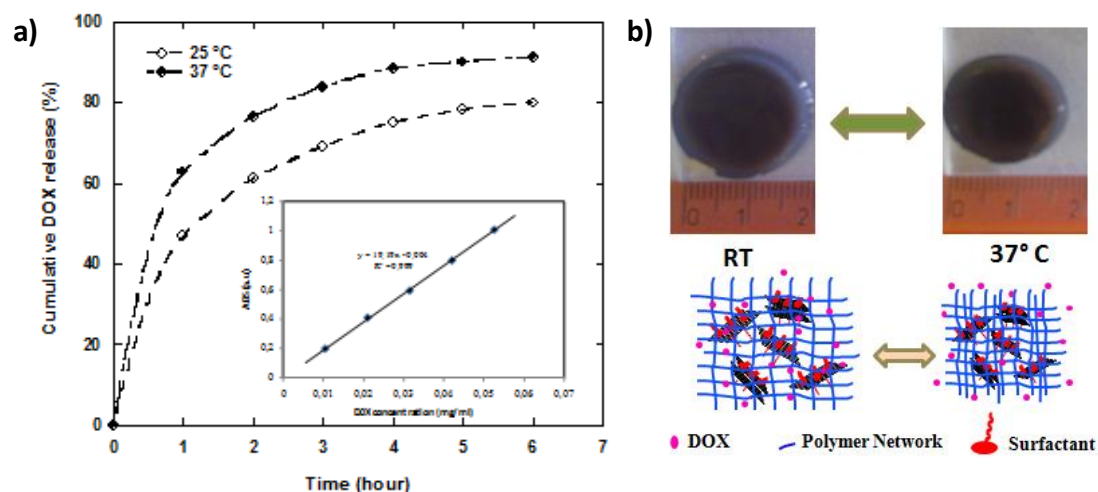


Figure 17. a) Doxorubicin cumulative release by GPVA/p(MA-co-NiPAAm) at 25 °C (empty symbols) and at 37 °C (filled symbols). The inset is the DOX calibration curve in PBS; b) Shrinking behavior of GPVA/p(MA-co-NiPAAm) at physiological temperature and the DOX release mechanism.

Conclusion

Few and single-layers graphene sheets with limited defects have been successfully exfoliated and then incorporated into methacrylated PVA chains by photocrosslinking the surfactant vinyl moiety, leading to a robust hybrid construct. It was also possible to include vinyl containing oligomers, such as NiPAAm for a shrinking assisted drug delivery application. Hence, the graphene based hydrogel exhibited in addition a thermoresponsivity displayed by a volume phase transition close to the physiological temperature, which was functional for the delivery of the anti-tumor drug Doxorubicin.

These results gave rise to the idea of including pristine graphene and take advantages of its mechanical and optical features for other, more specialized, microdevices which will be discussed in the following chapters.

Chapter II

References

- [1] Topel, Ö.; Çakır, B. A.; Budama, L.; Hoda, N. *J. Mol. Liq.* **2013**, *177*, 40–43.
- [2] Lotya, M.; Hernandez, Y.; Kin, P. J.; Smith, R. J.; Nicolosi, V.; Karlsson, L. S.; Blighe, F. M.; De, S.; Wang, Z.; Mc Goven, I. T.; et al. *J. Am. Chem. Soc.* **2009**, *131*, 3611–3620.
- [3] Fernandez-Merino MJ, Guardia L, Paredes JI, Villar-Rodil S, Solis-Fernandez P, Martinez-Alonso A, et al. *J Phys Chem C.* **2010**; *114*, 6426–6432.
- [4] Li, D.; Muller, M. B.; Gilje, S.; Kaner, R. B.; Wallace, G. G. *Nat. Nanotechnol.* **2008**, *3*, 101–105.
- [5] Ferrari, A. C.; Meyer, J. C.; Scardaci, V.; Casiraghi, C.; Lazzeri, M.; Mauri, F.; Piscanec, S.; Jiang, D.; Novoselov, K. S.; Roth, S.; et al. *Phys. Rev. Lett.* **2006**, *97*, 187401-187404.
- [6] Ferrari, A. C. *Solid State Commun.* **2007**, *143*, 47–57.
- [7] Malard, L. M.; Pimenta, M. A.; Dresselhaus, G.; Dresselhaus, M. S. Raman Spectroscopy in Graphene. *Phys. Rep.* **2009** *473*, 51-78.
- [8] Ni, Z.; Wang, Y.; Yu, T.; Shen Z. Raman Spectroscopy and Imaging of Graphene. *Nano. Res.* **2008**, *1*, 273 291.
- [9] Bracamonte, M. V.; Lacconi, G. I.; Urreta, S. E.; Foa Torre, L. E. F. On the Nature of Defects in Liquid-Phase Exfoliated Graphene. *J. Phys. Chem. C* **2014**, *118*, 15455–15459.
- [10] Frank, O.; Mohr, M.; Maultzsch, J.; Thomsen, C.; Riaz, I.; Jalil, R. ; Novoselov, K. S.; Tsoukleri, G.; Parthenios, J.; Papagelis, K.; Kavan, L.; Galiotis, C. Raman 2D-Band Splitting: Theory and Experiment. *ACS Nano* **2011**, *5*, 2231-2239.
- [11] Wang, P.; Zhang, D.; Zhang, L.; Fang, Y. The SERS Study of Graphene Deposited by Gold Nanoparticles with 785 nm Excitation. *Chem. Phys. Lett.* **2013**, *556*, 146–150.
- [12] Frank, O.; Tsoukleri, G.; Parthenios, J.; Papagelis, K.; Riaz, I.; Jalil, R.; Novoselov, K. S. ; Kalba, M.; Kavan, L.; Galiotis, C. Graphene under Unaxial Deformation : A Raman Study. *Brno, Czech Republic, EU*, **2011**, *9*, 21-23.
- [13] Krieger, U. K.; Zardini, A. A. Using dynamic light scattering to characterize mixed phase single particles levitated in a quasi-electrostatic balance. *Faraday Discuss.* **2008**, *137*, 377-388.

Chapter II

[14] Lotya, M.; Rakovich, A.; Donegan, J. F.; Coleman, J. N. Measuring the Lateral Size of Liquid-Exfoliated Nanosheets with Dynamic Light Scattering. *Nanotechnology* **2013**, *24*, 265703.

[15] Park, M. H.; Kim, T. H.; Yang, C. W. Thickness Contrast of Few-Layered Graphene in SEM. *Surf. Interface Anal.* **2012**, *44*, 1538–1541.

[16] Tauer, K.; Gau, D.; Schulze, S.; Völkel, A.; Dimova, R. Thermal property changes of poly(N-isopropylacrylamide) microgel particles and block copolymers. *Colloid. Polym. Sci.* **2009**, *287*, 299-312.

[17] Ghugare, S. V.; Chiessi, E.; Telling, M. T. F.; Deriu, A.; Gerelli, Y.; Wuttke, J.; Paradossi, G. Structure and Dynamics of a Thermoresponsive Microgel around Its Volume Phase Transition Temperature. *J. Phys. Chem. B*, **2010**, *114*, 10285–10293.

[18] Xu, Y.; Liu, Z.; Zhang, X.; Wang, Y.; Tian, J.; Huang, Y.; Ma, Y.; Zhang, X.; Chen, Y. A graphene hybrid material covalently functionalized with porphyrin: Synthesis and optical limiting property. *Adv. Mater.* **2009**, *21*, 1275-1279.

[19] Ito, F.; Kakiuchi, T.; Sakano, T.; Nagamura, T. Fluorescence properties of pyrene derivative aggregates formed in polymer matrix depending on concentration. *Phys. Chem. Chem. Phys.* **2010**, *12*, 10923–10927.

[20] Kuilla, T.; Bhadra, S.; Yao, D.; Kim, N. H.; Bose, S.; Lee, J. H. Recent Advances in Graphene based Polymer Composites. *Prog. Polym. Sci.* **2010**, *35*, 1350-1375.

[21] Harnisch, K.; Muschik, H. Determination of the Avrami Exponent of Partially Crystallized Polymers by DSC- (DTA-) Analyses. *Colloid & Polymer Sci.* **1983**, *261*, 908-913.

[22] Yang, X.; Zhang, X.; Liu, Z.; Ma, Y.; Huang, Y.; Chen, Y. High-efficiency loading and controlled release of doxorubicin hydrochloride on graphene oxide.. *J. Phys. Chem. C.* **2008**, *112*, 17554–17558.

Chapter III:

Photoacoustic Imaging in Biomedicine and Hybrid Contrast Agents

Chapter III

Introduction:

This chapter introduces the historical origin of photoacoustic effect and its application in biomedicine in addition to the basic physical concepts related to its generation mechanisms and the essential elements involved in photoacoustic imaging (light propagation in tissue, contrast agents, principles of optically scattering media). Also, the principles of ultrasound imaging are introduced; it is necessary to provide the details of this medical technology as the main theme in the next chapter will be the photoacoustic application of hybrid graphene-microbubbles which also have potential for ultrasound imaging. The goal is to give the main physical elements that will allow understanding of the studied systems in this manuscript. The last section discusses both contrast agents used regularly in ultrasound imaging and exogenous hybrid contrast agents in photoacoustic imaging suggesting why graphene could be advantageous.

1. Photoacoustic effect history:

The photoacoustic effect, called also optoacoustic effect, was first discovered in 1880 by Alexander Bell during an experiment of long-distance sound transmission, and whose results led to the invention of the spectrophone device.^[1] The discovery consisted in observing a direct production of sound waves from a solid sample upon its exposition to rapidly interrupted sunlight beam by using a rotating slotted wheel. The intensity of sound waves production was found to be depending on the type of material, and consequently on its ability to absorb light energy. Moreover, this effect was also produced in liquid and gas samples.^[2] The application of the photoacoustic effect had afterwards to wait until the development of sensitive sensors and intense light sources. Since then research and applications grew faster and wider, including the biomedical field, acquiring higher detection sensitivity.

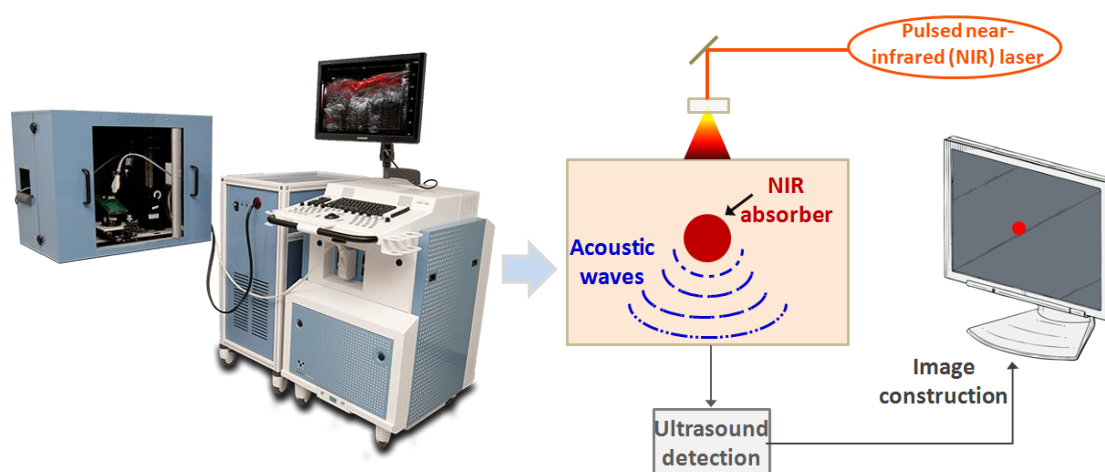
2. Concept of photoacoustic imaging (PAI):

Photoacoustic imaging is a hybrid fast developing preclinical modality in the biomedical field, which has been considered in the last decade and is based on the photoacoustic effect allowing structural, functional and molecular imaging. PAI combines therefore both optical and ultrasound imaging techniques.^[3-4] In order to excite MHz ultrasound (US) waves in soft tissues, non-ionizing radiations of short

Chapter III

laser or radio-frequency (rf) pulses are often used. Briefly, PAI operating principle consists on irradiating a target tissue with a pulsed nanosecond timescale electromagnetic radiation, usually a NIR pulsed laser. The latter absorbs the radiation energy and converts it into acoustic waves by thermal expansion and subsequent relaxation. As the waves are detected with an US transducer placed directly around the tissue to diagnose, a signal processor allows then for the construction of the image (see scheme 1).^[3-5] The use of NIR laser in PAI rather than UV, visible light or rf pulses is because the spectral range from 600 to 900 nm is the region where water and blood absorb the less and offers the greatest penetration depth in the biological tissues. In addition, the fact of using a non-ionizing radiation does not destroy the properties of the biological tissue under diagnosis and hence makes PAI safe for humans with respect to other radiological imaging techniques, and ideal for in vivo applications.^[3,4,6] Moreover, the dependence of PA signals from the physical parameters of biological tissues is well defined, which permits the quantification of various physiological parameters such as the oxygenation of hemoglobin.

The main assets of PAI, discussed in the following sections, are the penetration depth, resolution, and contrast.



Scheme 1. Overview of photoacoustic imaging instrument from Vevo Lazr by VisualSonics (left); conceptual scheme of PAI system (right).

The photoacoustic signal is determined by the NIR absorption and scattering properties, the thermal properties, including the thermal diffusivity and thermal

Chapter III

expansion coefficient, and the elastic properties of the sample. The absorption property is of primary importance due to the contrast provided in biological tissues. For this reason, the properties of the target tissue are important in PAI as the pressure of a generated photoacoustic wave increases with the variation of the heat resulting from the absorption of the NIR radiation energy. ^[4]

The initial pressure in (Pa) can be expressed according to the equation (1):

$$P \propto \Gamma(T) \sigma \mu_a F$$

where Γ is the temperature-dependant Grueneisen parameter, σ is the heat conversion efficiency ($0 \leq \sigma \leq 1$), μ_a (cm^{-1}) is the optical absorbance coefficient, and F (W/m^2) is the optical fluence. The PA signal intensity depends in a proportional way on these parameters.

However, the photoacoustic wave can be described following the equation (2):

$$\frac{1}{v_s} \frac{\partial^2 p(\vec{r}_0, t)}{\partial t^2} - \nabla^2 p(\vec{r}_0, t) = \frac{\beta}{C_p} \frac{\partial H(\vec{r}, t)}{\partial t} \quad (2)$$

where v_s (m/s) is the wave velocity in the medium; $p(r, t)$ (Pa) is the PA pressure at the location r and time t ; β (dV/k) is the volumetric thermal expansion coefficient, C_p (J.K.kg^{-1}) is the heat conversion capacity; and H is the heating function of the thermal energy conversion. The left side of equation (2) is the generated PA wave, whereas the right side is the heating source variation.

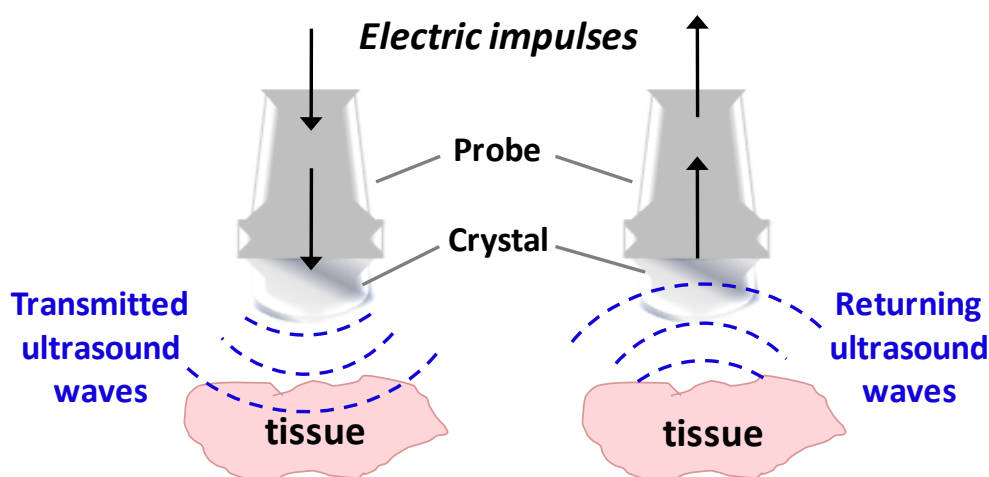
3. Ultrasound and photoacoustic imaging in biomedicine:

3.1. Ultrasound imaging (US):

Ultrasound imaging is the most used diagnostic tool spread through diverse fields in medicine such as cardiology and gynecology, being a low-cost and easy-to-handle technique. The medical application of this modality goes back to the 50's. ^[7,8] The principle of US imaging is based on the sonar in the same way as it is used by bats, ships, submarines, etc; it consists of the backscattering of a sound wave produced by a transducer after it was interacting with a human tissue. ^[9,10] The transducer probe presents therefore the main part of an US machine as it generates and receives

Chapter III

sound waves which are often in the frequency range from 2 to 20 MHz. The produced ultrasound waves originate from the mechanical oscillations of numerous crystals in the transducer, which are excited by electrical pulses using the piezoelectric effect discovered by the Curie's in 1880.^[11] The transducer converts then the electrical energy into mechanical vibrations resulting in a sound. The ultrasound pulses sent from the latter, propagate through different tissues, and then return to the transducer as reflected echoes. The returned echoes are converted back into electrical impulses by the transducer crystals and are further processed in order to construct the ultrasound image (see scheme2).



Scheme 2. Representation of Ultrasound imaging principle

The measuring of these echoes waves allows for the determination of how deep is the target tissue in addition to its size and shape. Hence by using US it is possible to detect abnormalities such as tumors or changes in the organs and tissues.^[12]

The important parameters of ultrasound scattering information are attenuation and velocity, which are the decay rate of the US amplitude as the wave travels within the tissue and its speed, respectively. The acoustic attenuation, usually expressed in dB/m, in a colloidal suspension yields information about particle size distribution on which the resonance frequency is dependent, whereas the velocity is proportionally affected by the density and elasticity of the medium.

Chapter III

Knowledge of these factors allows us to determine the adjustment needed to improve the imaging quality in order to obtain the maximum of the tissue information at the desired depth.^[13]

Nonlinear effects also can offer an enhanced US contrast imaging due the production of harmonics of higher orders, i.e. second harmonic, principally by microbubbles that have been injected into blood vessels, and the inherent nonlinearity of the tissue. The microbubbles as ultrasound contrast agent (UCA), will be discussed in section 4.1 of this chapter.^[14]

3.2. Photoacoustic imaging vs. ultrasound imaging:

Photoacoustic and ultrasound imaging are two complementary modalities. In fact, an US equipment can be modified to provide both PA and US imaging ability by simply installing into it a pulsed laser source.^[3-5]

In PAI, the acoustic waves in the medium are induced by laser irradiation, so the US transducer is only used to receive the generated PA waves and does not transmit acoustic waves. For this reason, the transmitting function of a clinical US imaging system must be blocked in order to enable acquisition of a PA image. Furthermore, the beam forming algorithm must be modified to enable one-way detection by making accessible the raw data of the received PA signal.^[4]

3.2.1 Contrast:

The optical contrast mechanism in PAI is based on the differences in absorption features between the diverse tissue components. As described above in section 2, pulsed laser light is incident on the tissue surface and depending on the selected wavelength the light penetrates more or less deeper to the target. The scattered and absorbed light is multiplied by specific absorbing agents which can be either endogenous (hemoglobin, melanin, etc) or exogenous (chromophore molecules as, indocyanine green, methylene blue, etc, or plasmonic nanoparticles).^[3,5,15]

Hence, the optical absorption capacity inside the tissue, as the main PAI contrast feature, lends to the visualization of anatomical features rich of chromophores such as hemoglobin, lipids and water. Here, the hemoglobin is preeminent to consider

Chapter III

since its absorption coefficients for both oxygenated and deoxygenated states are orders of magnitude (about two) higher than the water and lipids which are present in surrounding tissues components and blood vessels. Consequently, hemoglobin is strongly preferred as its absorption makes possible high contrast visualization of the vasculature using PAI: in the visible spectral region, hemoglobin absorption is further increased with respect to the other chromophores. Furthermore, the differences in the absorption spectra of the two states of hemoglobin, i.e. oxygenated and deoxygenated, allow to measure blood oxygenation by acquiring images at multiple wavelengths and applying a spectroscopic analysis. In this way, the endogenous contrast is enough to image functional as well as structural vasculature and therefore to follow a tumor angiogenesis.^[3,5,16,17,18]

However, for the NIR spectral region extending from 650 to 900 nm, where penetration depth is enhanced, the absorption coefficients of hemoglobin for both oxygenated and deoxygenated states become low, thus requiring the use of exogenous contrast agents.^[3,5,16]

3.2.2 Penetration depth:

In PAI, two parameters limit the penetration depth inside tissues which are the optical and the acoustic attenuations. However, it is the optical attenuation that dominates and it is strongly depending on the wavelength and absorption and scattering coefficients (see [Figure 1](#)).

Chapter III

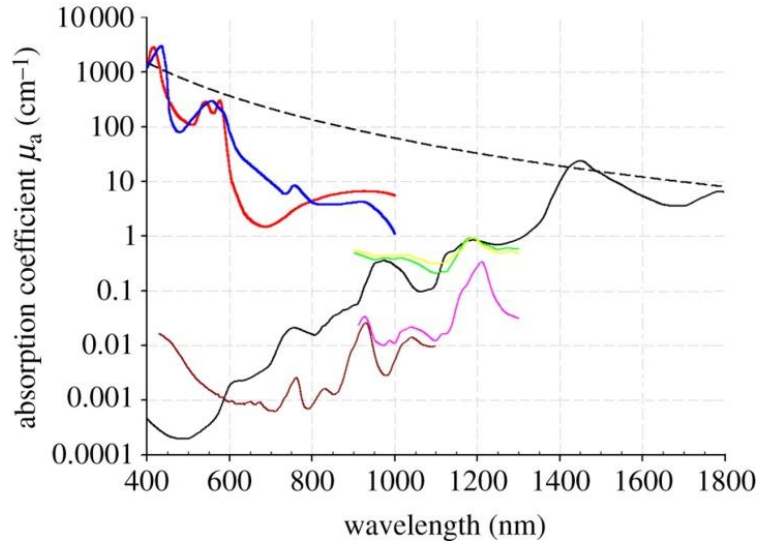


Figure 1. Vis-NIR absorption spectra of main chromophores in biological tissue: Water (black), lipids (brown), oxygenated hemoglobin (red) and deoxygenated hemoglobin (blue), melanin (dashed line), collagen (green),lipid (purple). Copyright Interface Focus (2011) 1, 602–631

The laser irradiation penetration depth in the tissues is characterized by the effective attenuation coefficient μ_{eff} which derives from diffusion theory as expressed in equation (3) :^[3]

$$\mu_{\text{eff}} = \sqrt{3\mu_a(\mu_a + \mu_s')} \quad (3)$$

where μ_a is the absorption coefficient and μ_s' is reduced scattering coefficient.

Inside biological tissues composed of different components μ_a can be defined as the sum of global absorption of each constituent. According to the [Figure 1](#), all chromophores naturally present in the tissue show a wavelength dependence of their absorption coefficients which decreases in the optical window above 650 nm. The intensity of laser irradiation decreases exponentially with the depth as the light diffuses inside the tissue to diagnose. In the NIR spectral region water and blood absorb the least allowing for the best penetration efficiency due to the fact that light can propagate within the tissue before being totally absorbed. In general, each of the total light and sound attenuations are at least some units per centimetre. This consists of one of the major challenges in PAI since penetrating several centimetres in tissue undergoes a signal attenuation of several orders of magnitude resulting in

Chapter III

extremely weak ultrasound signals to be detected. Nevertheless, combining the optimum choice of wavelength, transducer parameters and signal processing could lead to a penetration of several centimeters. It has been demonstrated that it is possible to reach 4cm depth in human breast by using a laser excitation wavelength of 800 nm.^[19] Moreover, in other in vitro studies using tissue mimicking phantoms and ex vivo tissues, the use of exogenous NIR contrast agents allowed for a penetration to a depth up to more than 5 cm.^[20]

3.2.3 Spatial Resolution:

The spatial resolution refers in general to the quality of the image that can be obtained and corresponds to the number of independent pixels per each inch. In the biomedical imaging systems, it is the ability to discriminate between two adjacent high-contrast objects within the analyzed tissue. As in US imaging, the spatial resolution for PAI is linked to the frequency of the acoustic wave arriving to the transducer, but does not depend on the light diffusion behavior in the tissues to reach the absorbing components. Thus, even if the multiple optical scattering in the tissue limits the intensity of the incident light to the chromophore-rich zones, this has no influence on the resolution of the image which is comparable to the US imaging one. ^[5,16]

Depending on the spectral features of the NIR optical absorber, the nanosecond pulses of the excitation laser often used in PAI can result in extremely broadband acoustic waves with a frequency range extending for several tens of MHz. The maximum frequency of a generated photoacoustic wave is limited by the weaker propagation of the waves owing to the frequency dependent attenuation exhibited by soft tissues. Under these circumstances, spatial resolution of the acoustic signal scales with depth. Nonetheless, the detector bandwidth and the area over which PA signals are recorded are some factors that could also have an impact on the spatial resolution in practice. ^[3-5]

Chapter III

4. Hybrid Contrast agents:

The contrast agents for US imaging and PAI have been studied separately. Since PAI combines both ultrasound and optical imaging, hybrid contrast agents to enhance the diagnosis were designed to support a dual-imaging modality, i.e. to exhibit both an ultrasound and a photoacoustic contrast. These are essentially ultrasound contrast agents (UCAs) decorated with exogenous chromophores or metallic nanoparticles (NPs).^[15,21-25]

4.1 Specific contrast agents for ultrasound imaging:

The need of contrast agents in US imaging (UCAs) is to overcome the reducing of the waves intensities in order to reach deeper zones to the tissue. The use of UCAs, which are mainly gas bubbles, has been developed in the last decades. The first discovery of the potential of gas bubbles as UCA was about 40 years ago, when accidentally an injection of indocyanine green (ICG) resulted in a signal increase while measuring cardiac output.^[26] The subsequent investigation showed that the observed phenomenon was caused by the formation of tiny air bubbles at the catheter tip at the moment of the injection. This is explained as air, or gas in general, is less dense than the tissue components, thus the sound travels with a slower speed through it. Therefore the difference in sound velocity creates an acoustic mismatch between bubbles and the tissues. Later on, it was developed the new generation of micrometer size stabilized gas bubbles, called microbubbles, which are generally formed by a spherical cavity (shell) filled with gas (air, perfluorocarbon, sulfur hexafluoride SF₆) and coated with phospholipids, surfactants, proteins or polymers.^[27,28] These MBs are excellent scatterers of sound in liquids and are able to produce strong ultrasound backscattering signals due to the differences in density and compressibility between the gas core and the tissue; hence their use to increase the blood echogenicity and to improve the quality of ultrasound image. Depending on the gas nature and the chemical properties of the shell, microbubbles are more or less stable and their physical properties change as well; which affects the produced contrast signal efficiency.^[29,30] Moreover, MBs resonance frequency is related to their radius and the shell elasticity according to the equation of Rayleigh Plesset:^[31]

Chapter III

$$f_0 = \frac{1}{2\pi R_0} \sqrt{\frac{1}{\rho L} \left[3\gamma P_0 + \frac{2(3\gamma-1)\sigma}{R_0} + \frac{4\chi}{R_0} \right]} \quad (4)$$

where f_0 is the resonance frequency, R_0 is the microbubble radius, γ is the specific heats of the gas core, ρL is the density of surrounding liquid, P_0 is the ambient fluid pressure, σ is the surface tension at the bubble-liquid interface and χ is the elasticity of the shell.

In addition to the physical properties of microbubbles, their US response depends primarily on the applied amplitude and intensity of the ultrasonic wave. The MBs can follow a “stable” or an inertial “cavitation” regime: at low pressure the MBs grow in volume, whereas at high pressures their volume is diminished. When polymer shelled MBs crack or lipid shelled MBs burst releasing their content (gas), the pressure exerted is called the peak negative pressure (PNP). This destruction mechanism can be translated by fatigue affecting the microbubble shell. PNP should be high enough so that the MBs do not crack too early, but not so high for the safety of the tissue. This is the reason why the ratio between the peak negative pressure and the square root of the ultrasound wave central frequency, called mechanical index (see [equation 5](#)), MI, should be below 1.9 as approved by the Food and Drug Administration.^[32]

$$MI = \frac{PNP}{\sqrt{f_c}} \quad (5)$$

At very low acoustic power or PNP (mechanical index <0.05–0.1), microbubble oscillates in a linear at the same frequency of incident ultrasound, reflecting the fundamental frequency and enhancing the scattering coming from blood. At higher mechanical index of 0.1–0.3, the microbubble becomes to oscillate in a nonlinear manner (nonlinear response), i.e. asymmetrically, backscattering a variety of frequencies (harmonic) as it liberates acoustic frequencies corresponding to both its fundamental and linear multiples. Higher acoustic pressures (mechanical index > 0.3–0.6) result in unstable oscillations leading to the microbubbles cracking

Chapter III

accompanied with high-intensity backscatter response (see Figure 2). This process corresponding to the “inertial cavitation” creates high local gradient of temperatures that harm the tissue and could be used therefore for tumors therapy. [32,33]

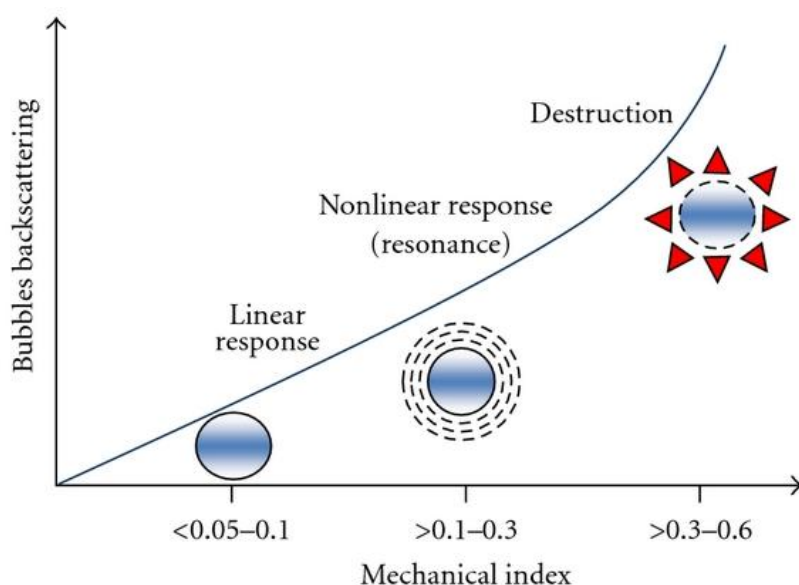


Figure 2. Dependence of microbubbles behavior on the amplitude of ultrasound to which they are exposed. Copyright (Greco et. al. *Journal of Biomedicine and Biotechnology* 2012)

In summary, the MBs features as UCAs must meet with specific requirements such as injectability, which is related to the size distribution limited by the diameter of capillaries to about $10\ \mu\text{m}$, scattering efficiency defined by their high density compressibility difference with the medium, biocompatibility and presence of reactive functionalities at the shell surface to allow a therapeutic potential in addition to the diagnostic function. To this regard, usually polymer shelled microbubbles are expected to be less echogenic than the lipid ones. However, as recently reported, PVA MBs, having acoustic properties comparable with the lipid counterpart, represents a potential UCA. The acoustic properties of the PVA shelled MBs are due to many factors, among which the water plasticizer action on the polymer shell. PVA shell is indeed a polymer network with high water content, about 70 % (w/w) and this increases the shell elasticity, bringing the acoustic performances of a PVA microbubbles close to those of a lipidic ones. [34]

An additional requirement is the MBs stability which defines their shelf life as well as their circulation life once injected. Every interface made of gas/liquid or liquid/liquid

Chapter III

exhibits a surface tension because of disruption of cohesive intermolecular forces and hence it shows an overpressure inside a microbubble. For a spherical interface with infinitely thin shell, Laplace formula (see [equation 6](#)) is valid:

$$\Delta P = P_{inside} - P_{outside} = \frac{2\sigma}{r} \quad (6)$$

where P_{inside} and $P_{outside}$ are the total pressure inside and outside the microbubble, respectively; σ is the surface tension of the gas/liquid interface and r is the microbubble radius.^[35]

The overpressure increases the gas solubility at the interface and leads to microbubbles disappearing rapidly, which is the main issue of air-filled MBs. However for PVA shelled MBs with air core, the stability is not an issue as for the phospholipids based MBs that require to be filled with hydrophobic gasses such as PFC or SF₆ to increase their shell stability. In PVA MBs the shell is stabilized by the chemical junctions crosslinking irreversibly the polymer chains in a network and this structural feature makes the core stability independent from the gas nature.

Moreover the PVA microbubbles are characterized by a very narrow size distribution and have also shown a potential in theranostic; being chemically highly versatile due to the presence of hydroxyl and aldehyde groups, their surface is an adequate platform for drug loading, such as doxorubicin, DOX, whose release can be guided by focused ultrasound. Derivatization with molecules promoting active targeting, such as folic acid, hyaluronic acid, RGD peptides, antibodies such as α -ICAM or α -VEGF, is easily accomplished either by acetylation, reductive amination of their available aldehyde groups, or by EDC chemistry to introduce a ligand with biospecific activity in order to increase their accumulation on pathological tissues.^[36-38]

4.2 Specific contrast agents for photoacoustic imaging:

In PAI, both endogenous contrast agents and a variety of exogenous moieties previously mentioned and absorbing in the NIR optical window from 650 to 900 nm

Chapter III

provide additional sources of spectrally selective PA contrast agents to be used for image disease-specific receptors (see [Table 1](#)). These latter mainly comprise organic dyes such as indocyanine green (ICG) and methylene blue which are already used clinically in some circumstances, or nanostructures such as metallic nanoparticles or shells that are reported in several studies but are currently limited to preclinical use. [15,18,23,24,39] Metal nanoparticles (NPs) of various geometries, such as gold nanorods and silver nanoplates, are of interest as their plasmon resonance absorption cross sections can be orders of magnitude higher than dye molecules and for the tunability of their peak absorption to NIR wavelengths as their shape changes. [40] Besides, the large absorption cross section exhibited by Au NPs may lead to a partial melting upon their irradiation with the pulsed laser. [41]

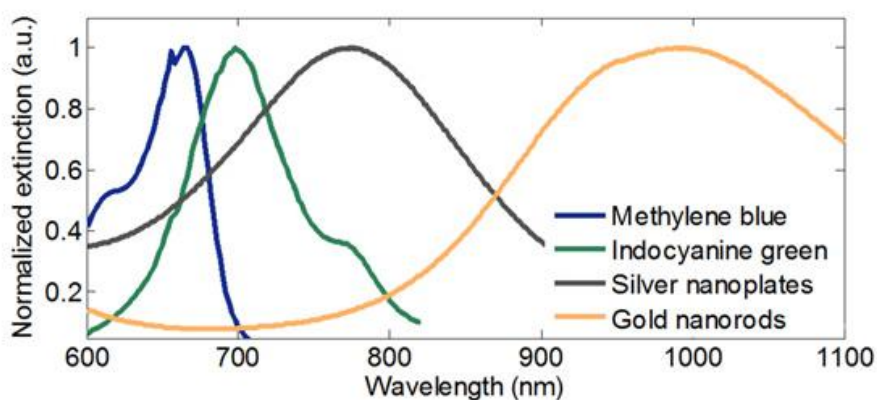


Figure 3. Absorption peaks of the common exogenous contrast agents in the PAI optical window. *Copyright Trends in Biotechnology (2011) 29, 213-221*

Ideally, PAI contrast enhancers are characterized by exhibiting a high molar extinction coefficient maximizing the amount of absorbed light; a characteristic absorption spectrum in the NIR specific range to maximize penetration depth by avoiding the strong absorption of intrinsic chromophores as shown in [Figure 3](#); a high photostability and efficient conversion of light into heat energy to produce acoustic waves. The photostability is indeed a major problem which makes organic NIR dyes not often appropriate as they degrade few minutes after being exposed to the laser energy used for imaging due to photobleaching.

However, in addition to these commonly studied chromophores addressing PAI, graphene derivatives i.e. GO and RGO were also investigated in recent studies for

Chapter III

their potential as contrast agents ^[42,43]. The interest in graphene for PAI, that could be advantageous with respect to other exogenous contrast agents, is due to its high thermal stability in addition to its appealing optical features as discussed in Chapter 1 section 1.2.4, exhibiting quasi-independent absorbance from the wavelength, from the visible to NIR, and providing therefore a wide suitable window for enhancing the photoacoustic contrast and penetration in the tissues.

Nonetheless, it is worth to mention that the optical absorbance efficiency is dramatically decreased in GO due to the induced structural defects on the graphene geometry (See Figure 4); in RGO, stability in physiological media is an issue as the major part of hydrophilic groups hindering the layers aggregation has been removed from GO surface during the reduction process. Some researchers were overcoming the GO absorption loss by coupling it to ICG ^[44] or plasmonic nanoparticles. A study by Moon *et. al.* reported recently the coupling of GO and gold nanorods to enhance PA signals;^[45] however such architecture may have not yet disclosed toxicological effects. Hence, in order to obtain improved graphene-based PAI enhancer materials, it is important that the original properties of graphene are preserved.

The discussed exogenous contrast agents for PAI can be introduced to the design of ad-hoc advanced platforms for dual or multi-modal imaging (see table 2) when coupled to microbubbles/microcapsules/droplets by chemical anchoring, surface decoration or encapsulation. Incorporation of hybrid systems ensures both contrast agents to circulate together, thus they can be simultaneously detected.

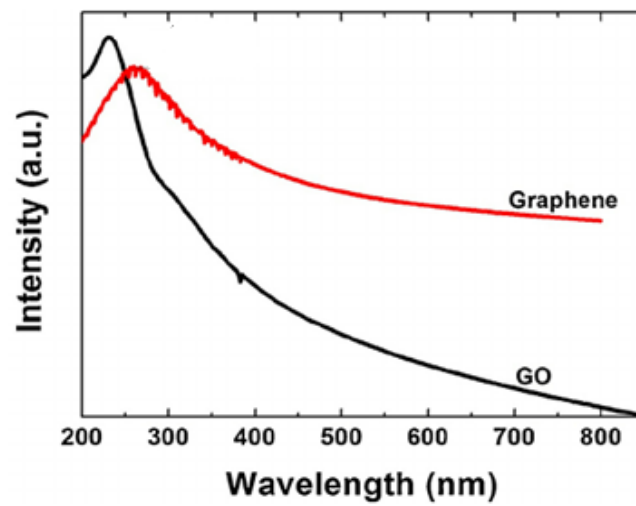


Figure 4. Graphene and GO UV-vis absorbance spectra. *Copyright (Journal of Industrial and Engineering Chemistry (2014) 20, 2883–2887)*

Table 1. Exogenous photoacoustic contrast agents discussed in the recent literature

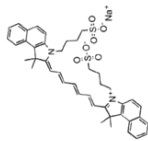
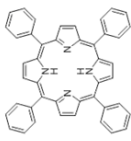
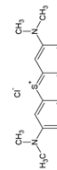


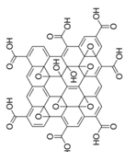

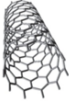
NIR dye	Chemical structure	Absorption peak	Size	Applications	Advantages	Disadvantages	References
Indocyanine green (ICG)		790 nm	< 2 nm	Fluorescence imaging, PAI	<ul style="list-style-type: none"> • Low toxicity and clinically approved • Good tissue penetration • Good biodistribution 	<ul style="list-style-type: none"> • Photoinstability • Poor solubility and aggregation • Short circulation lifetime 	[23, 46]
Porphyrin (TPP)		650 nm	< 2 nm	PAI in vitro	<ul style="list-style-type: none"> • Good photophysical properties • Chemical versatility for further derivatization 	<ul style="list-style-type: none"> • Photoinstability • Short circulation lifetime • Photosensitization of toxic singlet oxygen in oxygenated environments 	[25]
Methylene Blue		677 nm	< 2 nm	Sentinel lymph node identification	<ul style="list-style-type: none"> • Low toxicity and clinically approved 	<ul style="list-style-type: none"> • Photoinstability • Short circulation lifetime 	[24, 46]
Gold nanorods		790 nm (shifts depending on the particles length)	Diameter: 10 nm Length: 40-60 nm	PAI, conjugation with HER2 and EGFR for cancer imaging, photothermal therapy	<ul style="list-style-type: none"> • Good chemical and physical vesatility 	<ul style="list-style-type: none"> • Toxicity concerns • Poor biodistribution • Low homogeneity • Difficult quantification 	[18, 41, 46]
Silver nanoplates		600-1200 nm	100-200 nm	Imaging and photothermal cancer therapy	<ul style="list-style-type: none"> • Good chemical and physical vesatility 	<ul style="list-style-type: none"> • Toxicity concerns • low stability in physiological media 	[47,48]
Graphene oxide		200-1200 nm	100-500 nm	PAI in vitro and in vivo, photothermal therapy	<ul style="list-style-type: none"> • High and stable dispersibility in aqueous solutions • High chemical versatility • Wide NIR absorption window 	<ul style="list-style-type: none"> • Low absorption at NIR • Toxicity for doses > 50 mg/kg 	[42,43,49]
Reduced graphene oxide		200-1200 nm	100-500 nm	PAI in vitro	<ul style="list-style-type: none"> • Strong NIR absorption in a wide range • Good chemical versatility 	<ul style="list-style-type: none"> • Low water stability and aggregation 	[42]
Single walled carbon nanotubes (SWNT)		690 nm	Diameter: 1 nm Length: 100-300 nm	PAI in vitro and in vivo	<ul style="list-style-type: none"> • High surface area to volume ratio • Efficient binding to molecular targets 	<ul style="list-style-type: none"> • Low absorbance efficiency respect to graphene derivatives and other chromophores and metal nanoparticles 	[50]

Table 2. Hybrid contrast agents for dual-imaging: PAI and US

Hybrid contrast agent	Shell type	Size (nm)	Absorption peak (nm)	Reference
Au MBs	Protein (Human serum albumin)	100-1000	760	J Biomed Opt. 2012, 17, 045001
Dye-loaded perfluorocarbons nanoparticles	Phospholipids	220	750-800	ACS Nano, 2011, 5 (1), pp 173–182
Plasmonic liposomes	Phospholipids	100-200	800	Biomed. Opt. Express. 2011, 2,385–396
Triggered nanodroplets	Surfactant (Zonyl FSO fluorosurfactant)	300	500-800	Biomed Opt Express. 2014 Sep 1; 5(9): 3042–3052.
Porphyrin shell MBs	PEGylated Lipids	2000-3000	824	J. Am. Chem. Soc. 2012, 134, 16464–16467
Graphene oxide – AuNPs modified microcapsules	Polymer (Poly-lactic acid)	1000-2000	400-1000	Y. Jin et al. Biomaterials 34 (2013) 4794e4802

5. Hypothesis and aims:

Following the concept described in chapter II our goal consists in the formulation of pristine graphene interfaced to acoustic contrast poly(vinyl-alcohol)-shelled microbubbles platforms; a construct expected to exhibit high NIR absorption in a wide range of the optical window used for PAI, and therefore a more efficient photoacoustic responsiveness with respect to the other dyes discussed in this chapter. The rationale behind the choice of PVA microbubbles lies in their stability, biocompatibility and efficient use as an ultrasound contrast agent (UCA) in addition to their high chemical versatility.

Chapter III

References

- [1] Bell, A. G. On the production and reproduction of sound by light. *Am. J. Sci.* **1880**, *118*, 305.
- [2] Tyndall, J. Action of an Intermittent Beam of Radiant Heat upon Gaseous Matter. *P. Roy. Soc. Lond.* **1880**, *31*, 206–211.
- [3] Beard, P. Biomedical Photoacoustic Imaging. *Interface Focus* **2011**, *1*, 602–631.
- [4] Kim, J.; Lee, D.; Jung, U.; Kim, C. Photoacoustic imaging platforms for multimodal imaging. *Ultrasonography* **2015**, *34*, 88-97.
- [5] Xua, M.; Wangb, L. V. Photoacoustic Imaging in Biomedicine. *Rev. Sci. Instrum.* **2006**, *77*, 041101.
- [6] Mallidi, S.; Luke, G. P.; Emelianov, S. Photoacoustic Imaging in Cancer Detection and Treatment Guidance. *Trends Biotechnol.* **2011**, *29*, 213–221.
- [7] Goldman, D. E.; Hueter, T. F. Tabular Data of the Velocity and Absorption of High Frequency Sound in Mamalian Tissues. *J. Acoust. Soc. Am.* **1956**, *28*, 35-37.
- [8] Meyers, W. J.; Fry, F. J.; Fry, L. L.; Dreyer, D. F.; Schultz, R. F. Noyes. Early Experiences with Ultrasonic Irradiation of the Pallidofugal and Nigral Complexes in Hyperkinetic and Hypertonic Disorders. *J. Neurosurg.* **1959**, *16*, 32–54.
- [9] Sprawls P. Physical principles of medical imaging. Aspen Pub. ISBN:083420309X.
- [10] Chan, V.; Perlas, A. Basics of Ultrasound Imaging. S.N. Narouze (ed.), *Atlas of Ultrasound-Guided Procedures in Interventional Pain Management*, 13, DOI 10.1007/978-1-4419-1681-5_2,
- [11] Curie, P.; Curie, J. *Contractions et dilatations produites par des tensions électriques dans les cristaux hémiedres à faces inclinées. Comptes rendus de l'Académie des Sciences*, **1881**, *93*, 1137-1140.
- [12] Fass, L. Imaging and Cancer: A Review. *Mol. Oncol.* **2008**, *2*, 115-152.
- [13] William, D.; O'Brien, Jr. Ultrasound—biophysics mechanisms. *Prog. Biophys. Mol. Biol.* **2007**, *93*, 212–255.
- [14] Simpson, D. H.; Chin, C. T.; Burns, P. N. Pulse Inversion Doppler: a New Method for Detecting Nonlinear Echoes from Microbubble Contrast Agents. *IEEE Trans Ultrason. Ferroelectr. Freq. Control* **1999**, *46*, 372–382.

Chapter III

[15] Luke, G. P.; Yeager, D.; Emelianov, S. Y. Biomedical Applications of Photoacoustic Imaging with Exogenous Contrast Agents. *Ann. Biomed. Eng.* **2012**, *40*, 422–437.

[16] Li, C.; Wang, L. V. Photoacoustic Tomography and sensing in Biomedicine. *Phys. Med. Biol.* **2009**, *54*, 59–97.

[17] Levi, J. *et al.* Molecular Photoacoustic Imaging of Follicular Thyroid Carcinoma. *Clin. Cancer Res.* **2013**, *19*, 1494–1502.

[18] Li, P. C. *et al.* In vivo Photoacoustic Molecular Imaging with Simultaneous Multiple Selective Targeting Using Antibody-Conjugated Gold Nanorods. *Opt. Express* **2008**, *16*, 18605–18615.

[19] Kruger, R. A.; Lam, R. B.; Reinecke, D. R.; Del Rio, S. P.; Doyle, R. P. Photoacoustic angiography of the breast. *Med. Phys.* **2010**, *37*, 6096.

[20] Ku, G.; Wang, L. V. Deeply penetrating photoacoustic tomography in biological tissues enhanced with an optical contrast agent. *Opt. Lett.* **2005**, *30*, 507–509.

[21] Luo, S.; Zhang, E.; Su, Y.; Cheng, T.; Shi, C. A review of NIR dyes in cancer targeting and imaging. *Biomaterials* **2011**, *32*, 7127–7138.

[22] Sreejith, S.; Joseph, J.; Lin, M.; Menon, N. V.; Borah, P. Near-infrared squaraine dye encapsulated micelles for in vivo fluorescence and photoacoustic bimodal imaging. *ACS Nano* **2015**, *9*, 5695–5704.

[23] Hannah, A.; Luke, G.; Wilson, K.; Homan, K.; Emelianov, S. Indocyanine Green-Loaded Photoacoustic Nanodroplets: Dual Contrast Nanoconstructs for Enhanced Photoacoustic and Ultrasound Imaging. *ACS Nano* **2014**, *8*, 250-259.

[24] Jeon, M.; Song, W.; Huynh, E.; Kim, J.; Kim, J.; Helfield, B. L.; Leung, B. Y. C.; Goertz, D. E.; Zheng, G.; Oh, J.; Lovell, J. F.; Kim, C. Methylene blue microbubbles as a model dual-modality contrast agent for ultrasound and activatable photoacoustic imaging. *J. Biomed. Opt.* **2014**, *19*, 016005.

[25] Huynh, E.; Lovell, J. F.; Helfield, B. L.; Jeon, M.; Kim, C.; Goertz, D. E.; Wilson, B. C.; Zheng, G. Porphyrin Shell Microbubbles with Intrinsic Ultrasound and Photoacoustic Properties. *J. Am. Chem. Soc.* **2012**, *134*, 16464–16467.

Chapter III

- [26] Gramiak, R.; Shah P. Echocardiography of the aortic root. *Invest Radiol.* **1968**, *3*, 356–366.
- [29] de Jong, N.; Bouakaz, A.; Frinking, P. Basic Acoustic Properties of Microbubbles. *Ecocardiography* **2002**, *19*, 229-240.
- [30] K. Kooiman, T. J. A. Kokhuis, T. van Rooij, I. Skachkov, A. Nigg, J. G. Bosch, A. F. W. van der Steen, W. A. van Cappellen, N. de Jong, *Eur. J. Lipid Sci. Technol.* **2014**, *116*, 1217–1227.
- [31] Plesset, M.S. The dynamics of cavitation bubbles. *ASME J. Appl. Mech.* **1949**, *16*, 228–231.
- [32] E. Stride. Physical Principles of Microbubbles for Ultrasound Imaging and Therapy. *Cerebrovas. Dis.* **2009**, *27*, 1– 13.
- [33] Stride, E. P.; Coussios, C. C. Cavitation and contrast: The use of Bubbles in Ultrasound Imaging and Therapy. *P. I. Mech. Eng. H* **2010**, *224*, 171– 191.
- [34] Grishenkov, D.; Kari, L.; Brodin, L-Å.; Brismar, T. B.; Paradossi, G. In vitro contrast-enhanced ultrasound measurements of capillary microcirculation: comparison between polymer-and phospholipid-shelled microbubbles. *Ultrasonics* **2011**, *51*, 40 – 48.
- [35] Butt, H. J.; Graf, K.; Kappl, M. *Wiley: Physics and Chemistry of Interfaces* **2006**, *9*.
- [36] Cavalieri, F.; El Hamassi, A.; Chiessi, E.; Paradossi, G. Stable Polymeric Microballoons as Multifunctional Device for Biomedical Uses: Synthesis and Characterization. *Langmuir* **2005**, *2*, 8758-8764.
- [37] Cavalieri, F.; Finelli, I.; Tortora, M.; Mozetic, P.; Chiessi, E.; Polizio, F.; Brismar, T. B.; Paradossi, G. Polymer Microbubbles As Diagnostic and Therapeutic Gas Delivery Device. *Chem. Mater.* **2008** *20*, 3254-3258.
- [38] Cavalieri, F.; El Hamassi, A.; Chiessi, E.; Paradossi, G.; Villa, R.; Zaffaroni, N. Tethering Functional Ligands onto Shell of Ultrasound Active Polymeric Microbubbles. *Biomacromolecules* **2006**, *7*, 604-611.
- [39] Luke, G.P.; Myers, J.N.; Emelianov, S.Y.; Sokolov, K.V. Sentinel lymph node biopsy revisited: ultrasound-guided photoacoustic detection of micrometastases using molecularly targeted plasmonic nanosensors. *Cancer Research* **2014**, *74*, 5397-5408.

Chapter III

[40] Mallidi, S.; Larson, T.; Tam, J.; Joshi, P.; Karpiouk, A.; Sokolov, K.; Emelianov, S. Multi-wavelength photoacoustic imaging and plasmon resonance coupling of gold nanoparticles for selective detection of cancer. *Nano Lett.* **2009**, *9*, 2825-2831.

[41] Chen, Y. S.; Frey, W.; Kim, S.; Homan, K.; Kruizinga, P.; Sokolov, K.; Emelianov, S. Enhanced Thermal Stability of Silica-Coated Gold Nanorods for Photoacoustic Imaging and Image Guided Therapy. *Opt. Express* **2010**, *18*, 8867-8878.

[42] Lalwani, G.; Cai, X.; Nie, L.; Wang, L. V.; Sitharaman, B. Graphene-based contrast agents for photoacoustic and thermoacoustic tomography. *Photoacoustics* **2013**, *1*, 62-67.

[43] Patel, M. A.; Yang, H.; Chiu, P. L.; Mastrogiovanni, D D. T.; Flach, C. R.; Savaram, K.; Gomez, L.; Hemnarine, A.; Mendelsohn, R.; Garfunkel, E.; Jiang, H.; He, H. Direct Production of Graphene Nanosheets for Near Infrared Photoacoustic Imaging. *ACS Nano* **2013**, *7*, 8147-8157.

[44] Wang, Y. W.; Fu, Y. Y.; Peng, Q.; Guo, S. S.; Liu, G.; Li, J.; Yang, H. H.; Chen, G. N. Dye Enhanced Graphene Oxide for Photothermal Therapy and Photoacoustic Imaging. *J. Mater. Chem. B* **2013**, *1*, 5762-5767.

[45] Moon, H.; Kumar, D.; Kim, H.; Sim, C.; Chang, J. H.; Kim, J. M.; Kim, H.; Lim, D. K. Amplified Photoacoustic Performance and Enhanced Photothermal Stability of Reduced Graphene Oxide Coated Gold Nanorods for Sensitive Photoacoustic Imaging. *ACS Nano* **2015**, *9*, 2711-2719.

[46] Weber, J.; Beard, P. C.; Bohndiek, S. E. Contrast Agents for Molecular Photoacoustic Imaging. *Nat. Methods* **2016**, *13*, 639-650.

[47] Homan, K.; Shah, J.; Gomez, S.; Gensler, H.; Karpiouk, A. Silver nanosystems for photoacoustic imaging and image-guided therapy. *J. Biomed. Opt.* **2010**, *15*, 021316.

[48] Homan, K. A.; Souza, M.; Truby, R.; Luke, G. P.; Green, C.; Vreeland, E.; Emelianov S. Silver Nanoplate Contrast Agents for *In Vivo* Molecular Photoacoustic Imaging. *ACS Nano* **2012**, *6*, 641-650.

[49] Jastrzębska, A. M.; Kurtycz, P.; Olszyna, A. R. Recent Advances in Graphene Family Materials Toxicity Investigations. *J. Nanopart. Res.* **2012**, *14*, 1320-1328.

Chapter III

[50] De La Zerda, Adam *et. al.* Carbon Nanotubes as Photoacoustic Molecular Imaging Agents in Living Mice. *Nat.Nanotechnol.* **2008**, 3, 557-562.

Chapter IV:

Synthesis of Graphene-PVA Microbubbles a Hybrid Contrast Agent for PAI

Chapter IV

1. Introduction:

This chapter describes a new strategy on how pristine graphene sheets can be successfully and stably tethered onto PVA microbubbles surface, and demonstrates its potential as a new hybrid injectable contrast agent for photoacoustic imaging (PAI) by *in vitro* and *in vivo* tests. As far as we know, this is the first study in which pristine graphene has been coupled to microbubbles and for such purpose. The aim behind this work is to combine the appealing features of both materials i.e. PVA microbubbles as biocompatible efficient ultrasound resonators with high chemical versatility, with graphene as strong NIR absorber in a wide spectral range with excellent mechanical properties in order to obtain a novel PA enhancer.

2.1. Materials:

Poly(vinyl-alcohol) (PVA) with a number-average molecular weight, M_n , and weight average molecular weight, M_w , of 30 ± 5 and 70 ± 10 kg/mol, respectively, sodium metaperiodate (NaIO_4), ethylenediamine (EDA), Coomassie Brilliant Blue G (CBB), glycolic acid ethoxylate-4-nonyphenyl ether, synthetic graphite powder with particle size $< 20 \mu\text{m}$, N-(3-Dimethylaminopropyl)-N'-ethyl-carbodiimide hydrochloride (EDC), N-hydroxy-succinimide 98% (NHS), MES 99%, Rhodamine B isothiocyanate (RBITC), dimethylsulfoxide (DMSO), and acetic acid were purchased from Sigma Aldrich, Milan, Italy. Methanol (MeOH) and sodium cyanoborohydrate 95% powder (NaCNBH_3) were purchased from Carlo Erba, Milan, Italy, and Alfa Aesar, respectively. mQ quality water ($18.2 \text{ M}\Omega\cdot\text{cm}$) was produced using a deionization apparatus Pure Lab from USF (Perugia, Italy).

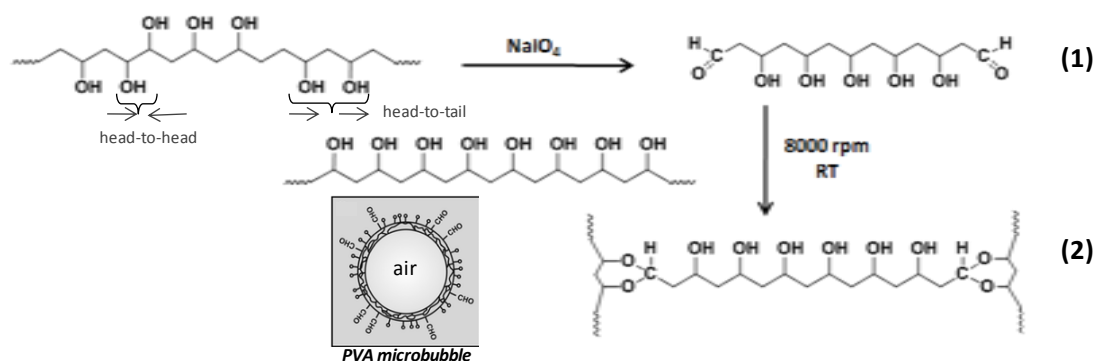
2.2. Methods:

2.2.1. Poly(vinyl-alcohol) microbubbles, PVA MBs, preparation :

PVA MBs were prepared and characterized as described elsewhere ^[1] by crosslinking telechelic PVA chains, at the water/air interface (see [Scheme 1](#)). Typically, 380 mg of NaIO_4 were added to 2% (w/v) PVA aqueous solution to split the polymer into chains of shorter length by the specific oxidation of the head-to-head sequences present in the backbone as structural defects, i.e. about 2 % of the total repeating units, of the polymerization reaction.^[2] The reaction mixture was vigorously stirred at room

Chapter IV

temperature for 2 hours using an Ultra-Turrax at 8000 rpm, generating a fine foam made of PVA shelled microbubbles encapsulating air. The shells are stabilized via the acetalization of the aldehyde chain ends and the hydroxyl groups of the PVA backbone occurring during the foaming. The formed floating MBs were then transferred in separating funnels and washed with mQ water collecting the MBs on top of the aqueous dispersion. During the acetalization not all the aldehydes were converted into crosslinks, some of them were still present at the surface of the shell, exposed to the solvent, and were used for further functionalization.



Scheme 1. Chemical reaction of PVA microbubbles synthesis

2.2.2. Ethylene diamine, EDA, PVA MBs functionalization:

Surface functionalization of PVA MBs shell with EDA was achieved by reductive amination. 10 μmol of EDA were added to 10 ml of an aqueous suspension of PVA MBs at a concentration of 5×10^8 MBs/ml, adjusting the pH to 5 using acetate buffer (0.03 M acetic acid, 0.02 M sodium acetate), followed by the addition of NaCNBH₃ a reducing agent. The suspension was slowly stirred at room temperature with a vortex at 500 rpm for 4 days. Finally functionalized PVA-EDA MBs were intensively washed with mQ water. The primary amino groups of the MBs coupled with EDA were quantified by the Orange II dye method.^[3,4] Typically, a 1mg/ml solution of Orange II sodium salt (pH 3) was prepared in mQ water, the pH was adjusted using HCL 1M. PVA-EDA MBs at a concentration of 10^8 MBs/ml were sonicated for 10 minutes in an ultrasound bath, and then re-dispersed in the acidic solution. Small known amounts of the Orange II dye solution were added successively. At each addition step, microbubbles were incubated for 15 minutes at 40°C, and then centrifuged for 10 minutes at 2500 rpm. The absorbance of the unbound dye in the

Chapter IV

supernatant was measured spectrophotometrically at 485 nm using a double beam JASCO V-630 (Milan, Italy) UV-vis spectrophotometer. Determination was carried out in triplicate.

2.2.3. Graphene Aqueous Dispersion Preparation:

Graphite powder was added to 0.5 mg/ml of glycolic acid ethoxylate-4-nonyphenyl ether aqueous solution at an initial concentration of 20 mg/ml, then exfoliated by ultra-sonication for 90 minutes at 320 W using a tip sonicator (1/2 inch titanium tip); these were the optimized conditions for our study. Vander Waals interactions between the graphene planes were overcome by the shear forces caused by the sonication and the aid of the surfactant to stabilize the exfoliated sheets in water through the interaction between the phenyl moiety of the surfactant with the graphene sp^2 surface.^[5,6] The system was placed in an ice bath during the sonication process to avoid over-heating, and the mixture was agitated, every 30 minutes, at 1500 rpm for 2 minutes to homogenize the non-exfoliated graphite powder throughout the aqueous suspension. The resulting dispersion was centrifuged twice for 30 minutes at 1300 rpm to remove large aggregates. The graphene concentration was estimated by UV spectrophotometry using a double beam JASCO V-630 (Milan, Italy) UV-vis spectrophotometer with a 1 cm quartz cell (Hellma, GE), monitored at 660 nm as reported previously in the literature,^[7] and the sheets size distribution was estimated by dynamic light scattering.

2.2.4. Graphene functionalization of PVA-EDA MBs:

Graphene was conjugated to the PVA-EDA MBs modified shell by EDC/NHS chemistry by activating the carboxylic moiety in the surfactant stabilizer and the $-NH_2$ group of the shell surface. For G/PVA (10% w/w) MBs, an equimolar amount about 1 μ mol of EDC/NHS was added to 10 ml of 0.15 mg/ml graphene/surfactant aqueous suspension to activate the carboxylic acid moiety present in the surfactant, and the pH was fixed to 6.5 with MES buffer. Then, 5 ml of PVA-EDA MBs at a concentration of 3 mg/ml was added. The obtained suspension was kept overnight in the dark at room temperature under stirring. Finally, the graphene functionalized PVA MBs were intensively washed with mQ water. It was observed that the washings were

Chapter IV

completely transparent, in contrast the floating MBs were dark grey colored suggesting that graphene stabilized sheets were homogeneously dispersed and coupled by the aid of the surfactant on the PVA MBs modified shells. MBs were then sonicated for 2 minutes at 50% in a water bath sonicator to disperse the aggregates formed by the stacking interaction between the graphene sheets. The as prepared MBs were freeze-dried and stored in the form of powder for further study. It is worth to note that coverage of the shell surface with graphene can be tuned by varying the amount of MBs in functionalization reaction while maintaining fixed the graphene concentration and vice-versa. MBs with lower/higher graphene amount on the shell were obtained by conserving approximately the previous graphene amount and increasing/decreasing the quantity of MBs put in reaction.

2.2.5. G/PVA RBITC labeled MBs:

MBs labeled with fluorescent RBITC were prepared for size distribution determination using confocal microscopy. Typically, 1 ml of 10^8 MBs/ml of G/PVA was incubated with 10 μ l of RBITC solution (2 mg/ml in DMSO) for 1 hour under slow stirring, then intensively washed with mQ water by several steps centrifugation at 1000 rpm for 5 minutes.

2.2.6. Optical and confocal microscopy characterization:

Observations were performed using an inverted microscope Eclipse model Ti-E (Nikon Instruments, Japan) equipped with a 60 \times /1.4 oil immersion Plan Apo objective, an Ar⁺ green laser (λ_{exc} = 543 nm) (MellesGriot, Carlsbad, CA, USA), and a He-Ne laser (λ_{exc} = 633 nm) (Spectra Physics, Mountain View, CA, USA). The concentration of microbubbles was determined with the aid of bright field microscopy using a Nauber chamber (0.25 \times 0.25 \times 0.1) μ m, then analysis of the micrographs was performed using ImageJ free software.

Chapter IV

2.2.7. Raman spectroscopy characterization:

The Raman study was carried out using a Raman confocal microscope (Horiba Jobin Yvon XploRA), equipped with solid state laser sources at 532 and 785 nm and a 100x objective. The characterization of the graphene aqueous suspension was performed at 532 nm excitation wavelength by evaporating at room temperature few microliters deposited on Si wafer. Also G/PVA MBs were explored at 532 nm. A small amount of freeze-dried MBs powder was deposited on Si wafer and dispersed on the surface by adding a few microliters of water, then left to evaporate at room temperature before the Raman study.

2.2.8. Thermogravimetric analysis (TGA):

TGA measurements of PVA MBs and G/PVA MBs different samples with variable graphene surface densities, prepared by decreasing the initial amount of PVA-EDA MBs, were carried out using TA Q600 instrument. Freeze-dried MBs were placed in platinum pan, and the measurement was performed under nitrogen atmosphere (100 ml/min) from 25 °C to 1000 °C at a heating rate of 10 °C/min.

2.2.9. Differential Scanning calorimetry:

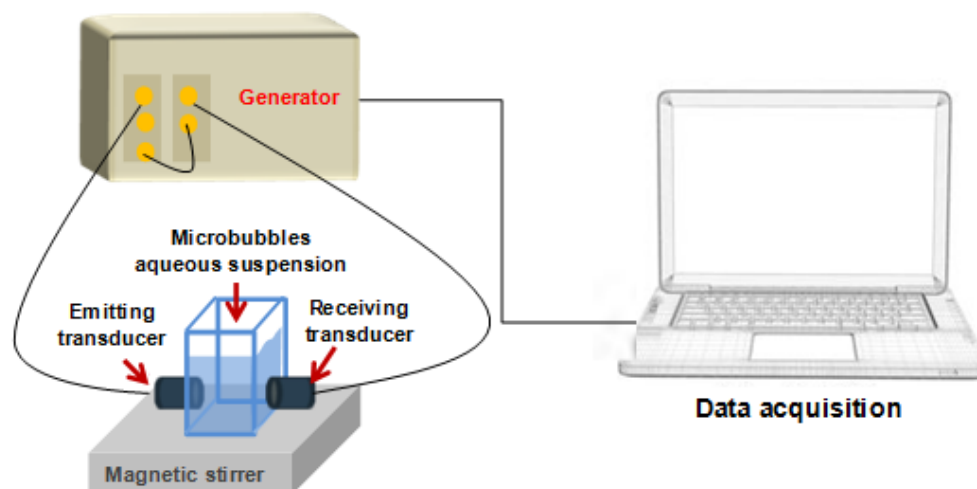
G/PVA MBs with graphene contents 2.5%, 5 % and 10% (w/w) were examined and compared to the plain PVA MBs. Approximately 1 mg of freeze-dried microbubbles powder was placed in an aluminum pan and sealed with holed aluminum lid. The scan was performed from 20°C to 250°C at a heating rate of 10°C/min under a flow of 50 mL/min of Nitrogen using a TA Q2000 differential scanning calorimeter, from TA instruments Milano, Italy.

2.2.10. Field emission scanning electron microscopy (FESEM):

G/PVA MBs aqueous suspensions with graphene shell density percentage of 2%, 5%, and 10% (w/w) (see table 1 for details in the SI) were observed. Control experiment was carried out with plain PVA MBs.

Chapter IV

2.2.11. Ultrasound properties measurements:



Scheme 2. Overview of the experimental set-up for acoustic attenuation measurements

[Scheme 2](#) represents the experimental set-up used for the ultrasound transmission experiment through G/PVA MBs in water medium, in order to determine the acoustic attenuation parameters of the considered microbubbles. Glass cell (2x2x4 cm), featuring two opening opposite sides separated by a distance of 2 cm allowing the contact with emitting and receiving transducers, was filled with 17 ml of mQ water.

The measurements were carried out using flat 10 MHz transducers (Olympus V311) for both emitter and receiver, and a waveform generator to produce consecutive sinusoidal burst of ultrasonic signals at frequencies ranging from 0.5 to 20 MHz with a step of 0.25 MHz. At each frequency, the burst signal was given an input voltage of 6 V, generating pressure levels below 62 kPa. The received signals were processed by comparison with the signals from the mQ water medium taken as a reference.^[8] The amplitude fundamental of the water medium reference was optimized to 0.35 V, and then known volumes of MBs were added up to a final concentration of about 3×10^6 MBs/ml. All steps were controlled by *LabView* software.

2.2.12. In vitro photoacoustic imaging:

The *in vitro* photoacoustic study of the graphene functionalized PVA microbubbles was monitored using VEVO® LAZR instrument from Visualsonics (Amsterdam, NL)

Chapter IV

equipped with an integrated fiber-optic linear array LZ250 transducer with an axial resolution of 75 μm and operating at a frequency of 21 MHz

G/PVA MBs at an initial concentration of 10^8 MBs/ml were injected into a capillary tube immersed within a mimicking tissue phantom (see Figure 1). For control experiments, another tube was injected only with saline NaCl solution. All PA measurements were performed at a gain of 45 dB, and at a laser excitation of 750 nm, which has revealed as the optimal wavelength for G/PVA MBs. The PA enhancement was studied as a function of MBs concentration and compared to the phantom tissue.

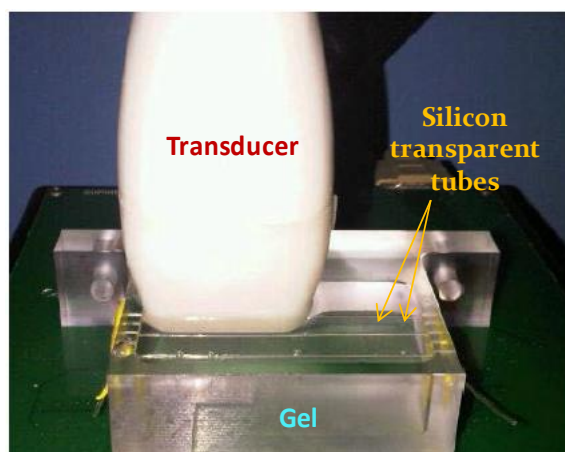


Figure 1. In vitro phantom overview

2.2.13. *In vivo* photoacoustic imaging

In vivo PA experiments were carried out using the same equipment as for the *in vitro* study and was performed at a gain of 50 dB on normal mouse by injecting 30 μl of G/PVA MBs (5% w/w, 3×10^7 MBs/ml) into hind limb muscle.

3. Results and Discussion

3.1. Primary amine groups quantification on modified PVA-EDA MBs

The estimation of the amount of available functional amine groups in PVA-EDA shell is required in order to optimize the tethering of graphene to the MBs surface through the carboxylic moiety of the surfactant. The absorbance of the free Orange

Chapter IV

It is exclusively related to the number of bound dye moieties to form the complex PVA-EDA-Orange II, which allows knowledge of available primary amines. The amount of amino groups per single PVA-EDA microbubble was estimated as equal to $(0.7 \pm 0.03) \times 10^{-15}$ mol/MB (see Figure 2).

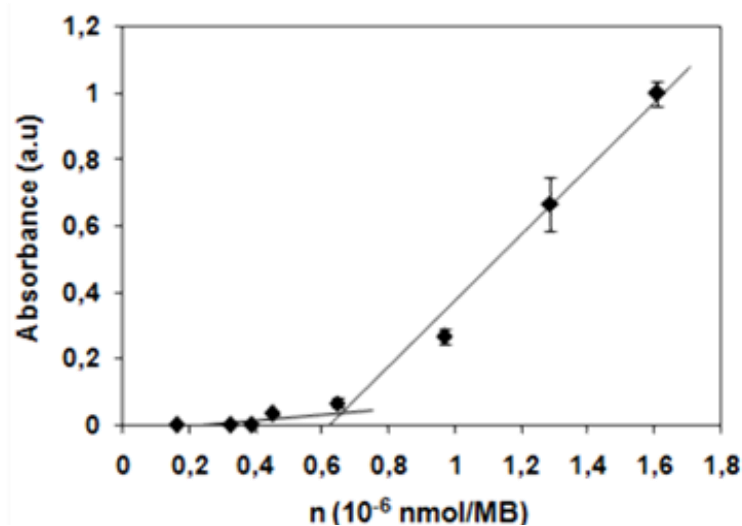


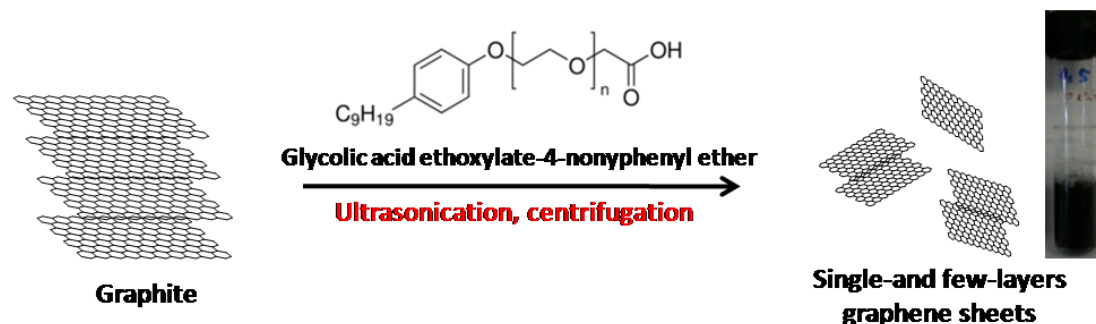
Figure 2. Titration of the primary amine groups attached to PVA microbubbles: Orange II supernatant absorbance at 485 nm versus added amount of Orange II/MB

3.2. Characterization of graphene dispersion and G/PVA hybrid MBs

During ultrasonication in an aqueous medium, the cohesive forces stabilizing graphite are broken by the shear energy. The hydrophobic nature of graphene makes the aqueous dispersion colloidally unstable. However, the action of a stabilizing agent such as a surfactant interacting via π - π stacking with the exfoliated graphene sheets avoids the graphene sheets reaggregation. Moreover, this process is effective for the spontaneous purification of the graphene material from graphite residues. These sheets are a collection of monolayer and few layers of graphene (up to four or five planar layers), with a distribution that depends on the exfoliation method. The overall byproduct of the exfoliation process is usually indicated as pristine graphene since no modification of the graphene structure occurred. The ionic and nonionic nature of the surfactant does not play a significant role.^[9] For example, IGEPAL® a commercial surfactant is considered a good graphene dispersant.^[10] We took advantage of this finding using a similar molecule, terminated

Chapter IV

with a carboxylic acid moiety at the end of a PEG hydrophilic tail of the monomer (see [Scheme 3](#)). This approach enables subsequent functionalization of the stabilized graphene sheets and the PEG moiety should, in principle, limit the biological impact of the overall systems when injected for in vivo experiments.

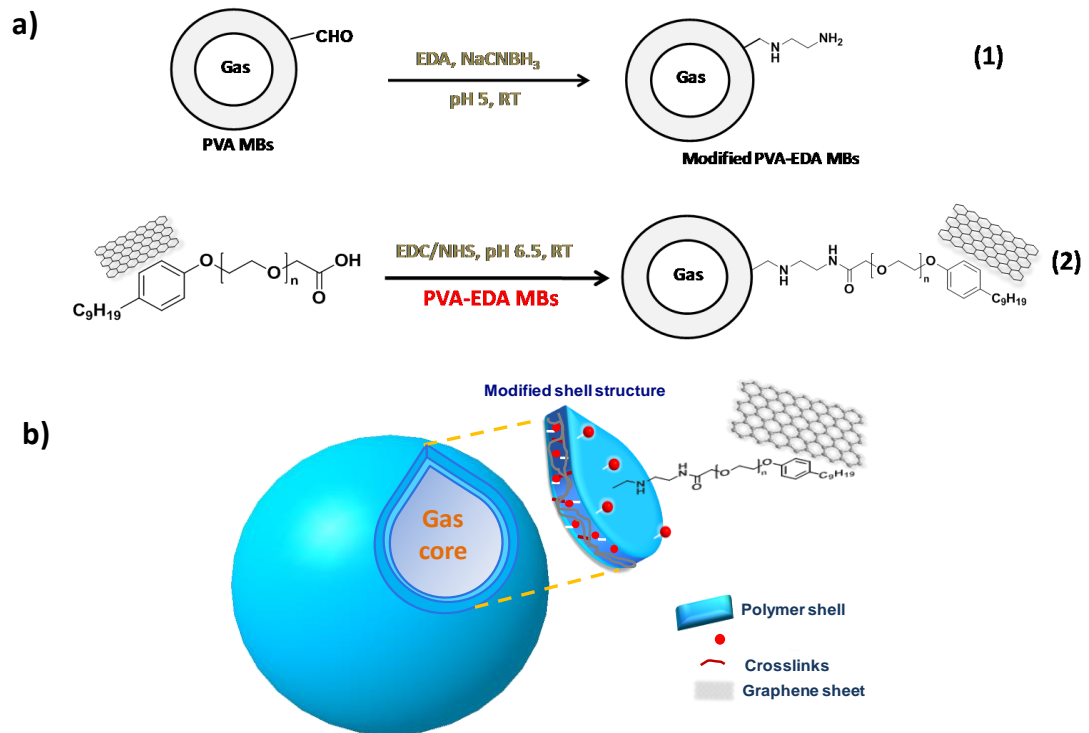


Scheme 3. Graphene surfactant assisted ultra-sonication

Stable graphene/surfactant aqueous suspensions were achieved up to a concentration of 0.25 mg/ml estimated by UV spectrophotometry.^[13] The almost independent absorbance to the wavelength exhibited from the visible to the Near infrared (NIR) region (see [Figure 3a](#)) is characteristic of pristine graphene, this absorbance feature in the NIR domain originates primarily from interband transitions.^[11] The suspension was composed by sheets of few hundreds of nm as determined by DLS (see [Figure 3b](#)).

Tethering of graphene to PVA MBs was based on a two-steps reaction: (i) aldehyde groups on the MBs shell surface were coupled with ethylene diamine (EDA) by reductive amination, (ii) the carboxylic moiety of the surfactant stabilizing graphene was conjugated to the $-NH_2$ group of PVA-EDA functionalized MBs via EDC/NHS chemistry (see [Scheme 4](#)). The obtained MBs are grey-black colored according to the coverage of the shell surface with graphene ([Figure 3c](#)).

Chapter IV



Scheme 4. a) PVA MBs modification and graphene functionalization, b) G/PVA MBS detailed structure.

Chapter IV

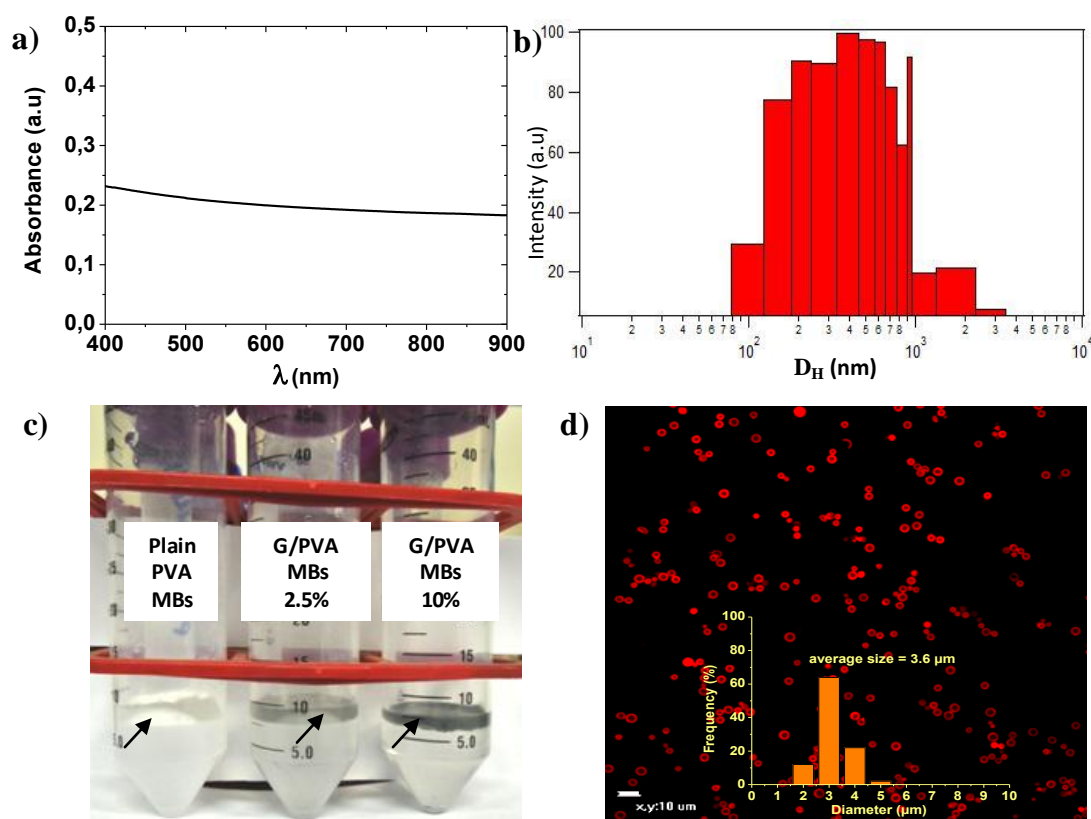


Figure 3. a) UV-visible-NIR absorbance spectrum of suspension, b) graphene sheets size distribution by DLS c) PVA and G/PVA MBs aqueous suspensions; the arrows show microbubbles floating at the air-water interface, d) Confocal laser microscopy of RBITC labeled G/PVA MBs ($\times 60$).

G/PVA MBs, with an average diameter of $(3.6 \pm 0.8 \mu\text{m})$, were well dispersed (see Figure 3d) when freshly prepared, but tend to aggregate with the aging within few weeks probably due to the π - π interaction between the graphene material. Such hurdle can be overtaken by storing them as freeze-dried powder to disperse before the use since G/PVA MBs maintain the property to reconstitute from the freeze-dried state as already observed for the plain PVA MBs.^[12] However, a rapid floating process respect to the plain PVA MBs is observed. Such a phenomenon was reported by Kim *et al.* for an aqueous suspension of GO sheets trapped by N_2 gas bubbles, used as carriers, and collected on the air/water surface by flotation.^[13] More than two decades ago, a similar practice was described to concentrate graphite at the air-water interface as it can be readily attached to air bubbles.^[14] In our case, this effect can be explained as the graphene sheets play the role of an accelerating carrier for the gas filled PVA microbubbles. This can be attributed to the hydrophobic nature of

Chapter IV

graphene that once tethered to the MBs shell, it repels the water medium increasing the floating tendency of the MBs to float at the water/air interface.

3.3. Raman spectroscopy characterization of graphene dispersion and of G/PVA

MBs:

Raman spectroscopy is known as the fingerprint tool to characterize the quality of graphene systems. The typical feature of graphene are the first order and the second order G and 2D bands at 1580 cm^{-1} and 2680 cm^{-1} , respectively, where the intensity ratio I_{2D}/I_G and the shape of the 2D resonance is informative about the number of layers. However, the D band at 1350 cm^{-1} is related to the presence of disorder in the structure, thus the intensity ratio I_D/I_G allows for a quantification of defects.^[15,16] Confocal Raman mapping at 532 nm laser excitation wavelength of the graphene/surfactant dispersion revealed that the suspension mainly contained a mixture of single- and few-layers (up to 4 layers) graphene sheets (see Figure 4).

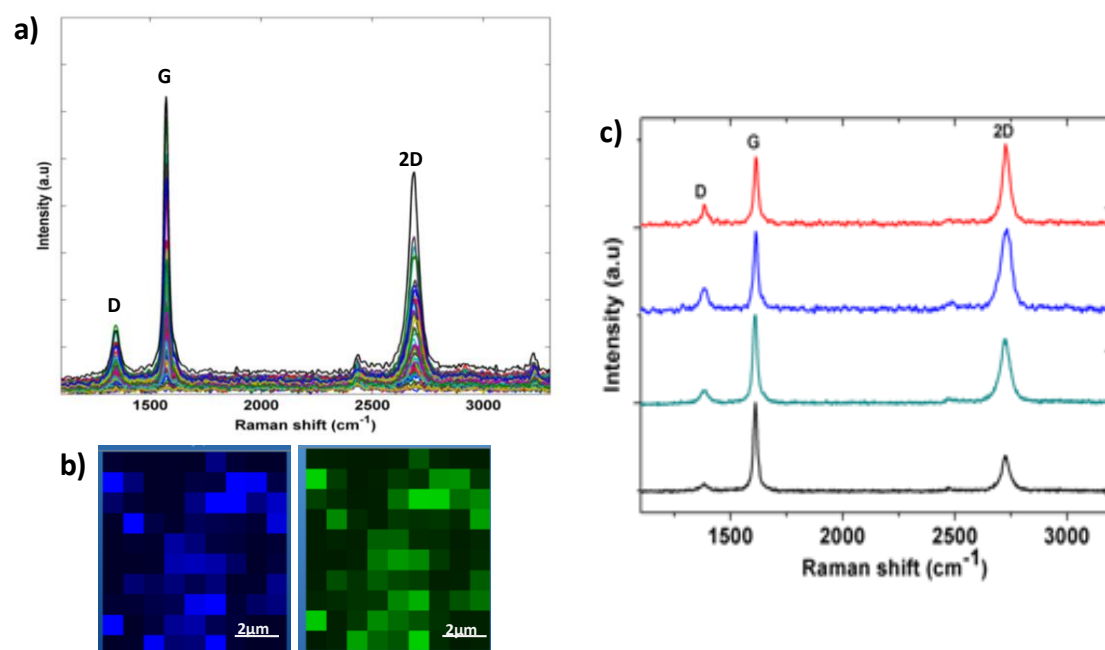


Figure 4. a) Graphene dispersion confocal Raman mapping spectra at 532 nm laser excitation wavelength; b) G (blue) and 2D (green) Raman bands maps; c) Raman spectra, collected from the mapping, of the different existing forms of graphene (single and few-layers) in the surfactant aqueous dispersion.

Chapter IV

Figure 5a shows a comparison between Raman spectra of the starting graphite and obtained single-layer graphene. The presence of a D band with very low intensity compared to the G band indicates a limited number of defects originated from the starting graphite before its exfoliation. Moreover, this exfoliation method leaves nearly unchanged the pristine graphene structure.

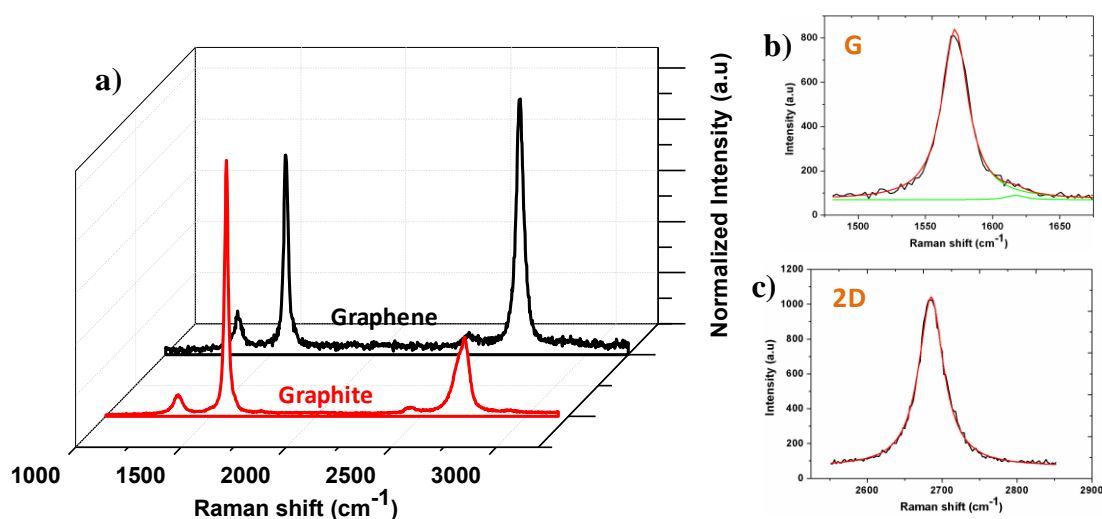


Figure 5. a) Raman spectra comparison between starting graphite powder (red) and single layer graphene present in the surfactant aqueous suspension (black) at 532 nm excitation; single-layer graphene: b) G Raman band (black line) and the fit (red line) obtained by two Lorentzians (G and D' components) (green lines), c) 2D Raman band (black line) with one Lorentzian fit (red line).

The successful graphene tethering to the G/PVA MBs was studied by Raman mapping at 532 nm in order to assess the quality and the spatial distribution of graphene on the MB shells after functionalization. All spectra were collected at a laser excitation wavelength of 532 nm. For comparison, a Raman spectrum of plain PVA MBs, i.e. without graphene, is illustrated in Figure 6a. The resonance at about 3000 cm^{-1} is attributed to the CH stretching modes of the polymeric shell of the microbubble. It should be mentioned that it was not possible to obtain a clear Raman spectrum in the case of plain microbubbles, contrarily to G/PVA MBs, because of autofluorescence which is a common issue in the Raman spectroscopy analysis when dealing with polymeric matrixes. A Raman mapping collected on a single G/PVA microbubble is shown in Figure 6b. It is worth to notice that despite the complexity of the polymeric matrix, graphene typical spectral features, i.e. G and 2D

Chapter IV

bands at 1576 cm^{-1} and 2684 cm^{-1} , respectively, were clearly evidenced (Figure 6b). The presence of graphene increases significantly the enhancement of the resonances corresponding to the CH stretching of the polymeric moiety (see Figure 6c), which is in accordance with the findings reported in the literature about the graphene effect on the surface-enhanced Raman scattering (SERS).^[17,18]

Analysis of the Raman mapping bands intensities (Figure 6c) shows an almost equivalent, or even higher, intensity of the 2D band with respect to the G band. This result suggests that tethering graphene to PVA/EDA modified surface does not influence its structure and that the MBs are functionalized with single- and few-layered graphene sheets which are homogeneously distributed over all the PVA MBs shells (see Figure 6e). Raman signals interfering with G and D bands, respectively at around 1580 cm^{-1} and 1380 cm^{-1} , are attributed to the phenyl moiety of the surfactant scaffold, which couples graphene to PVA MBs surface, and to the CH_3 bending modes,^[19] respectively. The resonances, present in the $1200\text{-}1300\text{ cm}^{-1}$ range, are attributed the vibrational modes of C-C of the polymer chains of the shell.

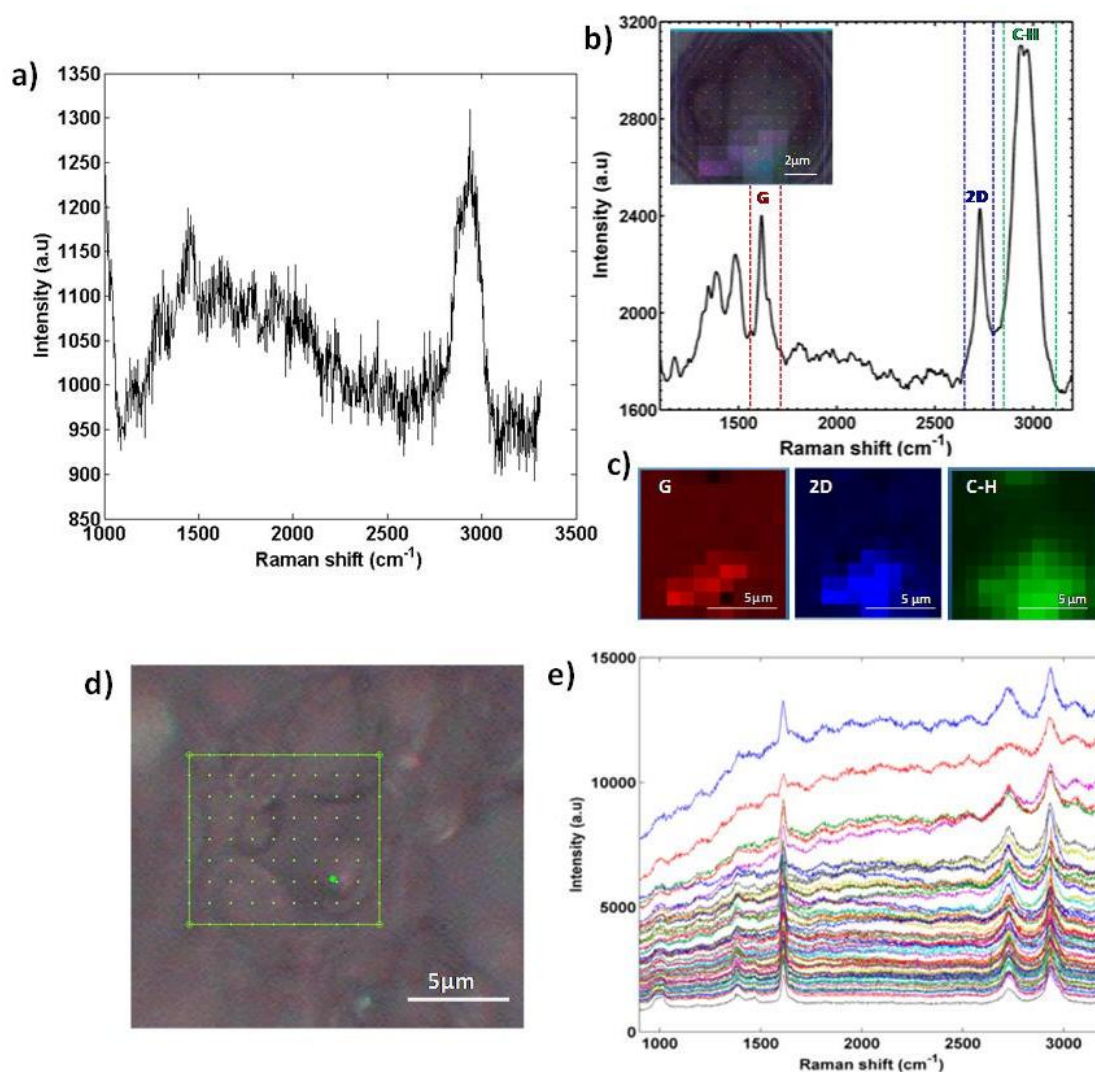


Figure 6. a) Raman spectrum of plain PVA microbubble; b) G/PVA Raman spectrum obtained by confocal Raman mapping on one single G/PVA microbubble, inset: Raman microscopy of the mapped G/PVA microbubble (x100); c) Raman mapping of bands intensities of G/PVA MB; d) Raman mapping microscopy on several G/PVA MBs (x100); e) Raman spectra recorded from the mapping of several G/PVA MBs. All spectra were recorded at an excitation wavelength of 532nm.

3. 4. Thermogravimetric analysis of PVA and G/PVA MBs:

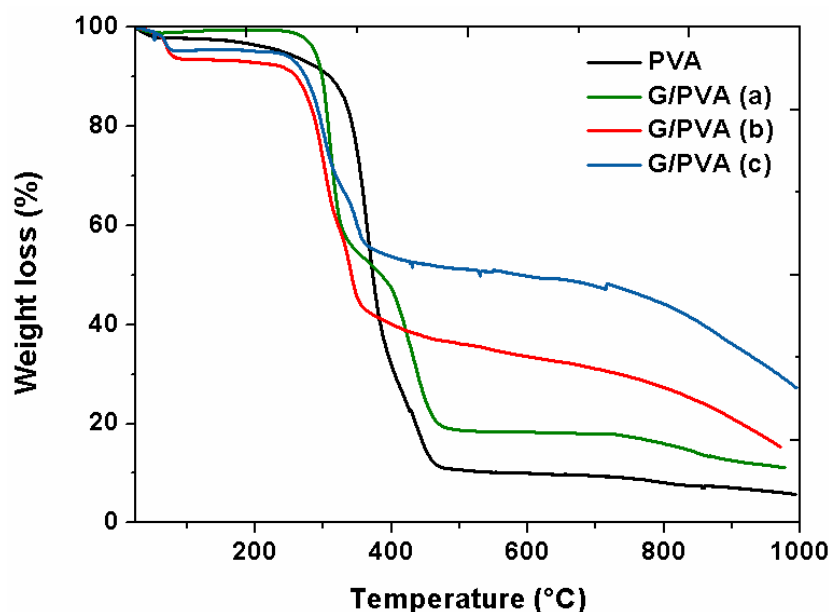


Figure 7. Thermogravimetric analysis PVA and G/PVA microbubbles under Nitrogen flow

The amount of graphene tethered on the PVA shells has been determined by thermogravimetric analysis. [Figure 7](#) shows the decomposition thermograms of G/PVA MBs with different graphene content in comparison with plain PVA MBs up to 1000 °C. G/PVA MBs yielded a higher residual weight respect to naked PVA MBs, proportional to the graphene shell initial feed ratio. The weight loss differences imply the presence of non decomposed graphene sheets and suggest that a total amount of about 28% of graphene respect to PVA can be achieved. The TGA results are in agreement with the estimated graphene from UV absorbance at 660 nm ([Table1](#)). However, at high coverage densities uncontrollable MBs aggregates are formed, which is the reason why for our study we limited the graphene contents to 10 % (w/w) in order to have a balanced assembly ratio between PVA MBs and graphene, thus allowing optimal use of both materials as an injectable device for PAI purposes.

Chapter IV

Table 1. Graphene shell density estimation of G/PVA MBs from UV spectrophotometry

Sample	$m_{\text{(PVA MBs)}} \text{ (mg)}$	$m_{\text{(Graphene)}} \text{ (mg)}$ _UV	% _{graphene/MBs} (w/w)_UV	% _{graphene/MBs} (w/w)_TGA
G/PVA (a)	49	1.4	3	5
G/PVA (b)	12	1.3	11	16
G/PVA (c)	6	1.3	22	28

3.5. Differential Scanning Calorimetry:

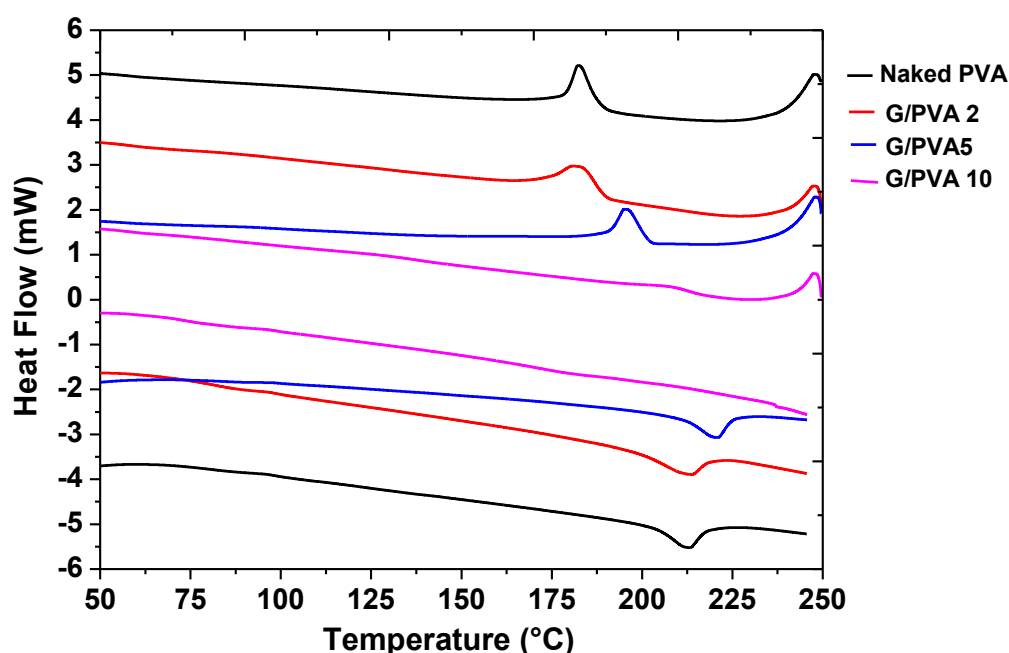


Figure 8. DSC thermograms of PVA and G/PVA microbubbles under 50ml/min Nitrogen flow

Differential scanning calorimetry analysis were performed to evaluate the effect of the tethering of graphene, with different contents i.e. 2.5 %, 5% and 10% (w/w), on the crystallinity of the PVA microbubbles shells. Thermograms of PVA and G/PVA MBs are shown in Figure 8. An increase in both melting and crystallization temperatures is observed as the graphene content increases to 5% (w/w), see also details in Table 1, which is mainly due to an enhancement of the thermal stability induced by the presence of graphene. However, for G/PVA MBs with a graphene content of 10% (w/w) no endothermic and exothermic peaks were exhibited, which reveals a major decrease in the PVA MBs shell crystallinity. In fact, the degree of

Chapter IV

crystallinity for the plain PVA MBs refers to the physical cross-links within the polymeric shell network which are typical for the semi-crystalline nature of PVA (ref), whereas the non crystalline domains refer to the chemical cross-links formed between the aldehyde and hydroxyl groups during the microbubbles synthesis. Therefore, it was found that a chemical modification of the plain PVA MBs surface results in a decrease of the shell crystallinity as the number of physical cross-links is reduced.^[20]

Table 2. G/PVA microbubbles DSC Analysis

Sample	Graphene content (%) (w/w)	T_c (° C)	ΔH_c (J/g)	T_m (° C)	ΔH_m (J/g)
Naked PVA	0	182.86	43.10	213.11	34.96
G/PVA 2	2.5	182.92	45.34	213.25	30.99
G/PVA 5	5	195.76	36.49	220.88	34.29
G/PVA 10	10	--	--	--	--

3.6. Field emission scanning electron microscopy:

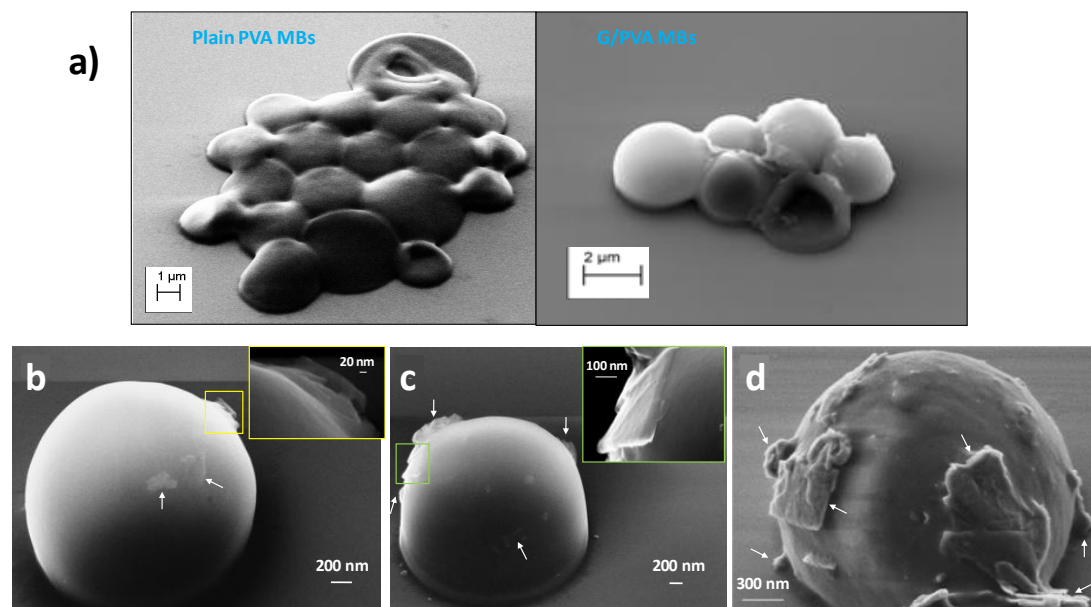


Figure 9. FESEM images of a) Plain PVA MBs versus G/PVA MBs b) G/PVA 2% (w/w), c) G/PVA 5% (w/w), and d) G/PVA 10% (w/w). Arrows show graphene flakes on the MBs shell surface. Green selected zones are magnified in the inset.

The morphology of G/PVA MBs as compared to the plain PVA MBs was analyzed by FESEM microscopy. The micrographs presented in Figure 9 reveal a very smooth,

Chapter IV

well defined shell with a spherical shape, on which are clearly few-layered (3 to 4) graphene sheets. The G/PVA shell aspect is conserved with respect to the plain PVA MBs that seem more collapsed (see [Figure 9a](#)). The graphene sheets on the hybrid microbubbles could be distinguished by taking as a marker the lateral edge contrast produced,^[21] however thinner layers like single ones are hardly distinguishable on the PVA MB surface due to the lower contrast. A higher coverage of the shell surface with the graphene sheets is obtained when increasing the graphene content from 2.5% to 10% (w/w) (see [Figure 9b-d](#)). The graphene sheets anchored to the microbubbles surface can be either folded or crumpled (see [Figure 10](#)).

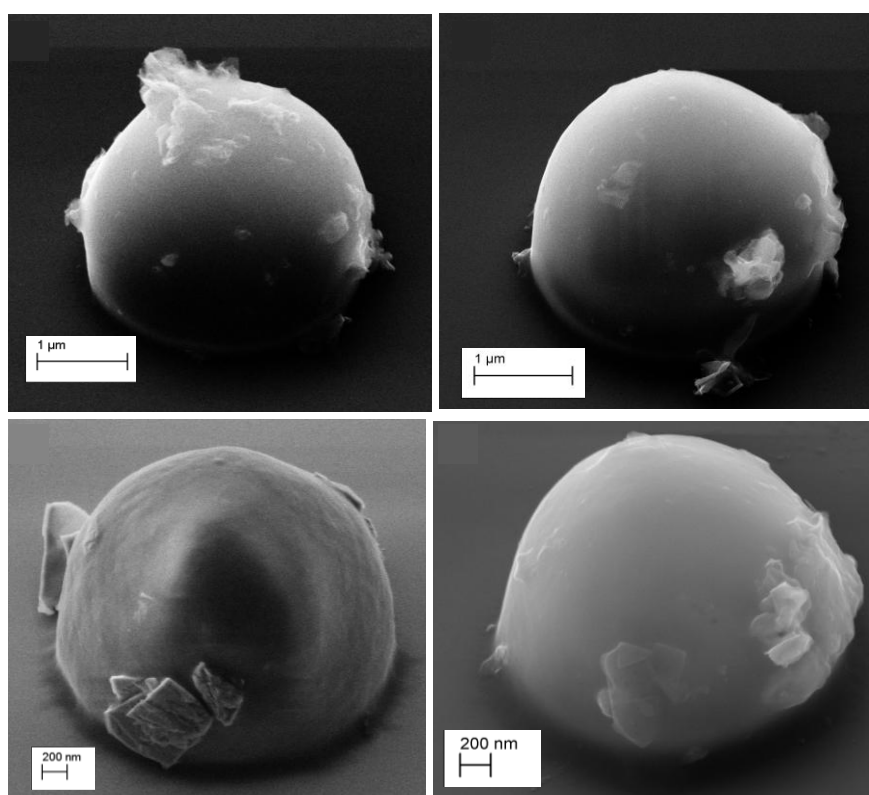


Figure 10. G/PVA MBs showing crumpled or folded graphene sheets on their surfaces.

The size determination by the FESEM images presented herein confirm the results obtained by confocal microscopy and DLS showing a MB size of about 3 μm and graphene sheets in the order of 300 nm. The size of microbubbles should be compatible with intravenous injection. The dimensions of the graphene sheets and functionalized group as well as their thickness are key parameters for performance in biomedical applications and to determine the fate after injection into a living body.^[22]

Chapter IV

3.7. Ultrasound properties of G/PVA MBs:

Ultrasonic attenuation is an important parameter required for determining the acoustic properties of a material. [Figure 11](#) illustrates the dependence of the acoustic attenuation coefficient of G/PVA MBs from frequency in the range 1 – 20 MHz. For all tested MBs concentration, the spectra display a broad maximum of attenuation at about 10 MHz, whose intensity depends on the MBs concentration.

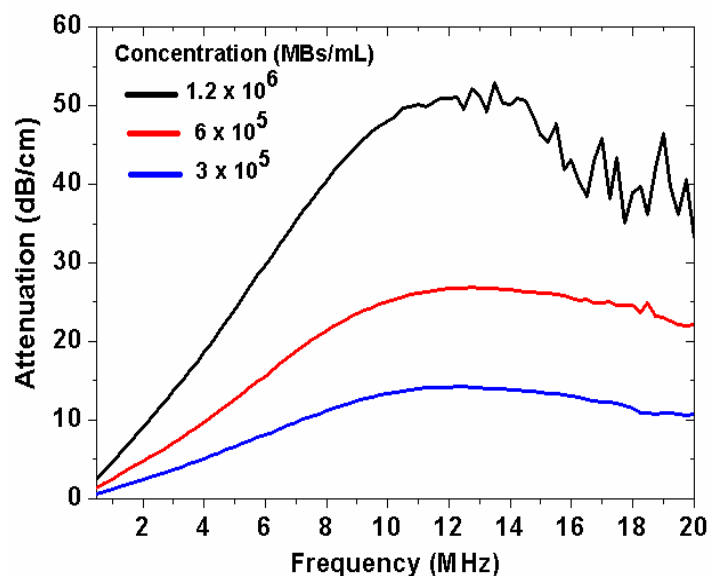


Figure 11. Acoustic attenuation of G/PVA microbubbles as a function of frequency

The acoustic behavior of G/PVA MBs does not change with respect to the plain PVA MBs, indicating that the tethering of graphene to the microbubbles shell does not affect the original echogenic properties of the MBs (see [Figure 12a](#)). Moreover [Figure 12b](#) shows that the G/PVA MBs acoustic performance is conserved after reconstitution from a freeze-dried powder state. Up to now few studies have investigated the acoustic properties of graphene, where it was assumed that ultrasonic waves exist in excess of THz frequencies in graphene.^[23] However, Chivikula *et al.* have demonstrated that surface acoustic waves in graphene may occur at lower frequencies (MHz) as a response to an optical irradiation, which results from the conversion of the energy of the optical power absorbed by the graphene flake to the heating of the sample.^[24]

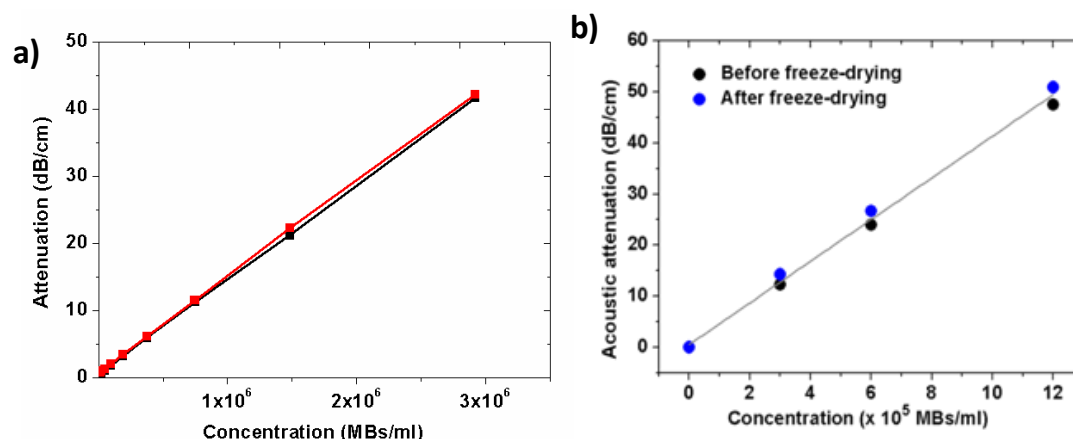


Figure 12. a) Acoustic attenuation vs concentration comparison between PVA MBs (black line) and G/PVA MBs (red line); b) Acoustic attenuation of G/PVA MBs before and after freeze-drying. Attenuation values being measured at 11 MHz.

3.8. Photoacoustic behavior of pristine graphene

Priorly, to confirm our hypothesis regarding coupling graphene to the PVA MBs as a hybrid photoacoustic contrast agent, the efficiency of graphene by itself for PAI when dispersed in the surfactant aqueous solution, was investigated both *in vitro*, using the phantom described in section 2.2.12, and *in vivo*. As shown in Figure 13, graphene exhibits a strong PA response which depends on the concentration in the spectral range from 680 nm to 850 nm.

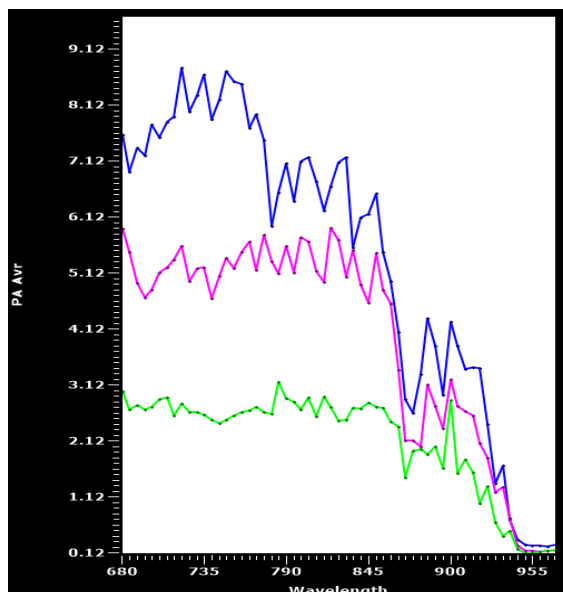


Figure 13. In vitro PA measurements of graphene/surfactant aqueous dispersion at different concentrations : 150 µg/ml (bleu), 50 µg/ml (purple) and 15 µg/ml (green). A 30 dB gain was used.

Moreover, *in vivo* experiments carried out on a bulb male mouse bearing a subcutaneous tumor have shown a strong PA signal in the selected ROI after the injection of 200 µL of the graphene surfactant aqueous suspension at a concentration of 0.15 mg/ml (see Figure 14). The PA signal reached its maximal amplitude after 16 min from injection, being almost 3 fold higher than the original background signal, but then decreases over the time (see Figure 14 and Table 3). At the tested dose no anomalies were observed on the tested mouse.

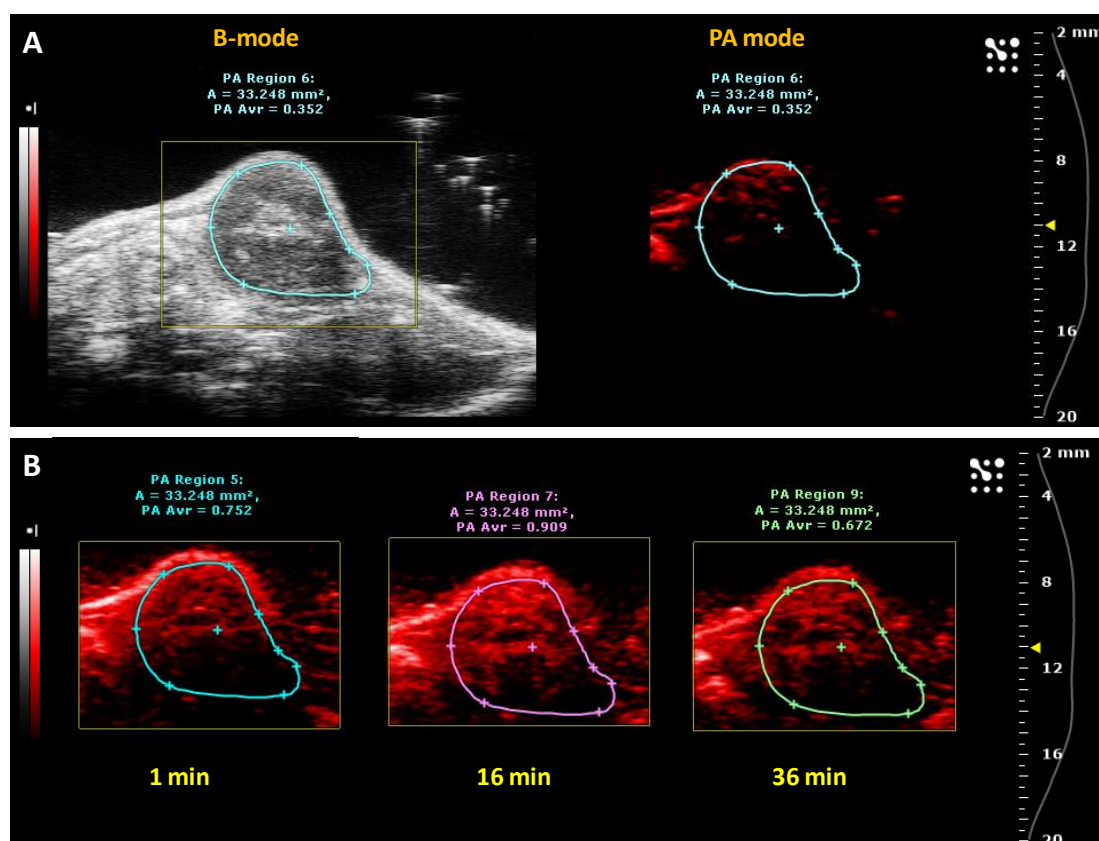


Figure 14. In vivo PAI of graphene/surfactant aqueous suspension injected in mouse bearing tumor monitored at 680 nm and 40 dB gain: (A) Pre-injection and (B) post-injection PA images.

Table 3. PA intensities in the selected ROI over the time after graphene injection

Post-injection time (min)	PA avr (a.u)
0	0.352
1	0.752
16	0.909
36	0.672

3.9. In vitro photoacoustic imaging of G/PVA MBs:

The construction of PA image is based on the following steps: upon NIR pulsed laser illumination of an optical NIR absorber; the absorbed energy is converted to heat leading to the generation of pressure waves which can finally be detected by ultrasound to form the image.^[25-27] Contrarily to fluorophores and Au-nanoparticles

Chapter IV

based contrast agents investigated for PAI, as well as the endogenous cellular tissues, graphene with its strong absorption extending from the visible to the NIR region can provide an excellent optical confinement.^[28,29]

Representative *in vitro* phantom PA images of G/PVA MBs (5% w/w) are shown in Figure 15. Sample concentration of 10^8 MBs/ml exhibited strong PA enhancement respect to the tissue mimicking phantom quantified as about 10 times higher in a.u. Furthermore, PA enhancement depends on the concentration of G/PVA MBs, the detection limit was determined as equal to 10^6 MBs/ml, for which only PA enhancement at the boarder of the ROI was observed and clearly identified from the control saline water and the rest of the tissue. Moreover, MBs exhibit as well good US enhancement in the non-linear mode (see Figure 16).

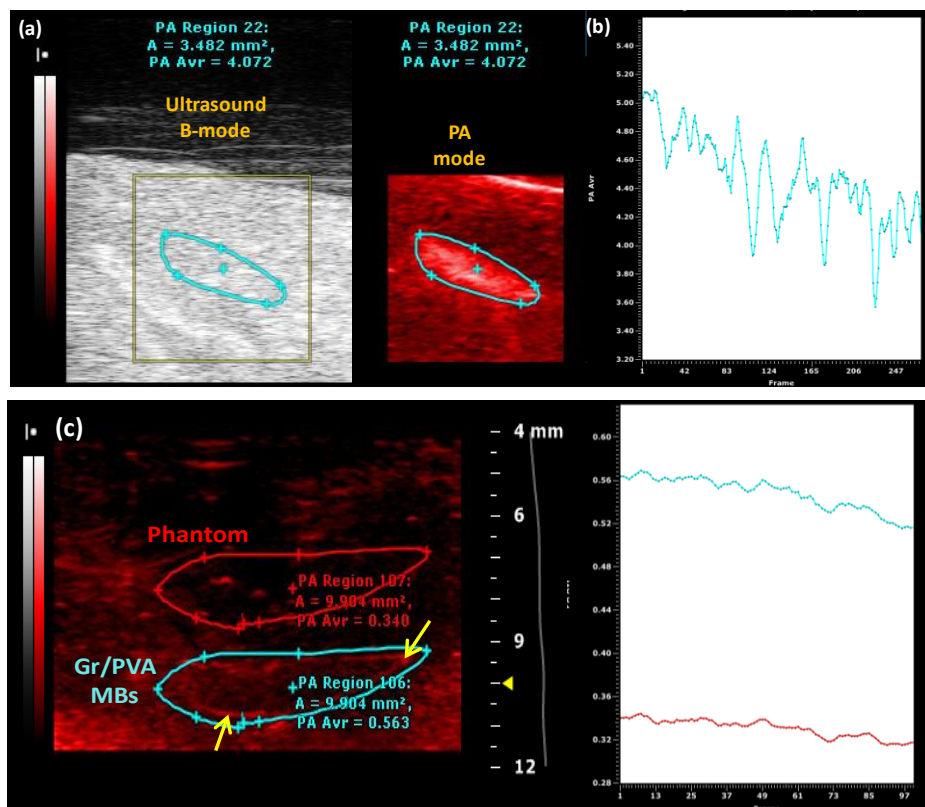


Figure 15. a) *In vitro* PA enhancement image of G/PVA MBs (10^8 MBs/ml), b) PA intensity versus time, c) *In vitro* PA detection limit image of G/PVA MBs (10^6 /ml) Vs Phantom tissue: The yellow arrows show the accumulation of MBs on the boarder side of the injection tube.

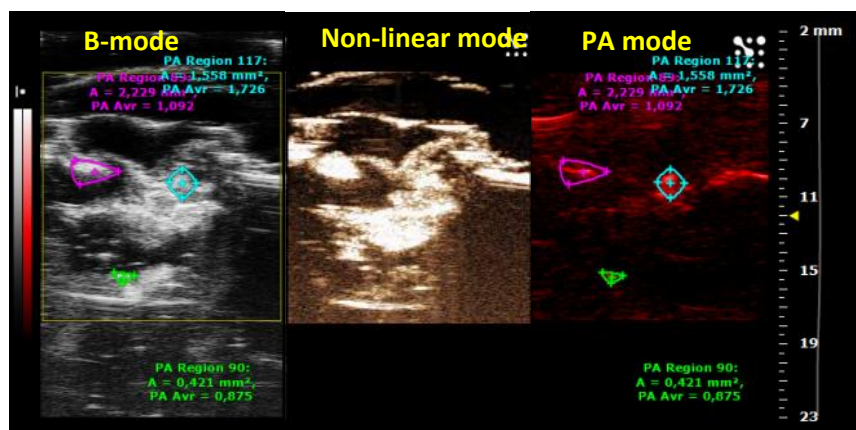


Figure 16. *In vitro* phantom non linear-US enhancement of (10^7 /ml) G/PVA MBs (5%w/w).

G/PVA MBs, as illustrated in Figure 17a, exhibit a strong and wide increase in the PA intensity extending from 680 to 850 nm with respect to the saline water control. The G/PVA MBs (graphene content 5 % w/w) show better PA enhancement than MBs with the lowest content, i.e. 2.5 % w/w, quantified as about 17 times higher as compared to the control (see details in Table 4). However, G/PVA MBs (graphene content 5% w/w) also shows better PA enhancement with respect to the highest graphene content, i.e. 10% w/w (see Figure 17b). These *in vitro* results suggested selecting G/PVA MBs (graphene content 5% w/w) for the subsequent *in vivo* studies. It is also worth to note that the PA spectrum of the G/PVA MBs offers an active window for its PA response which does not interfere with blood components such as hemoglobin (see Figure 17c).

Table 4. Description of G/PVA MBs used for PAI test

Graphene/PVA content (w/w)	2.5 %	5 %	Control (water)
Microbubbles concentration (MBs/mL)	10^8	3×10^7	0
Graphene concentration ($\mu\text{g/mL}$)	26	16	0
PA average (a.u)	1.4	2.9	0.17

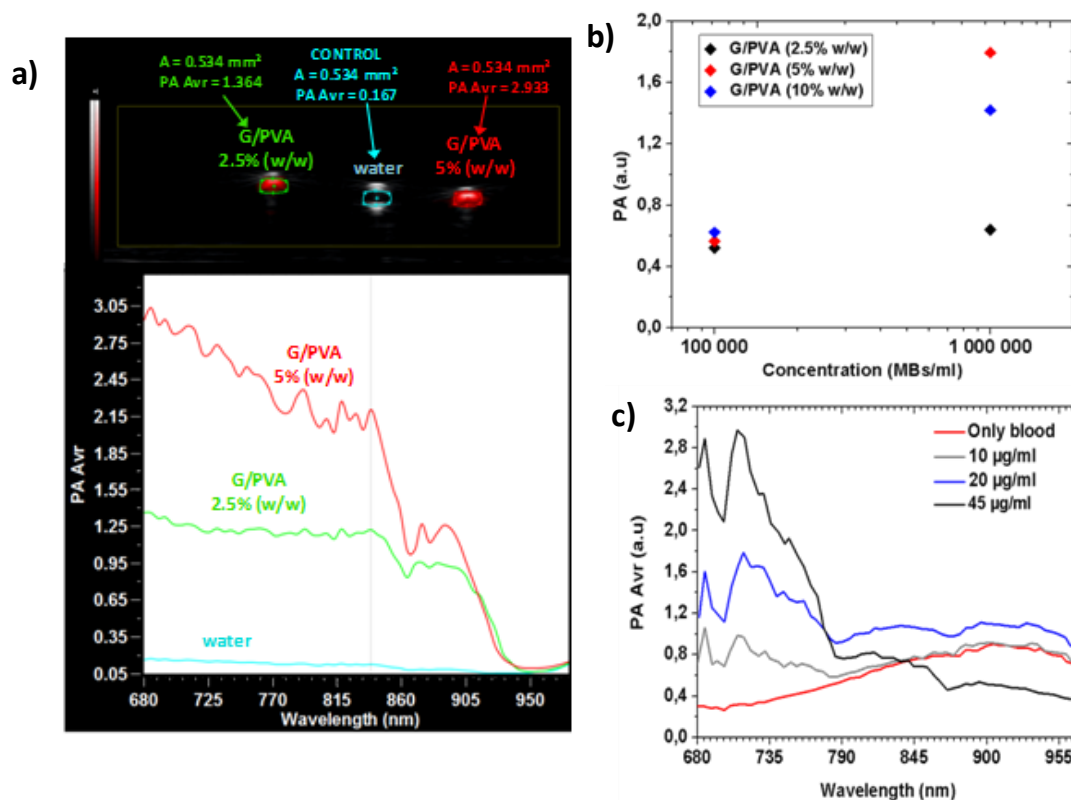


Figure 17. a) *In vitro* PA enhancement spectra of G/PVA MBs (2.5% w/w) (green) and G/PVA (5% w/w) (red) versus water (blue) in phantom, inset: corresponding PA signals image; b) *In vitro* PA response comparison between G/PVA 2.5%, 5%, and 10% (w/w); c) *In vitro* PA spectra of G/PVA MBs (5% w/w) in blood (gain 40 dB).

3.10. *In vivo* photoacoustic imaging of G/PVA MBs

Most studies highlighting graphene as PA contrast agent have focused on the use of GO and rGO combined with metallic nanoparticles as NIR absorbing molecules.^[30-32] Graphene doses per mouse discussed in the literature leading to a significant PA enhancement without toxicity were up to 400 µg of graphene oxide, which is considered within the safety dose range that could extend to 50mg/Kg body weight.^[32-36] To the best of our knowledge, pristine graphene has not been used for *in vivo* PA imaging. In this work, a preliminary real time *in vivo* PAI study using pristine graphene hybrid device shows the PA signal enhancement as result of the injection of 30 µl G/PVA (3×10^7 MBs/ml, graphene content 5% w/w) into wild mouse hind limb muscle. The total amount of pristine graphene loaded on the PVA MBs injected is estimated to be less than 4 µg, and the concentration in MBs after the injection is approximately as equal to the detection limit determined by the previous

Chapter IV

in vitro studies. Despite this very low dose compared to the previously reported administrated doses in the literature investigating PAI, a good enhancement of PA signal in the ROI was observed, 6.632 a.u respect to 0.583 a.u (see Figure 18). In deeper tissue the PA enhancement decreases significantly to approximately 1 a.u, but does not disappear due to the small injected amount (see Figure 18b, 18d and Figure 19). It is also worth to notice that no appearing toxicity or abnormalities were observed on the tested mouse monitored for 1 week after the experiment.

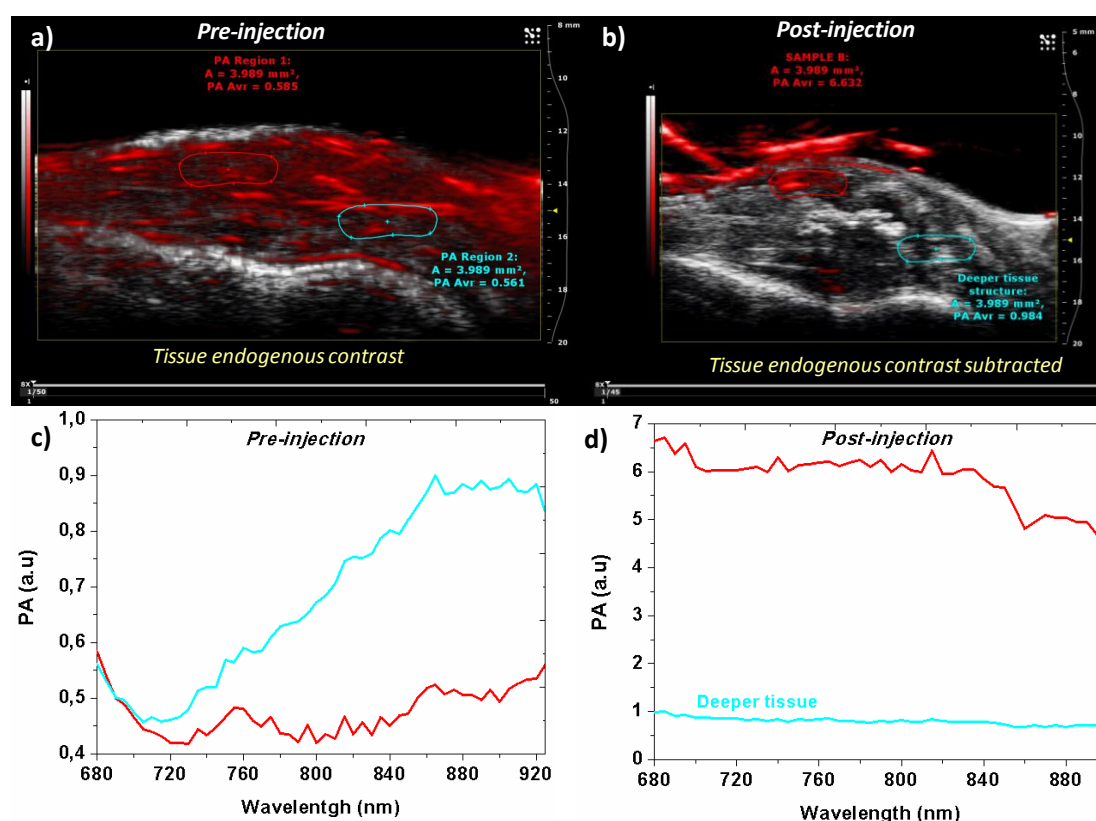


Figure 18. Real time In vivo PA images of subcutaneous injection of G/PVA MBs into normal mouse hind limb: a) Pre-injection tissue endogenous contrast, b) Post-injection tissue endogenous contrast subtracted, c) Pre-injection PA spectra, d) Post injection PA spectra, the spectra follow the color of the selected regions

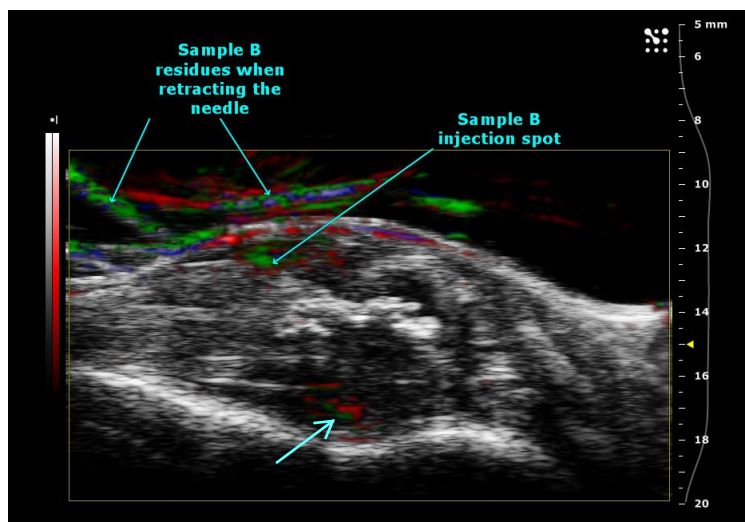


Figure 19. Real time In vivo PA unmixing response of G/PVA MBs (5% w/w) (green) with oxy-hemoglobin (red) and deoxy-hemoglobin (blue) after 30 μ l subcutaneous injection into mouse hind limb

Conclusion

The work discussed in this chapter has demonstrated the possibility to successfully incorporate few and single-layers graphene sheets almost free of defects, obtained by surfactant assisted ultrasonication into PVA soft microbubbles matrixes, and has shown good potential in PAI as assessed by in vitro and in vivo tests. Nonetheless, further tests will be addressed to study and optimize the PA response as a function of G/PVA doses.

The cytotoxicity of this hybrid system with respect to different graphene shell density will be evaluated using Fibroblast NIH 3T3 cells.

Chapter IV

References

- [1] Cavaliere, F.; ElHamassi, A.; Chiessi, E.; Paradossi, G. Stable Polymeric Microballoons as Multifunctional Device for Biomedical Uses: Synthesis and Characterization *Langmuir* **2005**, *21*, 8758-8764.
- [2] Baretta, P.; Bordi, F.; Rinaldi, C.; Paradossi, G. A Dynamic Light Scattering Study of Hydrogels Based on Telechelic Poly(vinylalcohol). *J. Phys. Chem. B* **2000**, *104*, 11019-11026.
- [3] Coussot, G.; Nicol, E.; Commeyras, A.; Desvignes, I.; Pascal, R.; and Odile Vandenabeele-Trambouze, O. Colorimetric quantification of amino groups in linear and dendritic structures. *Polym Int.* **2009**, *58*, 511-518.
- [4] Noel, S.; Liberelle, B.; Robitaille, L.; and De Crescenzo, G. Quantification of Primary Amine Groups for Subsequent Biofunctionalization of Polymer Surfaces. *Bioconjugate Chem.* **2011**, *22*, 1690-1699.
- [5] Zhang, M.; Parajuli, R.R.; Mastrogiovanni, D.; Dai, B.; Lo, P.; Cheung, W.; Brukh, R.; Lam Chiu, P.; Zhou, T.; Liu, Z.; Garfunkel, E.; and He, H. Production of Graphene Sheets by Direct Dispersion with Aromatic Healing Agents. *Small* **2010**, *6*, 1100-1107.
- [6] Yang, H.; Hernandez, Y.; Schlierf, A.; Felten, A.; Eckmann, A.; Johal, S.; Louette, P.; Pireaux, J. J.; Feng, X.; K. Muellen, K.; Palermo, V.; Casiraghi, C. Simple Method for Graphene Production Based on Exfoliation of Graphite in Water Using 1-Pyrene Sulfonic Acid Sodium Salt. *Carbon* **2013**, *53*, 357-365.
- [7] Lotya, M.; Hernandez, Y.; King, P. J.; Smith, R. J.; Nicolosi, V.; Karlsson, L.S.; Blighe, F. M.; De, S.; Wang, Z.; McGovern, I. T.; Duesberg, G. S.; and Coleman, J. N. Liquid Phase Production of Graphene by Exfoliation of Graphite in Water/Surfactant Solutions *J. Am. Chem. Soc.* **2009**, *131*, 3611-3620.
- [8] Verboven, E.; D'Agostino, E.; D'Hooge, J.; Pfeiffer, H.; BouMatar, O.; Den Abeele, K. V. The Non Linear Coefficient Dispersion of Ultrasound Contrast Agents and The Challenges of Current Microbubble Oscillation Models. *In Proceedings of 2013 International Congress on Ultrasonics, Singapore, May 2013*; pp 882– 887.
- [9] Guardia, L.; Fernandez-Merino, M. J.; Paredes, J. I.; Solís- Fernandez, P.; Villar Rodil, S.; Martinez-Alonso, A.; Tascón, J. M. D. High-Throughput Production of Pristine Graphene in an Aqueous Dispersion Assisted by Non-Ionic Surfactants. *Carbon* **2011**, *49*, 1653–1662.

Chapter IV

[10] Pu, N. W.; Wang, C. A.; Liu, Y. M.; Sung, Y. ; Wang, D. S.; Ger, M. D. Dispersion of Graphene in Aqueous Solutions with Different Types of Surfactants and the Production of Graphene Films by Spray or Drop Coating. *J. Taiwan Inst. Chem. Eng.* **2012**, *43*, 140-146.

[11] Mak, K. F.; Ju, L.; Wang, F.; Heinz, T. F. Optical Spectroscopy of Graphene: From the Far Infrared to the Ultraviolet. *Solide State Commun.* **2012**, *152*, 1341-1349.

[12] Tzvetkov, G.; Paradossi, G.; Tortora, M.; Fernandes, P. ; Fery, A. ; Graf-Zeiler, B. ; Fink, R. H. Water-Dispersible PVA-Based Microballoons with Potential for Biomedical Applications. *Mater. Sci. Eng C.* **2010**, *30*, 412-416.

[13] Kim F.; Cote, L. J.; and Huang, J. Graphene Oxide: Surface Activity and Two-Dimensional Assembly *Adv. Mater.* **2010**, *22*, 1954-1958.

[14] Wakamatsu, T.; Numata, Y. Flotation of Graphite. *Miner. Eng.* **1991**, *4*, 975–982.

[15] Ferrari, A. C.; Meyer, J. C.; Scardaci, V.; Casiraghi, C.; Lazzeri, M.; Mauri, F.; Piscanec, S.; Jiang, D.; Novoselov, K. S.; Roth, S.; Geim, A. Raman Spectrum of Graphene and Graphene Layers. *Phys. Rev. Lett.* **2006**, *97*, 187401–187404.

[16] Ferrari, A. C. Raman Spectroscopy of Graphene and Graphite: Disorder, Electron-Phonon Coupling, Doping and Non Adiabatic Effects. *Solid State Commun.* **2007**, *143*, 47–57.

[17] Schedin, F.; Lidorikis, E.; Lombardo, A.; Kravets, V. G.; Geim, A. K.; Grigorenko, A. N.; Novoselov, K. S.; Ferrari, A. C. Surface- Enhanced Raman Spectroscopy of Graphene. *ACS Nano* **2010**, *4*, 5617–5626.

[19] Dopa, D.; Sun, Z.; Torrise, F.; Ferrari, A. C. Sub 200 fs Pulse Generation from a Graphene Mode-Locked Fiber Laser. *App. Phys. Lett.* **2010**, *97*, 203106.

[20] Poehlmann, M.; Grishenkov, D.; Kothapalli, S. V. V. N.; Harmark, J.; Hebert, H.; Philipp, A.; Hoeller, R.; Seuss, M.; Kuttner, C.; Margheritelli, S.; Paradossi, G.; Fery, A. On the Interplay of Shell Structure with Low-and-High-Frequency Mechanics of Multifunctional Magnetic Microbubbles. *Soft Matter* **2014**, *10*, 214-226.

[21] Park, M. H.; Kim, T. H.; Yang, C. W. Thikness Contrast of Few- Layered Graphene in SEM. *Surf. Interface Anal.* **2012**, *44*, 1538–1541.

Chapter IV

[22] Jasim, D. A.; Ménard-Moyen, C.; Bégin, D.; Bianco, A.; Kostarelos, K. Tissue Distribution and Urinary Excretion of Intravenously Administrated Chemically Functionalized Graphene Oxide Sheets. *Chem. Sci.* **2015**, *6*, 3952–3964.

[23] Rabiou, M.; Mensah, S. Y.; Abukari, S. S.; Amekpewu, M.; Sefa- Ntiri, B.; Twum, A. Generation and Propagation of Ultrasonic Waves in Piezoelectric Graphene Nanoribbon. *OJA* **2013**, *3*, 38–42.

[24] Chivukula, V. S.; Ciplys, D.; Kim, J. H.; Rimeika, R.; Xu, J. M.; Shur, M. S. Surface Acoustic Wave Response to Optical Absorption by Graphene Film Composite. *IEEE Trans. Ultrason. Eng.* **2012**, *59*, 265–270.

[25] Xu, M.; Wang, L. V. Photoacoustic Imaging in Biomedicine. *Rev. Sci. Instrum.* **2006**, *77*, 041101–041122.

[26] Chen, J.; Lin, R.; Wang, H.; Meng, J.; Zheng, H.; Song, L. Blind Deconvolution Optical Resolution Photoacoustic Microscopy In Vivo. *Opt. Express* **2013**, *21*, 7316–7327.

[27] Wu, D.; Huang, L.; Jiang, M. S.; Jiang, H. Contrast Agents for Photoacoustic and Thermoacoustic Imaging: A review. *Int. J. Mol. Sci.* **2014**, *15*, 23616–23639.

[28] Lalwani, G.; Cai, X.; Nie, L.; Wang, L. V.; Sitharaman, B. Graphene Based Contrast Agents for Photoacoustic and Thermoacoustic Tomography. *Photoacoustics* **2013**, *1*, 62–67.

[29] Patel, M. A.; Yang, H.; Chiu, P. L.; Mastrogiovanni, D. D. T.; Flach, C. R.; Savaram, K.; Gomez, L.; Hemnarine, A.; Mendelsohn, R.; Garfunkel, E.; Jiang, H.; He, H. Direct Production of Graphene Nanosheets for Near Infrared Photoacoustic Imaging. *ACS Nano* **2013**, *7*, 8147–8157.

[30] Moon, H.; Kumar, D.; Kim, H.; Sim, C.; Chang, J. H.; Kim, J. M.; Kim, H.; Lim, D. K. *ACS NANO* **2015**, *9*, 2711.

[31] Yang, K.; Hu, L.; Ma, X.; Ye, S.; Cheng, L.; Shi, X.; Li, C.; Li, Y.; Liu, Z. Multimodal Imaging Guided Photothermal Therapy Using Functionalized Graphene Nanosheets Anchored With Magnetic Nanoparticles. *Adv. Mater.* **2012**, *24*, 1868–1872.

[32] Sheng, Z.; Song, L.; Zheng, J.; Hu, D.; He, M.; Zheng, M.; Gao, G.; Gong, P.; Zhang, P.; Cai, L. Protein-assisted Fabrication of Nanoreduced Graphene Oxide for Combined in Vivo Photoacoustic Imaging and Photothermal Therapy. *Biomaterials* **2013**, *34*, 5236–5243.

Chapter IV

[33] Jastrzębska, A. M.; Kurtycz, P.; Olszyna, A. R. Recent Advances in Graphene Family Materials Toxicity Investigations. *J. Nanopart. Res.* **2012**, *14*, 1320–1328.

[34] Bianco, A. Graphene Safe or Toxic? The Two Faces of the Medal. *Angew. Chem. Int. Ed.* **2013**, *52*, 4986-4997.

[35] Guo, X.; Mei, N. Assessment of the Toxic Potential of Graphene Family Nanomaterials. *J. Food. Drug. Anal.* **2014**, *22*, 105-115.

[36] Kanakia, S.; Toussaint, J. D.; Chowdhury, S. M.; Tembulkar, T.; Lee, S.; Jiang, Y. P.; Lin, R. Z.; Shroyer, K. R.; Moore, W.; Sitharaman, B. Dose Ranging Expanded Acute Toxicity and Safety Pharmacology Studies for Intravenously Administrated Functionalized Graphene Nanoparticle Formulations. *Biomaterials* **2014**, *35*, 7022-7031.

Chapter V:

Effect of Diamine Intermediate on Graphene PVA MBs and Cytotoxicity Evaluation

Chapter V

1. Introduction

In this chapter we aim to determine how diamine intermediate allows the tethering of graphene onto the PVA MBs shells and influences the properties of the hybrid microbubbles. The herein studied diamines were selected as a function of their length, varying from a short alkylene carbon chain to PEG backbones with different molecular weights. Such diamines were conjugated to the surfactant stabilizing graphene as described in the previous chapter. The interest behind this study is to introduce a modification on the steric hindrance, flexibility and hydrophilicity when incorporating moieties ranging from saturated carbon chains to PEG's with different molecular weights. PEGylation has been remarkably used in the biomedical literature for several purposes i.e. from polymers functionalization, to fabrication of nanoparticles and core/shell systems. In the latter case, it has been proved that in addition to preventing the immune recognition of the material, it modifies the interface characteristics of the particle with the solvent medium.^[1,2] Hence, PEGylation can offer a better control on the optimization of the G/PVA MBs properties in terms of stability, photo-acoustic efficiency and biocompatibility.

2.1. Materials

The following materials were all purchased from Sigma Aldrich, Milan, Italy: poly(vinyl alcohol) (PVA) with a number-average molecular weight, M_n , and weight average molecular weight, M_w , of 30 ± 5 and 70 ± 10 kg/mol, respectively; sodium metaperiodate (NaIO_4); pentamethylene diamine (PMDA); polyethylene glycol diamine with molecular weight 2000 and 6000 (PEGDA2000 and PEGDA6000, respectively); orange II sodium salt; glycolic acid ethoxylate-4-nonyphenyl ether; synthetic graphite powder with particle size $< 20 \mu\text{m}$; N-(3-Dimethylaminopropyl)-N'-ethyl-carbodiimide hydrochloride (EDC); N-hydroxy-succinimide 98% (NHS); MES 99%, acetic acid, thiazolyl blue tetrazolium bromide (MTT) and Dulbecco's modified Eagle's medium (DMEM). Methanol (MeOH) and sodium cyanoborohydrate 95% powder (NaCNBH_3) were purchased from Carlo Erba, Milan, Italy, and Alfa Aesar, Heysham UK, respectively. mQ quality water ($18.2 \text{ M}\Omega\text{-cm}$) was produced using a deionization apparatus Pure Lab from USF (Perugia, Italy). Mouse fibroblast cell line

Chapter V

NIH 3T3 was obtained from Istituto Zooprofilattico della Lombardia e dell'Emilia Romagna.

2.2. Methods

2.2.1. Diamine Surface Modification of PVA Microbubbles and Graphene Functionalization

Surface functionalization of PVA MBs shell with different diamine intermediates i.e. PMDA, PEGDA2000 and PEGDA6000, was achieved by reductive amination. Typically, an excess amount of diamines molecules was added to the PVA MBs. The pH of the mixtures was adjusted to 5 using an acetate buffer (0.03 M CH₃COOH, and 0.02 M CH₃COONa) followed by the addition of NaCHBH₃. The microbubbles suspensions were slowly stirred at room temperature for 4 day using a vortex at 500 rpm. The resulting microbubbles products i.e. PVA-PMDA, PVA-PEGDA2000 and PVA-PEGDA6000, were finally washed with mQ water by several step centrifugations.

2.2.2. Primary Diamine Quantification of PVA Microbubbles Modified Surfaces:

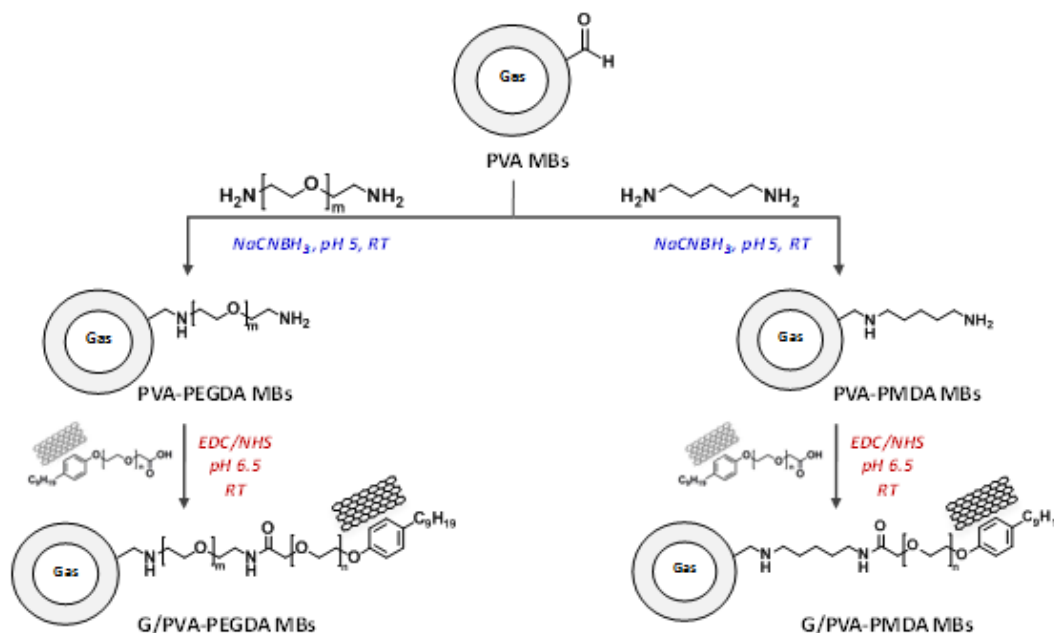
The available primary amine groups on PVA-PMDA, PVA-PEGDA6000 and PVA-PEGDA2000 were quantified by Orange II (O-II) dye method.^[3] A 1mg/ml solution of Orange II sodium salt (pH 3) was prepared in mQ water, the pH was adjusted using HCL 1M. The MBs samples at a concentration of 10⁸ MBs/ml were sonicated for 10 min in a sonicator bath, and then re-dispersed in the acidic solution. Fixed amounts of the Orange II dye solution were added step-by-step. At each addition, microbubbles were incubated for 15 min at 40°C, and then centrifuged for 10 min at 2500 rpm. The absorbance of the unbound dye in the supernatant was measured spectrophotometrically at 485 nm.

2.2.3. Graphene PVA Diamine Microbubbles Functionalization:

Graphene sheets were tethered to each type of diamine modified microbubbles surfaces with a content of 5% (w/w), as described previously in Chapter IV section 2.2.4, through the carboxylic moiety of its stabilizing surfactant and the primary amine groups on the microbubbles shells via EDC/NHS chemistry at pH 6.5 using a MES buffer. The overall reaction is shown in scheme (1) below. The resulting G/PVA-

Chapter V

PMDA, G/PVA-PEGDA2000 and G/PVA-PEGDA6000 were washed by mQ water and sonicated (when necessary) for 2 min in a water bath sonicator at 50% of power to redisperse the aggregates formed by π - π stacking of the graphene sheets, then stored as freeze-dried powders.



Scheme 1. Graphene PVA microbubbles functionalization with pentamethylene diamine and PEG diamine (2000 and 6000).

2.2.4. Acoustic Attenuation Measurements of Graphene PVA Diamines Microbubbles:

Acoustic attenuation measurements were carried out using the same set-up described in chapter (4) for PVA and G/PVA MBs. The received signals were processed by comparison with the signals from the mQ water medium taken as a reference. The amplitude fundamental was optimized to 0.35 V, then known amounts of G/PVA-PMDA, G/PVA-PEGDA2000 and G/PVA-PEGDA6000 MBs were added respectively and compared to the same batch of plain PVA MBs 11 days after its preparation.

2.2.5. MTT Cytotoxicity Assay of Graphene PVA Diamines Microbubbles:

For MTT assay, typically, 5×10^4 NIH 3T3 fibroblasts were seeded in 24-well plates and cultured in DMEM supplemented with 2 mM L-glutamine, 1% penicillin/streptomycin and 10% FBS at 37°C in a humidified atmosphere containing

Chapter V

5% CO₂. The Well plates containing the cells were left for 12 hours in incubator (HeraCell 150i, ThermoScientific) to allow cell adhesion. Afterwards, 900 µl of DMEM and 100 µl corresponding to amounts ranging from 10⁵ to 10⁸ of each PVA, G/PVA-EDA, G/PVA-PMDA, G/PVA-PEGDA2000 and G/PVA-PEGDA6000 were added. The microbubbles were transformed into capsules by sonication prior to addition.

After 24 h contact, the cells were washed twice with PBS and incubated for 4 h with MTT at a final concentration of 0.5 mg/ml in serum-free DMEM, at 37 °C under 5% CO₂. Medium was removed after the incubation period and the insoluble formazan crystals produced by live cells were solubilized with DMSO. The plate was protected from light and put on an orbital shaker for 5 minutes. Then, the absorbances at 570 nm and at 650 nm (background) were registered by spectrophotometer (Jasco V-630). The cell viability was expressed as percentage value representing mitochondrial activity (see equation 1). Non-treated cells (NT) i.e. without being in contact with the microbubbles were used as control.

$$Cell\ Viability\ (\%) = \frac{(Abs\ MB)_{570} - (Abs\ MB)_{650}}{(Abs\ NT)_{570} - (Abs\ NT)_{650}} \times 100 \quad (1)$$

where Abs is the absorbance, MB represents a graphene PVA-diamine microbubbles treated sample, and NT is the control.

Data were statistically analyzed using the paired Student t-test within the groups (* = p<0.05).

3. Results and discussion:

3.1. Diamine functionalization of PVA microbubbles:

The quantification of available primary amine groups on the modified PVA MBs revealed a decrease as the diamine carbon chain length increases. With PVA-EDA and PVA-PMDA MBs similar results are obtained, whereas the diamine PEGylated MBs have shown a significant decrease of the number of primary amine groups (see Figure 1 and Table 1), which could be due either to the initial feed ratio or to the steric hindrance^[4] causing an effective masking of the available aldehyde groups on the shell surface of the microbubble.

Chapter V

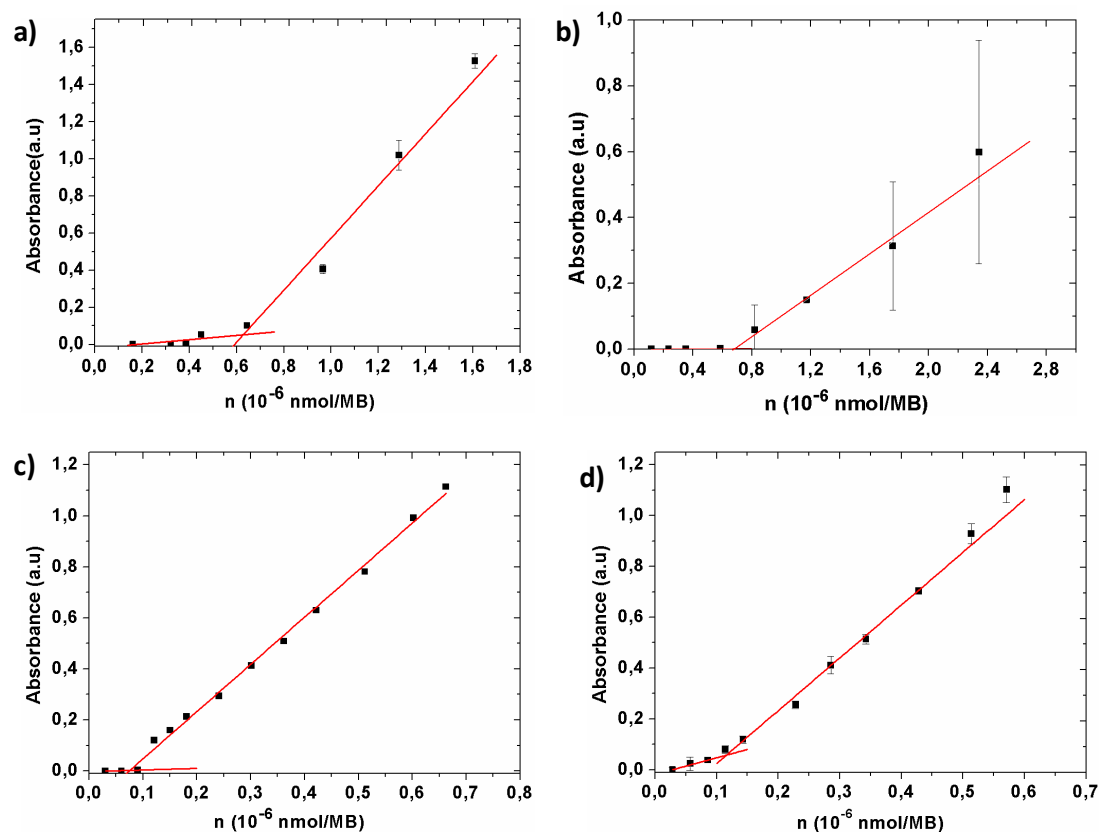


Figure 1. Diamine quantification of modified PVA MBs with Orange II: Orange II supernatant absorbance vs. the added amount of Orange II/MB: a) PVA-EDA, b) PVA-PMDA, c) PVA-PEGDA2000, d) PVA-PEGDA6000. Each titration was carried out in triplicate.

Table 1. Primary amine groups quantification on PVA modified microbubbles shell

Sample	PVA-EDA	PVA-PMDA	PVA-PEGDA2000	PVA-PEGDA6000
n_{DA}/MB (10^{-15} mol)	10	10	5	5
Normalized n_{DA}/NH_2	3.5×10^{-14}	6×10^{-14}	5.9×10^{-13}	1.8×10^{-12}
n_{O-II}/MB (10^{-15} mol)	0.64	0.69	0.074	0.11
SD	0.03	0.17	0.013	0.015

n_{DA} is the initial added amount of diamine

3.2. Graphene PVA-diamines microbubbles:

Tethering of graphene to the different PVA-diamines MBs with graphene content of 5% (w/w) was achieved by the “zero length spacer” EDC/NHS in which the carboxylic moiety of the surfactant stabilizing graphene was conjugated to the $-NH_2$ group of each of PVA-PMDA, PVA-PEGDA2000 and PVA-PEGDA 6000. All obtained MBs are dark grey colored suggesting a successful total tethering of the graphene sheets.

Chapter V

However, it was worth to notice that the longer the carbon chain of the diamine intermediate is, the better microbubbles are dispersed in their aqueous medium. The PEGylated G/PVA microbubbles exhibited a very good dispersibility, i.e., no microbubbles aggregates were observed upon their preparation and without a further sonication need (see Figure 2). This is due to an increase of the microbubbles hydrophilicity by the presence of ethylene-glycol repeats which have high water solubility ^[5]. Moreover, it is reported in the literature that surface PEGylation of small particles (from nano-to micrometer size) prevents their aggregation owing to passivated surfaces due to the presence of PEG chains which reduce the charge-based contact interactions (or zeta potential) between the PEGylated particles and molecules in the dispersing medium. ^[5,6] Thus, for G/PVA MBs the π - π stacking interactions between the graphene sheets causing microbubbles aggregation is minimized. This could be attributed to an increase in the flexibility of the spacing chains allowing the graphene tethering to the MBs which results in an increase of the steric distance between the sheets from the different microbubbles surfaces.

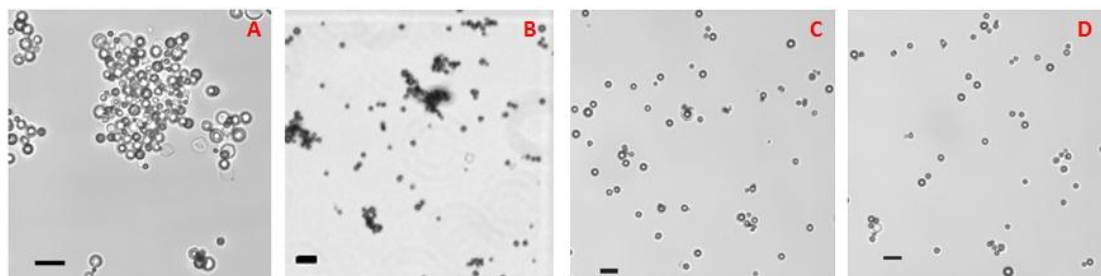


Figure 2. Bright field optical microscopy of G/PVA microbubbles without sonication: G/PVA-EDA MBs (A), G/PVA-PMDA MBs (B), G/PVA-PEGDA2000 MBs (C) and G/PVA-PEGDA6000 MBs (D) ($\times 40$) (The scale bars measuring $10\mu\text{m}$).

3.3. Acoustic Properties of Graphene/PVA-Diamines Microbubbles:

Figure 3 illustrates the dependence of the acoustic attenuation coefficient of G/PVA MBs with the different diamines intermediates from frequency in the range 1 – 20 MHz. All spectra reveal that the different types of microbubbles are active in the investigated ultrasound region and display an attenuation being proportional to the MBs concentration (see Figure 3a-b). Comparison with plain PVA MBs shows a

Chapter V

decrease of the acoustic attenuation and a shift in the resonance frequency, which increases as the diamine carbon chain gets longer (see Figure 2c-d). The ultrasound resonance of G/PVA-PEGDA2000 and G/PVA-PEGDA6000 shifts from a value of 8 MHz of plain PVA MBs to 10 MHz and 11 MHz, respectively. The addition of PEG chains affects the mechanical properties of PVA MBs shell as well as and as their acoustic behavior. Moreover, the bubbles concentration needed to achieve the same attenuation of the plain PVA MBs nearly doubles for G/PVA-PEGDA600. This decrease in microbubbles attenuation upon PEGylation has been recently reported in the literature and could indicate that the shell becomes more easily disrupted. [7]

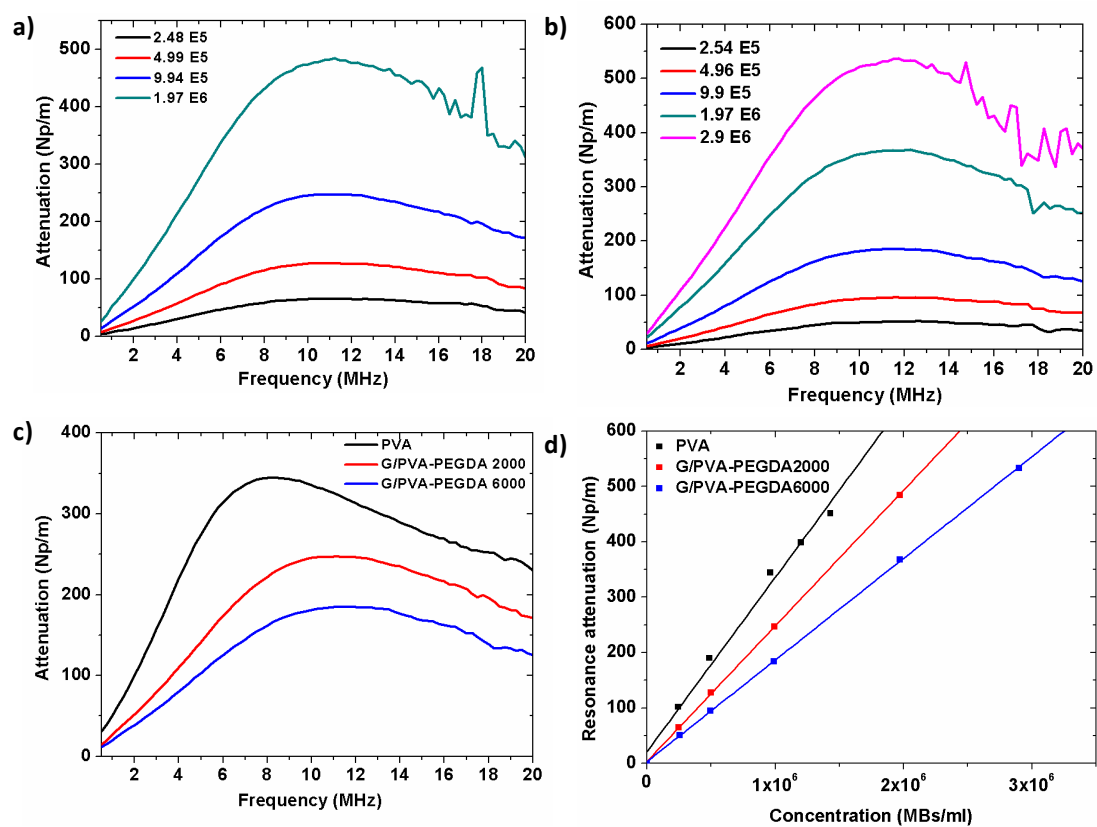


Figure 3. Acoustic attenuation spectra of G/PVA-PEGDA2000 and G/PVA-PEG6000 a) and b) respectively; comparison of acoustic attenuation spectra comparison at a concentration of 10^6 MBs/ml c); Resonance attenuation comparison between plain PVA MBs and G/PVA-DA MBs as a function of concentration.

3.4. Cytotoxicity Evaluation of Graphene/PVA-Diamines Microbubbles

The incidence of graphene on the biocompatibility of the modified PVA microbubbles with the different diamine intermediates was evaluated on fibroblasts NIH 3T3 cells, and compared to cytotoxicity of the PVA MBs. Figure 4a shows a good biocompatibility for all the tested systems, and most of the cells conserved their normal shape even at the highest microbubbles amount (see Figure 4b). However, a slight decrease in the cell viability to about 80% is observed at high microbubbles amounts (10^8 MBs) for the hybrid PEGylated microbubbles i.e. G/PVA-PEGDA MBs with respect to PVA MBs. It is worth to notice that G/PVA-EDA MBs shows a lower cell viability which decreases to 70% at 10^8 MBs than the G/PVA-PEGDA MBs. Nonetheless, the two studied molecular weight of the PEG diamine intermediates i.e. 2000 and 6000 have shown similar cell viabilities for the studied amounts ranging from 10^5 to 10^8 microbubbles. This finding indicates that PEGylation of G/PVA MBs should greatly reduce the toxicity of graphene in agreement with the literature investigating graphene materials toxicity.^[8,9]

Table 2. Graphene content on G/PVA MBs 5% (w/w)

MBs count	10^5	10^6	10^7	10^8
Graphene content (μg)	0.05	0.5	5	50

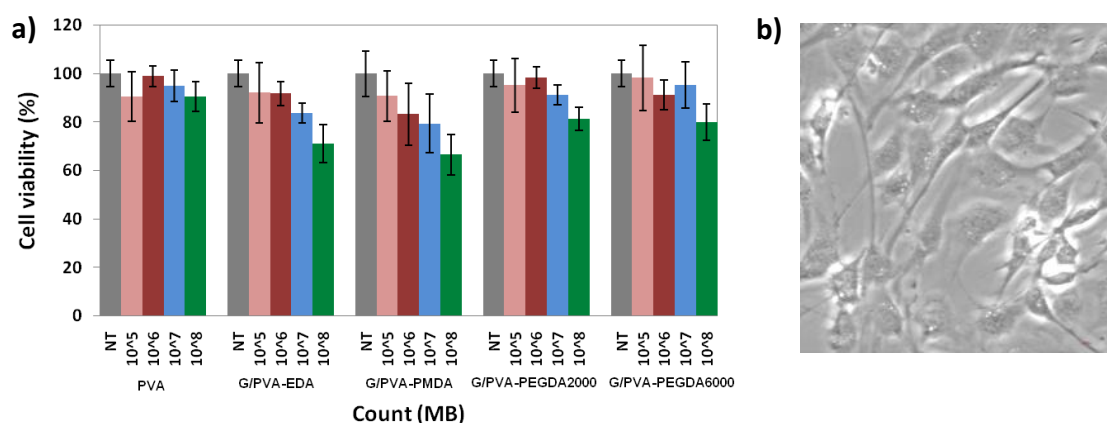


Figure 4. a) MTT assay of fibroblast NIH 3T3 (5×10^4 cells) treated with PVA and Graphene/PVA-diamines microbubbles (5% w/w) after 24 h incubation, error bars represent the standard deviation about the cell viability; b) Bright field optical microscopy image of cells after 24h incubation with 10^8 Graphene/PVA-EDA MBs ($\times 40$).

Chapter V

Conclusion

The study discussed in this chapter investigates the effect of diamine carbon backbone length on the behavior of G/PVA MBs in order to understand and overcome many of the challenges surrounding the future *in vivo* application of G/PVA MBs derivatives as PAI contrast agent and as “theranostic” systems. We have demonstrated that incorporating a PEG based diamine intermediate for the tethering of graphene onto the PVA MBs shows a better microbubbles dispersibility and enhances the biocompatibility of the hybrid contrast agent as tested on Fibroblast NIH 3T3 cells. It was worth to notice a different acoustic behavior of the PEGylated G/PVA MBs with respect to the G/PVA-EDA and G/PVA-PMDA MBs, which have shown similar attenuation properties to the plain PVA MBs. The lower PEGDA molecular weight i.e. 2000 resulted in a better acoustic performance and a similar cytotoxicity at the high doses as compared the higher PEGDA molecular weight i.e. 6000. We plan to continue developing and optimizing these G/PVA MBs, as they represent a great potential in PAI and for functionalization with bioactive molecules. Studies are ongoing to investigate biodistribution and to determine the targeting, drug loading, and delivery capabilities of these agents for applications in cancer therapy.

Chapter V

References

- [1] Harris J. M.; Martin N. E.; Modi M. Pegylation: a novel process for modifying pharmacokinetics. *Clin Pharmacokinet.* **2001**, *40*, 539-551.
- [2] Pozzi, D.; Colapicchioni, V.; Caracciolo, G.; Piovesana, Susy.; Capriotti, A. L.; Palchetti, S.; De Grossi, S.; Riccioli, A.; Amenitsch' H.; Laganà, A. Effect of polyethyleneglycol (PEG) chain length on the bio-nano-interactions between PEGylated lipid nanoparticles and biological fluids: from nanostructure to uptake in cancer cells. *Nanoscale* **2014**, *6*, 2782-2792.
- [3] Noel, S.; Liberelle, B.; Robitaille, L.; De Crescenzo, G. Quantification of Primary Amine Groups Available for Subsequent Biofunctionalization of Polymer Surfaces. *Bioconjugate Chem.* **2011**, *22*, 1690-1699.
- [4] Pasche, S.; Paul, S. M.; Vörös, J.; Spencer, N. D. ; Textor, M. Poly(L-lysine)-graft-poly(ethylene glycol) Assembled Monolayers on Niobium Oxide Surfaces: A Quantitative Study of Polymer Interfacial Architecture on Resistance to Protein Adsorption by ToF-SIMS and in-situ OWLS. *Langmuir* **2003**, *16*, 9216-9225.
- [5] Jokerst, J. V.; Lobovkina, T.; Zare, R. N.; Gambhir, S. S. Nanoparticle PEGylation for imaging and therapy. *Nanomedicine (lond)* **2011**, *6*, 715-728.
- [6] Misra, S. K.; Chang, H. H.; Mukherjee, P.; Tiwari, S.; Ohoka, A.; Pan D. Regulating Biocompatibility of Carbon Spheres via Defined Nanoscale Chemistry and a Careful Selection of Surface Functionalities. *Sci. Reports* **2005**, *5*, 14986.
- [7] Jablonowski, L. J.; Alfego, D.; Andorko, J. I.; Eisenbrey, J. R.; Teraphongphom, N.; Wheatley, M. A. Balancing Stealth and Echogenic Properties in an Ultrasound Contrast Agent with Drug Delivery Potential. *Biomaterials* **2016**, *103*, 197-206.
- [8] Miao, W.; Shim, G.; Lee, S.; Lee, S.; Choe, Y. S.; Oh, Y. K. Safety and Tumor Tissue Accumulation of Pegylated Graphene Oxide Nanosheets for Co-Delivery of Anticancer Drug and Photosensitizer. *Biomaterials* **2013**, *34*, 3402-3410.
- [9] Feng, L.; Liu, Z. Graphene in biomedicine opportunities and challenges. *Nanomedicine* **2011**, *6*, 317-324.

Concluding Remarks and Future Directions

The central objective of this dissertation was the design of pristine graphene PVA based composites to be used as drug carriers and as dual contrast agents for both ultrasound and photoacoustic imaging. The experiments conducted as part of this dissertation address these relevant research questions:

1. How to stably tether graphene prepared in an aqueous medium while preserving its pristine form, i.e. without passing by an oxidation process, to a PVA matrix?

Chapter II and Chapter IV introduce a simple way, taking spur of the recent literature about liquid phase production of graphene, to exfoliate the latter directly in water and tether it in only one step, and without any oxidation treatments that jeopardize its optical and electronic properties, to PVA platforms. This was achieved simply by the right choice of a surfactant which can enable good stabilization in water of the ultrasonically detached sheets from graphite by non-covalent interaction, and which bears the appropriate moieties to be covalently coupled with the functional groups of a PVA hydrogel or modified microbubble matrix. This exfoliation process resulted in graphene flakes in the range of 300 nm in size. The Raman spectroscopy analysis, used as finger print tool to assess graphene materials quality, presented and discussed in both chapters II and IV, and in agreement with morphological investigation results obtained by FESEM microscopy, revealed evidences of almost free defect single-and-few-layered graphene homogeneously incorporated to the PVA network or surface. Moreover, in this way an exceptional stability of the pristine graphene attached to the PVA polymer matrix was noticed over the time, without observation of any precipitation of residues for months, which is an asset for the biocompatibility of graphene.

2. How does graphene affect the features of the PVA matrix?

In chapter II, it was observed that the entrapment of graphene into a PVA-methacrylate crosslinked hydrogel network (PVAMA) increased significantly its storage modulus (G') which translates an increase of the stiffness resulting therefore in enhanced mechanical properties. Moreover DSC characterizations have shown that graphene enhances the thermal stability and acts as a nucleation agent in the crystallization process of the PVAMA. On the other hand, the work reported in chapter IV regards the coupling of graphene to PVA ultrasound active microbubbles, showing that the higher is the graphene feed ratio the more microbubbles tend to aggregate due to π - π stacking of the graphene sheets from different MBs. However, the aggregates can be separated by sonication without damaging the PVA shelled MBs as graphene confers to them an enhanced mechanical resistance, and the hybrid MBs can be stored as freeze-dried powders. The work also demonstrated that the original acoustic features of PVA MBs were maintained although microbubbles shells have been modified by a graphene coating. The characterization consisted on measuring acoustic attenuation caused by the as described microbubbles, and comparing it to the naked ones. No difference in the resonance frequency or attenuation amplitude was noticed when using graphene feed ratio of 5% (w/w). However in chapter V, a shift in the resonance frequency as well as diminution of attenuation were found as a result of a PEGylation process used as spacer in the graphene tethering.

3. How does graphene improve the functionalities of the hybrid system?

The coupling of graphene to PVAMA hydrogel (Chapter II) increase the anti-tumor drug (DOX) interaction through π - π interactions with aromatic rings as demonstrated by fluorescence studies. As described in Chapter III, the photoacoustic effect occurs when light hits an absorber and the thermal energy locally accumulated is converted and dissipated in mechanical energy by the emission of ultrasound waves and detected by a transducer. The light wavelength used in biomedical PAI is in the near

infrared (NIR) spectral window, where light is less attenuated by the tissue and water. Endogenous metabolites such as haemoglobin of red blood cells display a photoacoustic effect, similarly to other molecules absorbing in the same spectral range. This effect can be enhanced by exogenous devices as for example our hybrid assembly made by the stable coupling of pristine graphene with PVA microbubbles. The efficiency in the enhancement of the photoacoustic signal makes such device an unprecedented multimodal contrast agent for ultrasound and PAI. Graphene, with its strong absorbance in NIR almost independently from the wavelength, confers to the system a strong and wide spectral photoacoustic response even at very small doses with respect to the usual tested amounts of other chromophores reported in the literature. The preliminary photoacoustic results obtained from the mouse animal model regarding graphene PVA MBs (shown in Chapter IV) are very encouraging, in addition to not showing any apparent significant side effect at the tested doses.

4. How to define the graphene biocompatibility or toxicity limits?

One of the main considerations when addressing biomedical use of a material is its biocompatibility issue, in other terms up to which point the material becomes toxic for biological tissues? The few data discussing the different graphene derivative (GO and RGO) materials reported in biomedical related literature revealed dose dependence toxicity which can be decreased by enhanced stability and functionalization with other biocompatible materials. To this regard, PEGylation or other surface treatments could be necessary to increase circulation time and biocompatibility, reduce clearance by organs such as the liver, and decrease immunogenicity. However, there is still no clear evidence between the different derivatives concerning the oxidation effect on the graphene biocompatibility. Hence graphene exfoliation in surfactant aqueous solutions without modifying its structure by choosing the appropriate surfactant for further functionalization, such as with a biocompatible PVA polymer, and yielding to a reasonable quantity of pristine graphene sheets, is a potential utility. Moreover, we have shown that the graphene doses used *in vivo*, resulting in satisfactory PA signals and mechanical enhancement of PVA were much lower than the reported limit doses (20mg/Kg). In chapter V of

the manuscript, the cytotoxicity evaluation of the hybrid G/PVA MBs with a graphene feed ratio of 5% (w/w) resulted in cells viabilities larger than 80% for all the tested amounts of each sample, but with noticeable increase of viability at the highest doses when using PEG diamine intermediates.

In summary, the thesis work demonstrates that the potential of graphene can be easily implemented with a strategy applicable to diverse polymeric support. The strategy leaves intact the 2D planar structure of graphene and therefore preserves its original features. The coupling of graphene on practically any polymer surface can be accomplished in mild reaction conditions and in aqueous medium that is an issue of relevance in biologically addressed applications.

This work contains several elements of novelty:

- 1) The use of pristine graphene leaves unchanged its relevant properties.
- 2) A general strategy for attaching pristine graphene to a large number of hydrophilic polymer surfaces in a stable way using mild conditions and aqueous media
- 3) With this method we have assembled the true hybrid system where a hydrophobic moiety, i.e. graphene, is coupled with a hydrophilic moiety, i.e. the poly (vinyl alcohol) shelled microbubble, to obtain a novel multifunctional device implementing the potentialities of the photoacoustic imaging

Imaging and drug delivery are key in the next generation medicine. The issue is the disease detection in the earliest stages as it increases the chance of success of any therapy. PAI is among the imaging methods with the highest resolution and this allows in the less invasive way to detect at the very beginning a tumor. The targeting is key both for a localized diagnostic and to bring a drug focally to the diseased tissue. Therefore, graphene together with PVA microbubbles could be a potential for theranostics through surface bioconjugation with active molecular targets. As follow up of this thesis work, our group aims to test G/PVA MBs potential in targeting and drug delivery, and to determine the threshold dose, i.e. the best tradeoff between signal detection and toxicity. Biodistribution and bioelimination are other issues to

consider: what is the fate of the graphene/microbubbles hybrid assembly? Where the hybrid system is accumulated? What is the elimination curve? Further preclinical systematic studies to address these issues will be carried out within Acougraph project financed by the University of Rome Tor Vergata.

Appendix

Polymerized Surfactant Shell-Perfluorocarbon Filled- Micro/Nano-droplets for Ultrasound imaging applications

Appendix

1. Introduction:

In this appendix we present a preliminary study on the design of photo-crosslinked surfactant layers encapsulating a liquid perfluorocarbon (PFC) to obtain nano-and-microdroplets. The systems described below are based on diacetylene-bearing surfactants such as the 10, 12 pentacosynoic acid (PCDA), and on a very common surfactant, Tween 80. Basic characterization of the systems and acoustic droplet vaporization tests were performed for this study.

2. Materials:

The following materials were purchased from Sigma Aldrich, Milan, Italy: 10,12-pentacosadiynoic acid (PCDA), Tween 80, Span 60, (1,1,1,2,3,4,4,5,5,5)-decafluoropentane (DFP) with a boiling point of 55°C, and Nile Red. Perfluoropentane (PFP) with a boiling point of 29°C was purchased from Appollo Scientific-UK; Irgacure 2959 and Chlorofrom were purchased from from BASF (Milan, Italy) and Alfa Aesar, respectively. Milli-Q quality water (18.2 MΩ.cm) was produced by a deionization apparatus Pure Lab from USF (Perugia, Italy)

3. Methods:

3.1. Poly-PCDA-DFP/ PFP filled droplets preparation

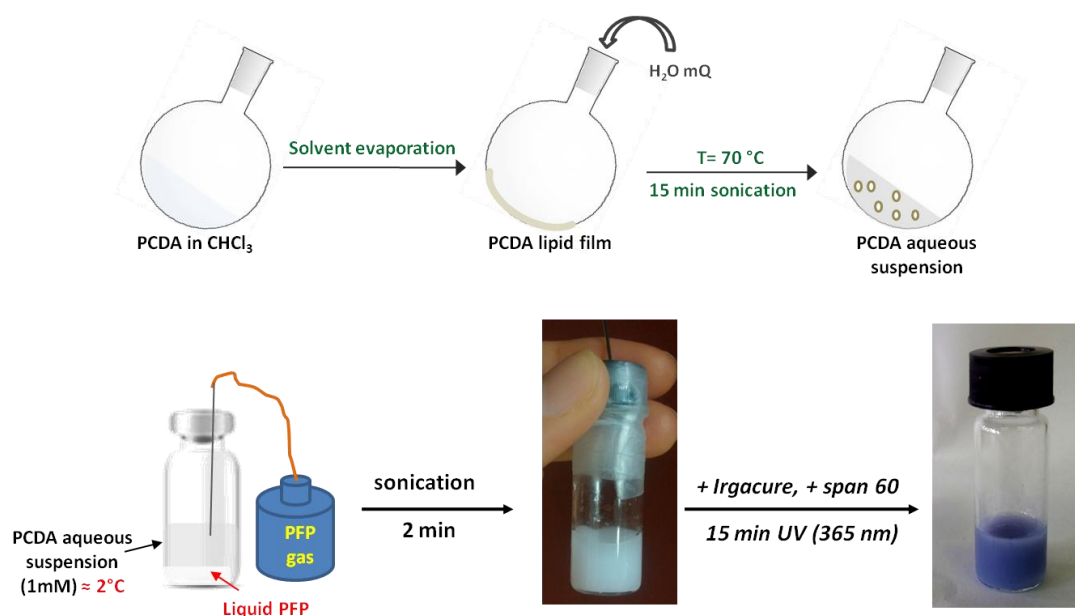
First, an aqueous solution of PCDA monomeric vesicles is prepared. Typically, 10 mg of PCDA powder are dissolved in 10 ml chloroform in a round-bottom flask. The solvent is then removed under vacuum for 4 hours using a rotary evaporator (Heidolph V V 2000, Milan, Italy) until a lipidic film is formed. The film is further dried overnight in a stove at 40°C. The PCDA lipid monomer is dispersed in mQ water at 70°C and sonicated for 15 min using a sonicator bath at 100% power and its concentration is adjusted to 1 mM. The obtained PCDA suspension is finally filtered using a 0.45 μm Nylon syringe filters.

PFC based droplets were formed through sonication of PCDA vesicle/micelle aqueous solution. For the DFP droplets preparation, 50 μL of DFP, 100 μL of Nile Red dye solution (60 μg/ml in Ethanol) and Irgacure 2959 (0.15 % w/v) are added to 1ml of PCDA monomer aqueous suspension at room temperature. The mixture is

Appendix

sonicated for 2 min using a sonicator bath at 100% power to lead to the droplets formation, and then 100 μ L of span 60 aqueous solution (10 mg/mL) is added as a stabilizer. The droplets are photopolymerized under 365 nm UV light for 10 min at a power of 400 W. The development of a blue color of the suspension is an evidence of the crosslinking reaction (see Scheme 1). For the PFP filled droplets; preparation is carried out following the same procedure but the PCDA aqueous suspension is first cooled at 2°C in order to condense the PFC added in gas state. Special care of the temperature is taken using ice in order to avoid the PFC evaporation prior to the droplets formation (see scheme1 below).

Photo-polymerized droplets are washed with mQ water by centrifugation at 1000 rpm for 5 min.



Scheme 1. Poly-PCDA PFC filled nanodroplets preparation procedure

3.2. Tween 80 droplets preparation

To 10 mL of tween 80 aqueous solution at a concentration of 0.1% (w/v) are added 0.5 ml of DFP and Irgacure at a concentration of 0.3 % (w/v). The mixture is then stirred using an ultraturax homogenizer at 13000 rpm for 15 min to ensure sufficient mixing and finally exposed to UV light at 365 nm for 10 min using a 400 W power lamp. The obtained microdroplets are washed with mQ water by centrifugation at

Appendix

1000 rpm for 5 min. For the labeled microdroplets 1ml of Nile red solution (60 µg/mL in ethanol) is mixed with the DFP prior to addition to the aqueous mixture. It is to be mentioned that submicron sized droplets can be obtained directly by sonication for 2 min in a water bath at 100% power instead of ultraturrax homogenizer.

The described droplets are counted using a Nauber chamber (0.25×0.25×0.1) µm and ImageJ software.

3.3. Dynamic light scattering (DLS)

The size distribution of poly-PCDA nanodroplets is determined by DLS. 1mL of 10 fold diluted solution of DFP/PFP filled poly-PCDA is put into a quartz cuvette. The measurements were carried out using DLS photometer and a BI-200SM goniometer with a BI-9000AT (Brookhaven Instruments Co.) correlation board equipped with a solid state laser source emitting at 532 nm, at 90°. Analysis of the autocorrelation function, $g_2(q,t)$, of the scattered intensity was carried out using the CONTIN algorithm provided as part of the standard instrument software package of the instrument.

3.4. Bright field, Fluorescence and CLSM microscopy

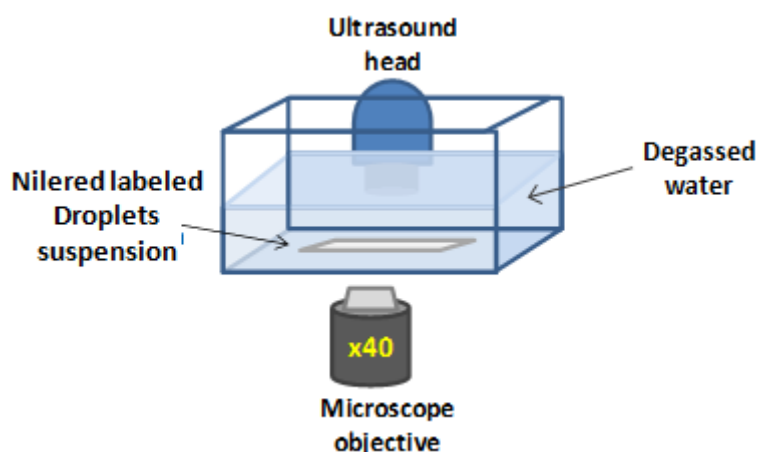
The following experiments and visualization of the different droplets samples were carried out using an inverted Eclipse model Ti-E microscope (Nikon Instruments, Japan) equipped with a 60×/1.4 oil immersion Plan Apo objective, an Ar+green laser ($\lambda_{exc} = 543$ nm) (Melles Griot, Carlsbad, CA), and a He-Ne laser ($\lambda_{exc} = 633$ nm) (Spectra Physics, Mountain View, CA). The droplet conversion to microbubbles was monitored by fluorescence and confocal microscopy on the Nile red labeled cores samples.

3.5. Acoustic droplets vaporization (ADV)

The ADV experiments are performed using a SP100 sonoprotator from SONIDEL™ (Dublin, IE). Typically, for each droplets systems described above, an “ibidi” channel chamber (Milan, Italy) is filled with 200 µL of 10 fold diluted droplets suspension and fixed in a polystyrene flask degassed water bath placed on the microscope. An

Appendix

ultrasound probe is placed in the water bath at 37°C and at 2cm height. Acoustic vaporization is carried out twice at 1 MHz central frequency, 100% duty cycle and 5W/cm² power for 30 s. The transition of nano/micro droplet-to-microbubble is followed by bright field and fluorescence microscopy on the nilered labeled samples (see [Scheme 2](#)).



Scheme 2. Acoustic droplet vaporization setup monitored by fluorescence microscopy.

3.6. Droplets preparation by microfluidics

The preparation of PCDA and Tween 80 encapsulating PFP or DFP droplets was also tested using a microfluidic technique carried out with a Tide Microfluidic technology (Twente, ND). This technique uses the outer fluid, or continuous phase, and the geometry of the microfluidic chip to confine the inner fluid, or disperse phase. As the fluids flow through the junction the disperse phase is confined and focused creating a point where it will break-up into small droplets or bubbles of uniform size. The dispersant solution (Tween80 or PCDA) allowing formation of the shell of the droplets and the PFC (PFP or DFP) liquid core were connected to the device through test tubes and fluxed into a microfluidic chip. The device and the chip geometry are described below in [Figure 1](#). The pressure of the dispersant and PFC was regulated to 2600 mbar and 2000 mbar, respectively. For the PFP filled droplets the test was carried out at room temperature. Collected samples were exposed to UV light at 365 nm for 20 minutes for polymerization using a 100 W UV lamp (7W/cm²).

Appendix

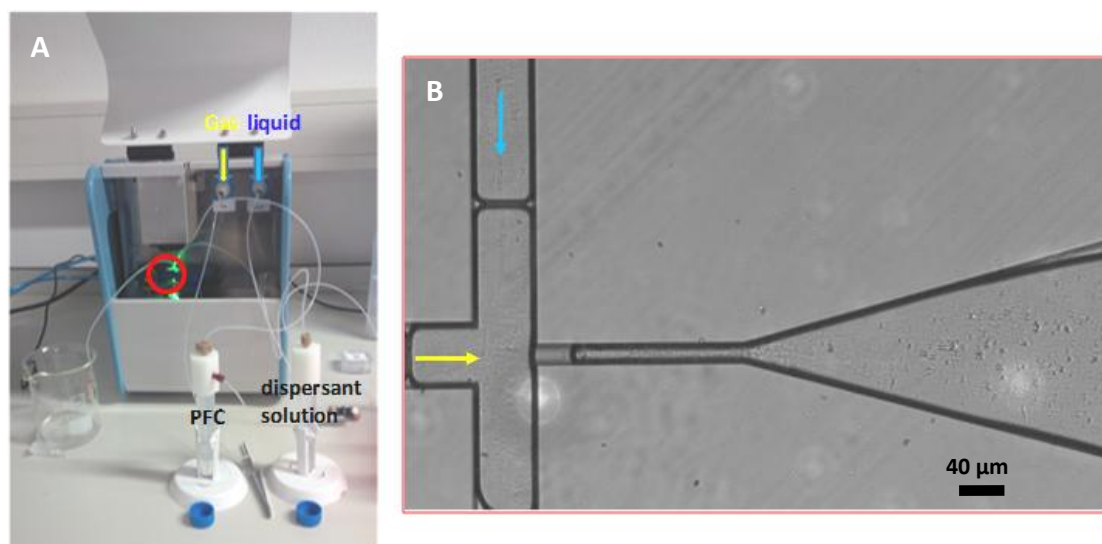


Figure 1. Microfluidic device photograph from “Tide microfluidics” for bubbles/droplets generation (A), optical micrograph of T-junction microfluidic chip (B).

4. Discussion

4.1. PCDA-PFC nanodroplets

Amphiphilic molecules can self-assemble into a monolayer shell at the interface between a gas/liquid core and the surrounding medium, allowing a good control of the shell surface architecture and flexibility.^[1] The self assembly properties of the PCDA monomer which acts like a surfactant make it ideal to form microemulsions of stabilized perfluorocarbons (PFC) nanodroplets with a polymerizable shell due to the presence of diacetylene moieties in its structure. The monomer should be orientated with its lipophilic tail towards PFC whereas its hydrophilic carboxylic head is towards the aqueous phase. The hydrophobic tails of PCDA bearing the diacetylene moieties can be polymerized by UV light, involving a 1,4-addition reaction which results in the conversion into a conjugated polymer shell with an alternating ene-yne sequences (see [Scheme 3](#)).^[2,3] The polymerized “poly-PCDA-PFC” nanodroplets aqueous suspension accordingly exhibits a more or less intense blue color (see [Figure 2a](#)) depending on the irradiation time and therefore on the crosslinking degree of the fatty acid chains, and show a maximum absorption at 670 nm (see [Figure 2b](#)).

Appendix

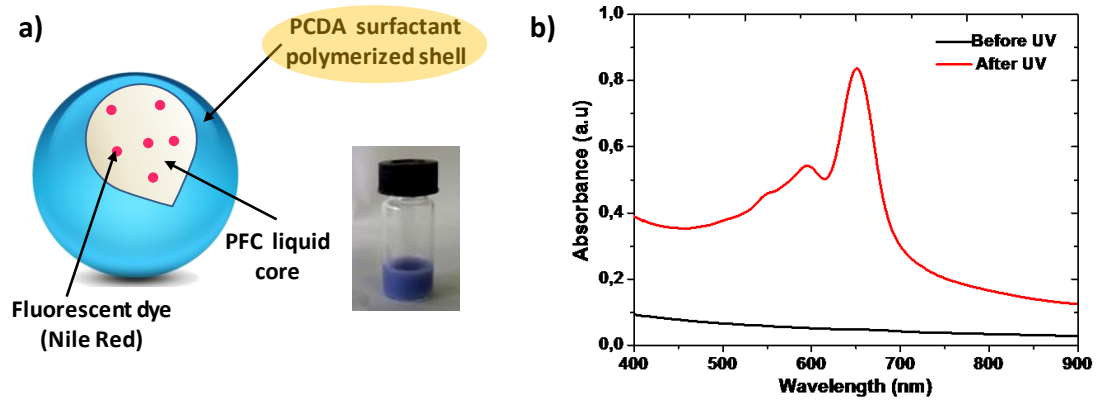
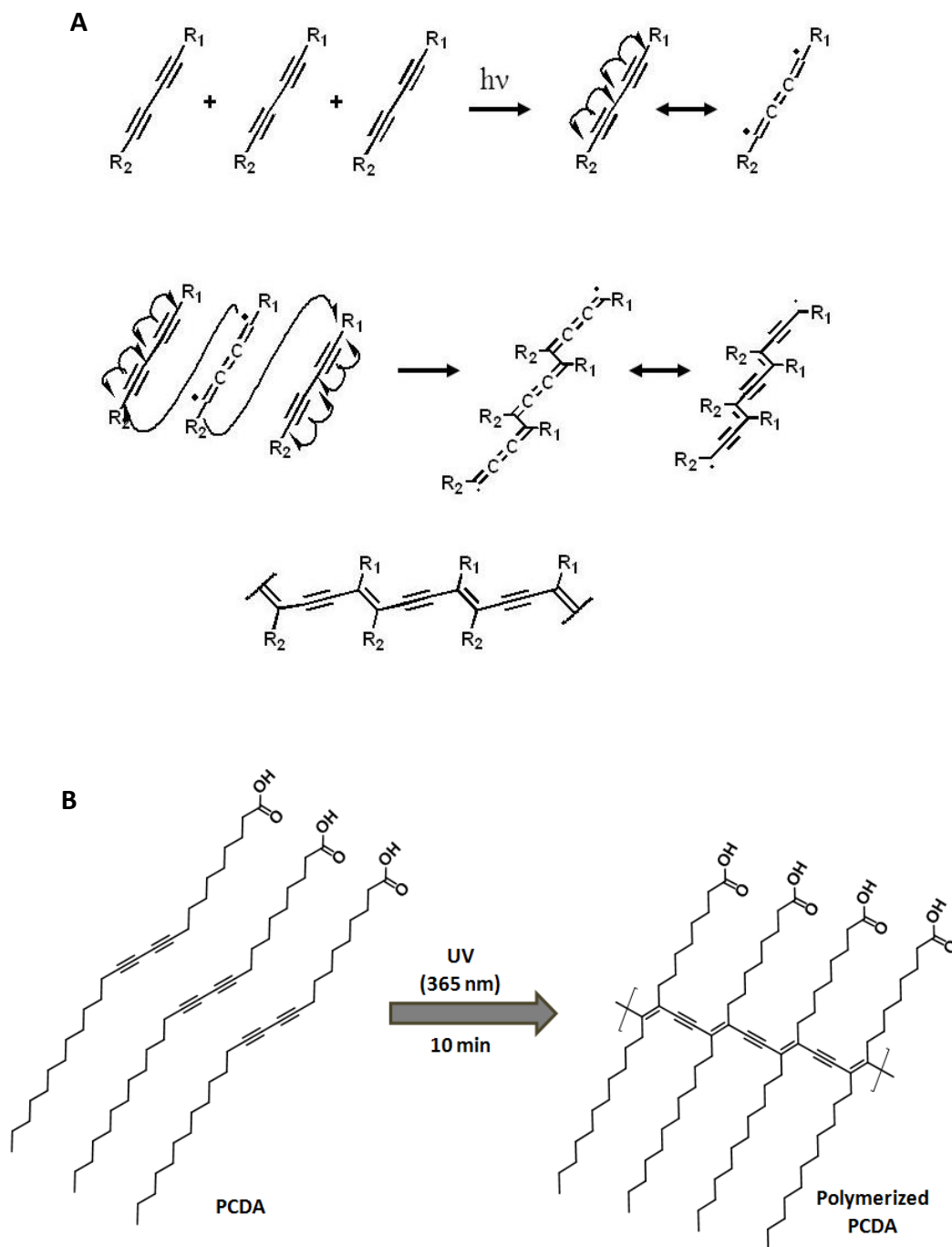


Figure 2. a) Schematic representation of crosslinked PCDA DFP/PFP nanodroplets, b) UV-vis-NIR absorbance spectrum of PCDA aqueous suspension before and after UV crosslinking.



Scheme 3. 1-4 addition polymerization mechanism of diacetylenes (A), PCDA cross-linking reaction (B).

Appendix

The colloidal stability of the nanodroplets is assessed by the absence of a coalescence process, typical of a physical assembled structure. In fact the suspension should remain stable within a period of time suitable for its storage and clinical administration. For this reason, systems formed by crosslinkable shells can offer some advantages with respect to the phospholipid shells counterparts. By using different UV exposure times, the surface properties of poly-diacetylenes such as PCDA vary in terms of elasticity and resistivity against gas dissolution according to the Laplace law discussed in the [Chapter III section 4.1](#).

The use of polydiacetylene functionalized phospholipid-PEGylated shells as ultrasound contrast agents was recently reported.^[4] Indeed, a study by Qin *et al.* demonstrated that the use of polydiacetylenes in liposome based structures make them stable against drug leakage, showing a potential for controlled drug delivery when activated by laser.^[5] Moreover, numerous studies in the literature report the biocompatibility of polydiacetylene particles and their efficient role in biosensing applications since they undergo a color transition as a response to photo-crosslinking, pH or temperature changes.^[6-8]

However, we believe that the simpler is the structure, the better is the understanding of the system behavior and evaluation of its performance with less parameters to be considered. By taking advantage of the surfactant behavior of PCDA and its polymerization capability, it is could be possible to make stable nanodroplets with a decreased shell thickness but with enhanced stability, which can be an asset for its acoustic performance.

In this work two based PFC droplets (DFP and PFP) with a poly-PCDA have been tested. The poly-PCDA-DFP droplets i.e. PFC with a boiling point of 55°C, exhibit a polydispersed size distribution with two averages populations of 500 nm and 2 μm (see [Figure 3](#)). The acoustic droplet vaporization using the parameters, described above in section 3.5 of this chapter, occurs only for droplets of more than 1 μm in size, whereas the submicron droplets need higher acoustic energy to lead to the vaporization of the DFP core upon ultrasound irradiation and an increase in the diameter up to 20 μm . This was clearly evidenced by fluorescence microscopy, in the droplets state, the NileRed labeled poly-PCDA-DFP appear fully fluorescent due to

Appendix

the hydrophobic interaction between the DFP liquid core and the dye. When droplets are transformed into microbubbles only a fluorescent ring appears due to the amphiphilic nature of the poly-PCDA shell and transformation of DFP into gas. Moreover, poly-PCDA-DFP droplets, kept at room temperature, show a reversible liquid to gas transition within 20 minutes after ultrasound application (see [Figure 5](#)). The reversibility phenomenon consists on the return from microbubble to droplet state and is due to the condensation of DFP gas as the energy has been dissipated and temperature decreases, the elasticity properties of the shell, as a result of the chemical crosslinking, play in principle an important role in the ADV reversibility.

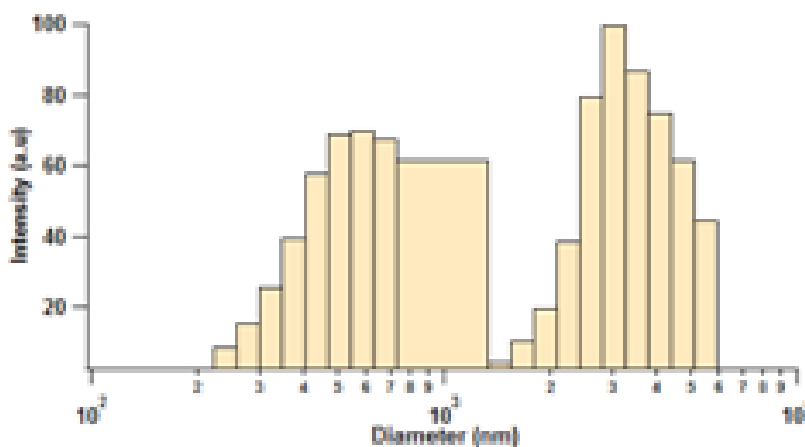


Figure 3. Poly-PCDA DFP droplets size distribution by DLS

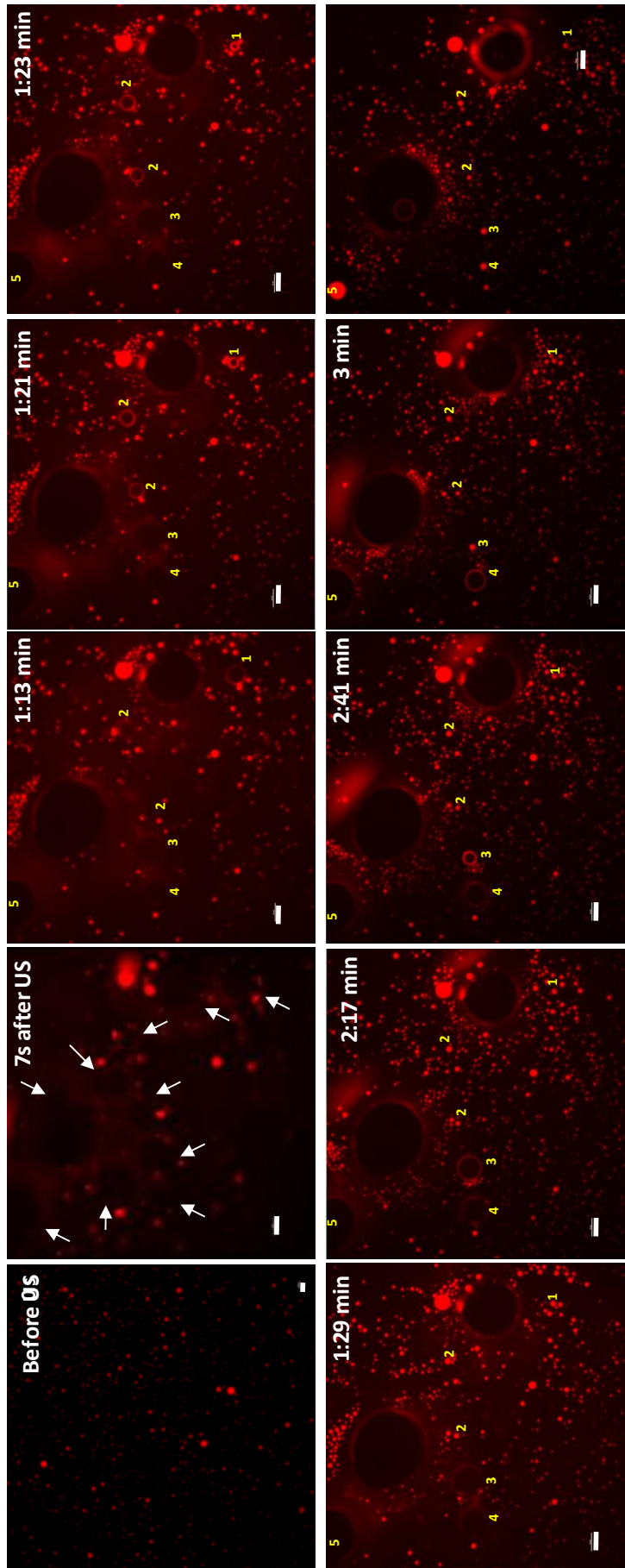


Figure 4. Real time Fluorescence microscopy images of PCDA-NileRed PFC labeled microdroplets (Barre scale 20 μ m). White arrows indicate MBs; Numbers indicate retransformation of MBs into microdroplets by order

Appendix

However, poly-PCDA-PFP droplets show a narrower size distribution as determined by DLS with an average diameter of 400 nm (see [Figure 5](#)). Indeed, the initial size of the nanodroplets is important to allow their extravasation within defective tumor tissues.^[9] These PFP nanodroplets exhibit a significantly more efficient ADV occurring for the major part of the submicron sized droplets respect to the DFP counterparts using the same setup parameters. Considering PFP boiling point is at 29°C, the core of the droplet is stabilized by the shell Laplace pressure and remains liquid at a temperature of 37°C. Increasing the temperature does not allow for its vaporization; only if an acoustic pressure is applied, the additional Laplace term increases the boiling point of the liquid core well above the physiological temperature.^[10] Nonetheless, by monitoring the formed MBs for a couple of hours at RT, reversibility was not observed as RT is not sufficient to allow for the condensation of the PFP gas and its return to the liquid state.

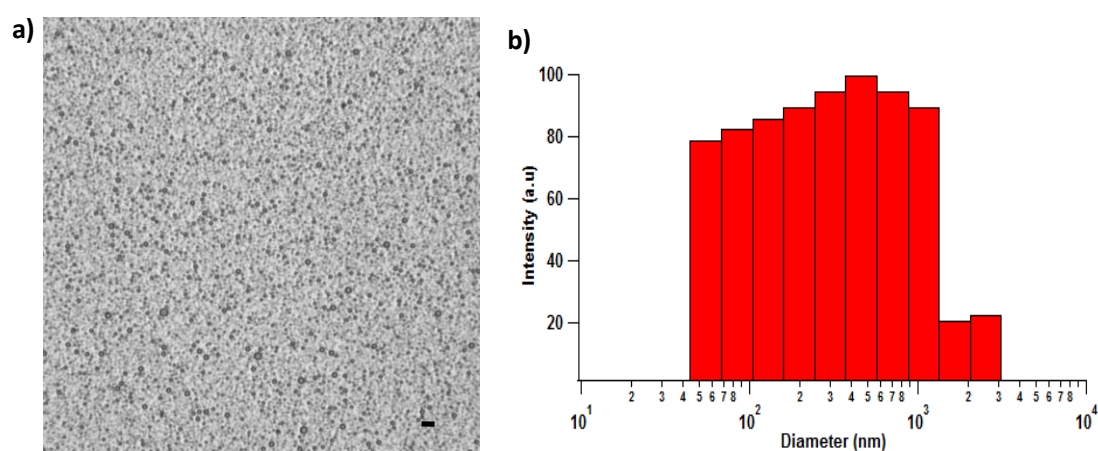


Figure 5. a) Bright field optical microscopy of poly-PCDA-PFP nanodroplets ($\times 40$); b) size distribution of poly-PCDA-PFP nanodroplets by DLS.

The [Figure 6](#) demonstrates that ultrasound mechanical waves enable the transition of the liquid PFP to gas and the passage from the labeled vesicles to MBs, appearing as fluorescent rings, with an increase in the average diameter from 400 nm to 8 μm . In both cases no coalescence effects were observed due to the crosslinking of the shell. The reported behavior opens a perspective on the future exploitation of the

Appendix

nanodroplet/microbubble transition for a combined imaging and therapeutic approach. The liquid hydrophobic core can be regarded as a drug reservoir to be targeted in the vicinity of the pathological tissue and, simultaneously, as a sonographic imaging enhancer, via US driven ADV. Finally MBs can be blasted, if properly excited by US, to release the drug payload.

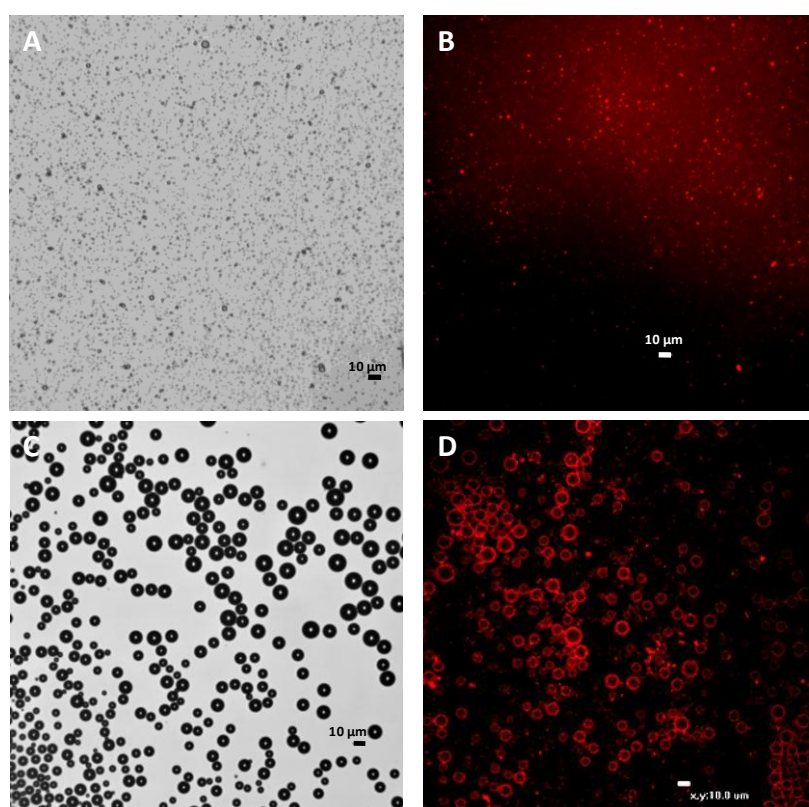


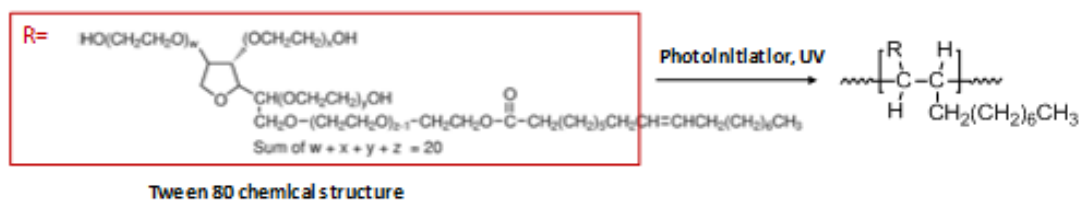
Figure 6. Nile Red labeled poly-PCDA-PFP nanodroplets before US: (A) bright field microscopy image and (B) fluorescence microscopy image; Nile Red labeled poly-PCDA-PFP microbubbles after US: (C) bright field microscopy and (D) confocal microscopy.

4.2. Tween 80-PFC droplets

Tween 80 is a non-ionic biocompatible surfactant commercially available and widely used in food and pharmaceutical industries and in the literature for biomedical applications either as a compound for formulations or as a stabilizing agent.^[11] The first surfactant based microbubbles, reported in the study of Singhal et. al, were produced by Tween 80 aqueous solution mixed with Span 60.^[12] Other studies report

Appendix

the use of Tween 80 to improve the stability of microbubbles/microdroplets made of phospholipids and to hinder their aggregation.^[4] Both of tween 80 and span 60 were not able to form microbubbles when not combined together or used with another emulsifier such as the polyoxyethylene 40 stearate called PEG40S. Herein, Tween 80 was used as a monolayer shell to formulate PFC filled microdroplets. The vinyl moiety in the surfactant structure is susceptible to polymerize upon UV irradiation when using a photoinitiator^[13] which would afford the microdroplet shell an enhanced stability for avoiding coalescence (see Scheme 4).



Scheme 4. Tween 80 polymerized shell structure

The fabricated and polymerized Tween 80-DFP as described in section 3.2 microdroplets precipitate rapidly due to the higher density than water of the liquid PFC and show an average diameter of 4 μm (see Figure 7).

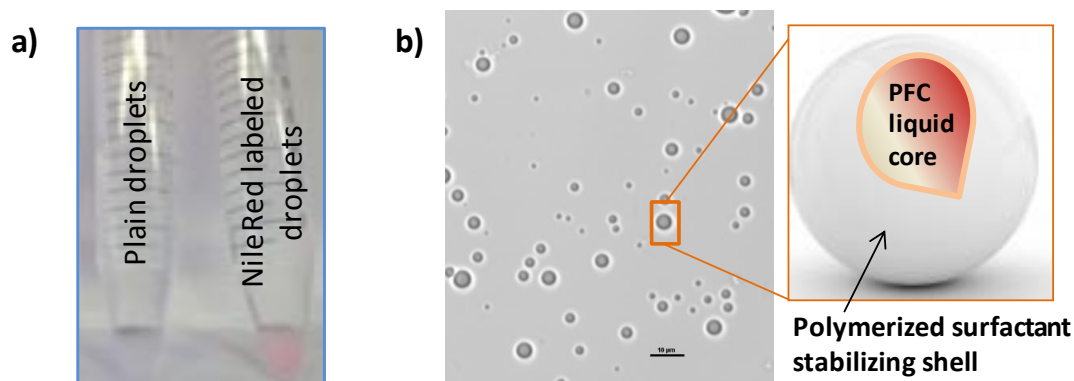


Figure 7. Tween 80 DFP microdroplets: a) photograph of microdroplets suspension, arrows showing the microdroplets on the bottom of the tube; b) Bright field microscopy of Tween 80-DFP microdroplets suspension ($\times 40$ _ barre scale $10\mu\text{m}$).

Appendix

After US irradiation, microdroplets increased from 4 μm to 30 μm in diameter, after monitoring the droplets for 2 hours no reversibility was observed which must be probably due to the high viscous nature of Tween 80.

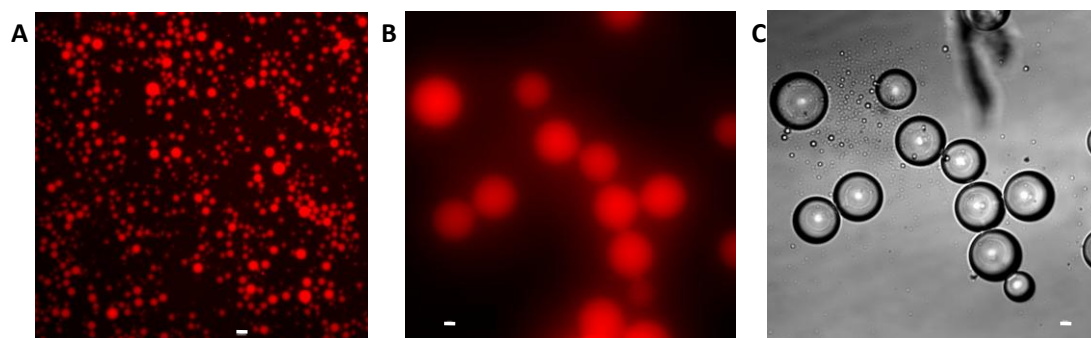


Figure 8. Tween 80-NileRed labeled DFP microdroplets (x40): Fluorescence microscopy Before US (A), Fluorescence microscopy after US (B), Bright field optical microscopy after US; barre scale (10 μm).

5. Formulation of PFC droplets by Microfluidics

Microfluidic devices are known for their ability to create microdroplets, bubbles or particles with high monodispersity.^[4, 14-16] This is due to the techniques of particles generation, where each bubble or droplet is created individually. Hence, the ability to produce the droplets described above i.e. poly-PCDA and Tween 80 filled PFP and DFP liquid cores has been tested by a microfluidic device in order to optimize the size distribution and obtain a monodisperse system. The experiment was run as a proof of concept and it is worth to mention that the used chip device is not appropriate for small sized droplets below 10 μm , and optimization of the chip channels must be considered. Nonetheless, both DFP and PFP PCDA filled droplets have shown a good size distribution as observed by optical microscopy (see Figure 8 B and D) with an average diameter of 1 μm . It was noticed during the experiment running production of some microbubbles from 10 to 20 μm when using PFP at a room temperature due to the applied pressure inside the chip (see Figure 8 C). However production Tween 80- DFP microdroplets show a good yield with an average diameter of 5 μm (see Figure 9) , the difference in size in the collected suspension is due to the variation of

Appendix

pressure during the experiment as some aggregates stuck at the inject input or output.

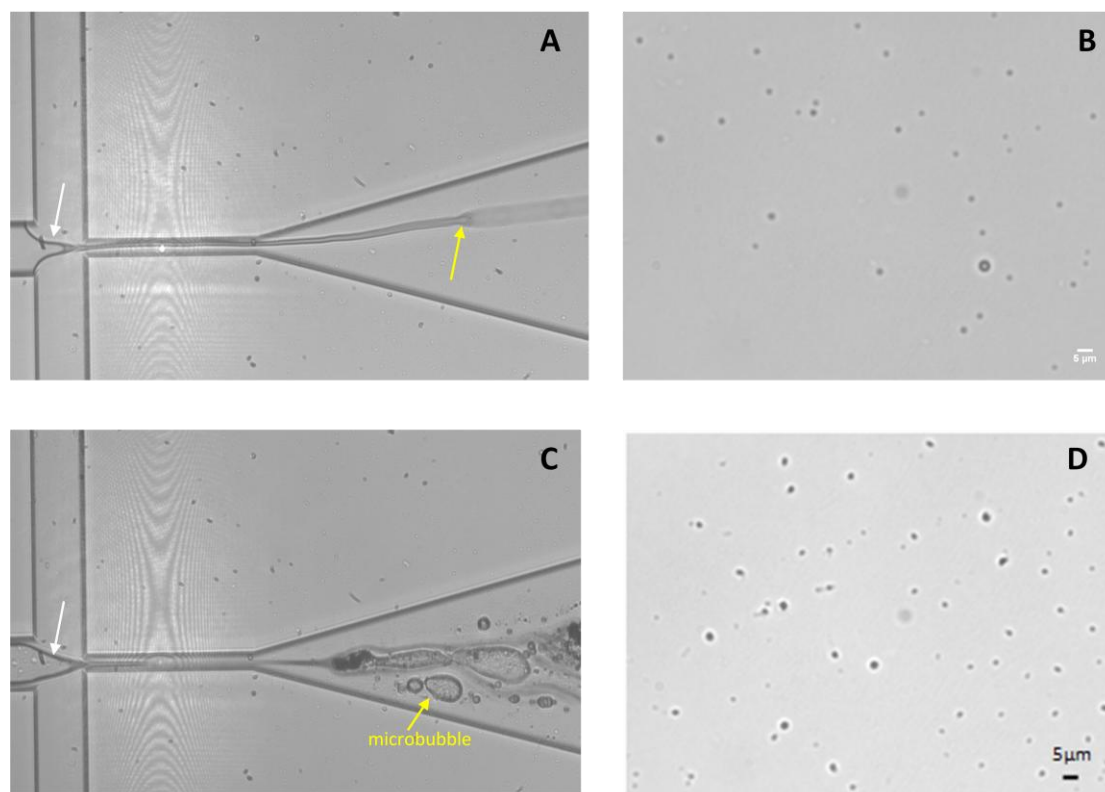


Figure 8. (A) Real-time Optical image of PCDA-DFP droplets generation by microfluidics at RT, the white arrow shows the aqueous PCDA solution-DFP interface and the yellow arrow indicates the generated micro/nanodroplets flow; (B) optical microscopy of collected poly-PCDA-DFP sample; (C) Real-time Optical image of PCDA-PFP droplets generation by microfluidics at RT; (D) optical microscopy of collected PCDA-PFP sample.

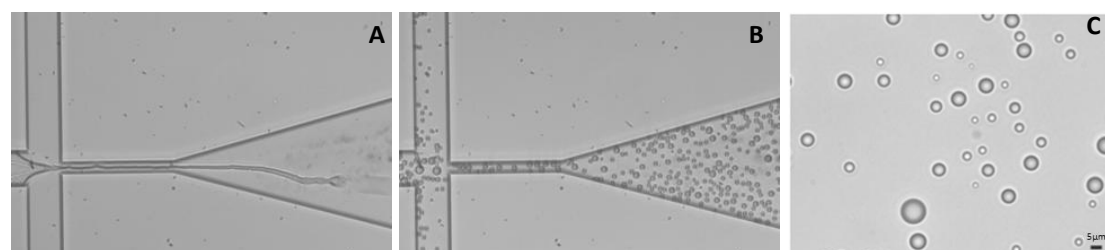


Figure 9. (A) Real-time Optical image of Tween 80-DFP microdroplets generation by microfluidics at RT; (B) Microdroplets fluxing back in the chip after experiment running; (C) optical microscopy of the collected Tween 80-DFP sample.

Appendix

6. Conclusion and perspectives

These results discussed in this appendix are preliminary but show that stable monolayer shelled PFC filled nano-and-micro-droplets were successfully produced directly, either with the aid of sonication or using a microfluidic device, by using a diacetylene fatty acid or surfactant polymerizable moieties.

The micron size of the poly-PCDA-DFP droplets undergo easier ADV as compared to nano-sized ones, but allowing also efficient reversibility. However, nano-sized PFP filled droplets were efficiently converted into microbubbles upon ultrasound irradiation using the same conditions.

Further deep studies are needed in a future work to characterize the shell properties of these systems as well as their acoustic properties, since how a microbubble behaves in an ultrasound field is largely determined by the mechanical properties of the shell. And the performance of these systems as UCAs will be studied *in vitro* and *in vivo*.

In particular poly-PCDA nanodroplets surface can be implemented through bioconjugation of their carboxylic moieties with antibodies, proteins, peptides as tumoral targets, etc. Moreover, the potential of nanodroplets as a reservoir for hydrophobic drug delivery and their theranostic ability will be evaluated.

Appendix

References

- [1] Meier, W. Polymer Nanocapsules. *Chem. Soc. Rev.* **2000**, *29*, 295-303.
- [2] Neuberg, P.; Périno, A.; Morin-Picardat, E.; Anton, N.; Darwich, Z.; Weltin, D.; Mely, Y.; Klymchenko, A. S.; Remy, J. S.; Wagner, A. Photopolymerized Micelles of Diacetylene Amphiphile: Physical Characterization and Cell Delivery Properties. *Chem. Comm.* **2015**, *00*, 1-3.
- [3] Vinod, T. P.; Chang, J. H.; Kim, J.; Rhee, S. W. Self-Assembly and Photopolymerization of Diacetylene Molecules on Surface of Magnetite Nanoparticles. *Bull. Korean Chem. Soc.* **2008**, *29*, 799-804.
- [4] Park, Y.; Luce, A. C.; Whitaker, R. D.; Amin, B.; Cabodi, M.; Nap, R. J.; Szeleifer, I.; Cleveland, R. O.; Nagy, J. O.; Wong, J. Y. Tunable Diacetylene Polymerized Shell Microbubbles as Ultrasound Contrast Agents. *Langmuir* **2012**, *28*, 3766–3772.
- [5] Qin, G.; Li, Z.; Xia, R.; Li, F.; O'Neill, B. E.; Goodwin, J. T.; Khant, H. A.; Chiu, W.; Li, K. C. Partially polymerized liposomes: stable against leakage yet capable of instantaneous release for remote controlled drug delivery. *Nanotechnology* **2011**, *22*, 155605.
- [6] de Oliveira, C. P.; de Fátima Ferreira Soares, N.; Fontes, E. A. F.; de Oliveira, T. V.; Filho, A. M. M. Behaviour of polydiacetylene vesicles under different conditions of temperature, pH and chemical components of milk. *Food Chem.* **2012**, *135*, 1052–1056.
- [7] NOPWINYUWONG, A.; BOONSUPTHIP, W.; PECHYEN, C.; SUPPAKUL, P. Formation of Polydiacetylene/Silica Nanocomposite as a Colorimetric Indicator: Effect of Time and Temperature. *Adv. Polym. Tech.* **2012**, *00*, 1–8.
- [8] Lee, H. Y.; Tiwari, K. R.; Raghavan, S. R. Biopolymer capsules bearing polydiacetylenic vesicles as colorimetric sensors of pH and temperature. *Soft Matter* **2011**, *7*, 3273-3276.
- [9] Rapoport, N. Phase-Shift, Stimuli-Responsive Perfluorocarbon Nanodroplets for Drug Delivery to Cancer. *Wiley Interdiscip Rev Nanomed Nanobiotechnol.* **2012**, *4*, 492–510.
- [10] Rapoport, N.; Kennedy, A. M.; Shea, J. E.; Scaife, C. L.; Nam, K. H. Controlled and Targeted Tumor Chemo therapy by Ultrasound-Activated Nanoemulsions/microbubbles. *J. Controlled Release.* **2009**, *138*, 268–276.

Appendix

[11] Prietro, C.; Calvo, L. Performance of the Biocompatible Surfactant Tween 80, for the Formation of Microemulsions Suitable for New Pharmaceutical Processing. *J. App. Chem.* **2013**, Doi: 10.1155/2013/930356.

[12] Singhal, S.; Moser, C. C.; Wheatley, M. A. Surfactant-Stabilized Microbubbles as Ultrasound Contrast Agents: Stability Study of Span 60 and Tween 80 Mixtures Using a Langmuir Trough. *Langmuir* **1993**, *9*, 2426-2429.

[13] Lee, J. H.; Danino, D.; Raghavan, S. R. Polymerizable Vesicles Based on a Single-Tailed Fatty Acid Surfactant: A Simple Route to Robust Nanocontainers. *Langmuir* **2009**, *25*, 1566-1571.

[14] Lin, H.; Chen, J.; Chen, C. A novel technology: microfluidic devices for microbubble ultrasound contrast agent generation. *Med. Biol. Eng. Comput.* **2016**, *54*, 1317-1330.

[15] Hettiarachchi, K.; Talu, E.; Longo, M. L.; Dayton, P. A.; Lee, A. P. On-chip generation of microbubbles as a practical technology for manufacturing contrast agents for ultrasonic imaging. *Lab Chip* **2007**, *7*, 463-468.

[16] Segers, T.; de Rond, L.; de Jong, N.; Borden, M.; Versluis, M. Stability of Monodisperse Phospholipid-Coated Microbubbles Formed by Flow-Focusing at High Production Rates. *Langmuir* **2016**, *32*, 3937-3944.

ACKNOWLEDGMENTS

First off, I would like to express my distinguished gratitude to my Professor Gaio Paradossi who has helped and supported me, in every sense of the word, to conduct my PhD research in the best conditions, and for keeping his encouragement and enthusiasm.

My sincere gratitude goes also to the team members for their hospitality, friendship, help and science sharing: Dr. Ester Chiessi and all my colleagues I crossed the chance to meet and work with during my PhD, Barbara, Letizia, Fabio, Nikki, Sabrina, Silvia and Sharad.

I am also grateful to our collaborators Dmitry Grishenkov, Philippe Trochet Pierangela Giustetto, Francesco Basoli and Silvia Orlanducci.

I would like to acknowledge the University of Rome Tor Vergata and the financial supports contributing in the realization of this thesis project from the MUIR, FILAS fellowship regarding “Progettazione di Nuovi Microdispositivi Polimerici per Applicazione Biomediche” and the European Union Seventh Framework Programme FP7/2007-2013 under Grant Agreement No. 602923 “THERAGLIO”.

A special thank goes also to Dr. Mark Telling as being more than a guest of our team, giving advices and bringing humor and “wisdom podcasts”.

Finally, special recognition goes out to my family, for their support, encouragement and patience during my PhD and my entire educational path. Thanks are also extended to all my friends and everyone who contributed directly and indirectly to the accomplishment of this thesis work.

LIST OF PUBLICATIONS

Peer-reviewed scientific articles

Fasolato, C.; Giantulli, S.; Silvestri, I.; Mazzarda, F.; **Toumia, Y.**; Ripanti, F.; Mura, F.; Luongo, F.; Costantini, F.; Bordi, F.; Postortino, P.; Domenici, F. Folate-based Single Cell Screening Using Surface Enhanced Raman Microimaging. *Nanscale* **2016**, *8*, 17304-17313.

Toumia, Y.; Domenici, F.; Orlanducci, S.; Mura, F.; Grishenkiv, D.; Trochet, P.; Lacerenza, S.; Bordi, F.; Paradossi, G. Graphene Meets Microbubbles : A Superior Contrast Agent for Photoacoustic Imaging. *ACS App. Mater. Interfaces* **2016**, *8*, 16465-16475.

Chronopoulou, L.; **Toumia, Y.**; Cerroni, B.; Pandolfi, D.; Paradossi, G.; Palocci, C. Biofabrication of Genipin-Crosslinked Peptide Hydrogels and their Use in the Controlled Delivery of Naproxen. *N. Biotechnol.* **2016**, *In Press (corrected Proof)*, DOI: [10.1016/j.nbt.2016.04.006](https://doi.org/10.1016/j.nbt.2016.04.006).

Chronopoulou, L.; Margheritelli, S.; **Toumia, Y.**; Paradossi, G.; Bordi, F.; Sennato, S.; Palocci, C. Biosynthesis and Characterization of Cross-Linked Fmoc Peptide-Based Hydrogels for Drug Delivery Applications. *Gels* **2015**, *1*, 179-193.

Toumia, Y.; Orlanducci, S.; Basoli, F.; Licoccia, S.; Paradossi, G. Soft Confinement of Graphene in Hydrogel Matrixes. *J. Phys. Chem. B.* **2015**, *119*, 2051-2061.

Congress contributions

Abstract for Poster Contribution in ECIS 2016, Rome, September 4-9, Italy: Fasolato C, Ripanti F, Mazzarda F, **Toumia Y**, Giantulli S, Silvestri I, Luongo F, Mura F, Costantini F, Bordi F, Postorino P, Domenici F. "Surface enhanced Raman microimaging allows for screening single cells with different folate binding capabilities". (Awarded best poster prize)

Abstract for Poster Contribution in Raman Fest 2016, Berlin, May 19-20, Germany: Fasolato C, Ripanti F, Mazzarda F, **Toumia Y**, Giantulli S, Silvestri I, Luongo F, Mura F, Costantini F, Bordi F, Postorino P, Domenici F. "Surface enhanced Raman microimaging allows for screening single cells with different folate binding capabilities". (Awarded best poster prize)

Abstract and oral Poster presentation in The 21st European Symposium on Ultrasound Contrast Imaging, January 21-22, 2016 (Rotterdam, The Netherlands): **Toumia Y**, Grishenkov, D, Cerroni, B, Domenici, F, Orlanducci, S, Trochet, P,

Paradossi, G. "Graphene PVA Microbubbles: A New Hybrid Ultrasound-Photoacoustic Imaging Contrast Agent".

Abstract and Poster Contribution in Graphene Week 2015 (Manchester, UK), June 22-26, 2015: **Toumia Y**, Grishenkov D, Orlanducci S, Larsson M, Zhao Y, and Paradossi G." Graphene Functionalized PVA Microbubbles as Contrast Agent for Photoacoustic Imaging".

Poster Contribution in Scuola Soft Matter (San Servolo, Venice, Italy), June 16-20, 2014: **Toumia, Y.**; Orlanducci, S.; Basoli, F.; and Paradossi, G. "Direct Graphene Aqueous Solution Production For Non Covalent Stabilization in PVA-MA Based Hydrogel and Microgel".

Abstract for poster contribution in EMIM Meeting 2014, June,04-06, Anversa, Belgium: Capece S, Giustetto, P, **Toumia Y**, Orlanducci S, Quercioli A, Cavalli R, Paradossi G. "Microvesicle/Microbubble Assisted Photoacustics as Potential Imaging Enhancer for Preclinical Studies.

Abstract and Poster Contribution in Graphene 2014 Congress (Toulouse, France), May 06-09, 2014: **Toumia, Y.**; Orlanducci, S.; and Paradossi, G. "Study on non covalently-stabilized graphene en PVA-MA hydrogel".